

# Studies for the LHCb SciFi Tracker

Development of Modules from Scintillating Fibres  
and Tests of their Radiation Hardness

Dissertation zur Erlangung  
des akademischen Grades

Dr. rer. nat.

vorgelegt von

**Robert Jan Ekelhof**

geboren am 18.02.1983

in Braunschweig

Fakultät Physik

Technische Universität Dortmund

Dortmund, im März 2016

CERN-THESIS-2016-098  
18/05/2016



Der Fakultät Physik der Technischen Universität Dortmund zur Erlangung des akademischen Grades eines Doktors der Naturwissenschaften vorgelegte Dissertation.

1. Gutachter: Prof. Dr. B. Spaan
2. Gutachter: Priv.-Doz. Dr. R. Klingenberg

Datum des Einreichens der Arbeit: 31.03.2016  
Datum der mündlichen Prüfung: 18.05.2016



## Abstract

The LHCb detector will see a major upgrade in the LHC long shutdown 2, which is planned for 2019/20. Among others, the tracking stations, currently realised as silicon strip and drift tube detectors, will be replaced by the Scintillating Fibre (SciFi) Tracker. The SciFi Tracker is based on scintillating fibres with a diameter of 250  $\mu\text{m}$ , read out by multichannel silicon photomultipliers. The two major challenges related to the fibres are the radiation damage of the light guidance and the production of precise multi-layer fibre mats.

This thesis presents radiation hardness studies performed with protons at the tandem accelerator at Forschungszentrum Garching and in situ in the LHCb cavern. The obtained results are combined with additional data of the LHCb SciFi group and two different wavelength dependent models of the radiation induced attenuation are determined. These are used to simulate the relative light yield, for both models it drops to 83 % on average at the end of the nominal lifetime of the SciFi Tracker.

A machine and techniques to produce multi-layer fibre mats were developed and optimised. Procedures for the production and alignment are described. These are implemented in the serial production of the SciFi modules which will start in the second quarter 2016.

## Kurzfassung

Der LHCb-Detektor wird im LHC Long Shutdown 2, welcher für 2019/20 geplant ist, ein großes Upgrade erhalten. Unter anderem werden die Tracking-Stationen, die derzeit als Kombination aus Siliziumstreifen und Driftröhren realisiert sind, durch den Scintillating Fibre (SciFi) Tracker ersetzt werden. Der SciFi Tracker basiert auf szintillierenden Fasern mit einem Durchmesser von 250  $\mu\text{m}$ , welche von mehrkanaligen Silizium-Photomultipliern ausgelesen werden. Die beiden großen Herausforderungen beim Einsatz der Fasern sind der Strahlenschaden der Lichtleitung und die Herstellung präziser mehrlagiger Fasermatten.

In dieser Arbeit werden Untersuchungen zur Strahlenhrte der Fasern mit Protonen am Tandembeschleuniger am Forschungszentrum Garching und in situ in der LHCb Kaverne vorgestellt. Die erhaltenen Ergebnisse werden mit zusätzlichen Daten der LHCb SciFi Gruppe kombiniert. Zwei unterschiedliche Beschreibungen des wellenlängenabhängigen Schadens werden bestimmt. Diese werden verwendet, um die relative Lichtausbeute zu simulieren, welche für beide Modelle im Mittel auf 83 % am Ende der nominellen Laufzeit des SciFi Trackers sinkt.

Eine Maschine und Techniken zur Herstellung von mehrlagigen Fasermatten wurden entwickelt und optimiert. Es werden Verfahren zur Produktion und Ausrichtung beschrieben. Diese werden in der Serienproduktion der SciFi-Module implementiert, welche im zweiten Quartal 2016 beginnen wird.



# Contents

<b>1</b>	<b>Introduction</b>	<b>1</b>
<b>2</b>	<b>LHC and the experiments</b>	<b>5</b>
2.1	The Standard Model of particle physics . . . . .	5
2.2	Physics at LHC . . . . .	6
2.3	The accelerator complex . . . . .	7
2.4	The detectors . . . . .	9
<b>3</b>	<b>LHCb and its upgrade</b>	<b>13</b>
3.1	The LHCb detector . . . . .	13
3.1.1	Tracking . . . . .	14
3.1.2	Particle identification . . . . .	15
3.1.3	Trigger . . . . .	16
3.2	Data taking and physics results . . . . .	17
3.3	Upgrade strategy . . . . .	19
3.4	Subdetector upgrades . . . . .	20
3.4.1	Tracking . . . . .	20
3.4.2	Particle identification . . . . .	23
<b>4</b>	<b>The Scintillating Fibre Tracker</b>	<b>25</b>
4.1	The LHCb tracking upgrade requirements . . . . .	25
4.2	The path to the SciFi Tracker . . . . .	28
4.3	LHCb SciFi Tracker Components . . . . .	30
4.3.1	Signal flow . . . . .	32
4.3.2	Geometry . . . . .	40
4.3.3	Schedule . . . . .	47
4.3.4	Performance . . . . .	47
<b>5</b>	<b>Module construction for the Scintillating Fibre Tracker</b>	<b>53</b>
5.1	The design of the SciFi modules . . . . .	53
5.2	Winding of fibre mats . . . . .	55
5.2.1	Winding concepts . . . . .	55
5.2.2	Alignment of the fibre mat . . . . .	60
5.2.3	Influence of diameter fluctuations of the fibres . . . . .	61
5.2.4	The prototype winding machine . . . . .	65
5.2.5	The serial production winding machine . . . . .	66

## Contents

5.3	Quality assurance . . . . .	69
5.4	Serial production . . . . .	73
5.5	Summary & outlook . . . . .	73
<b>6</b>	<b>Scintillating fibres research</b>	<b>75</b>
6.1	Basic principle . . . . .	75
6.1.1	Scintillation . . . . .	75
6.1.2	Light guidance . . . . .	78
6.1.3	Radiation Damage . . . . .	80
6.2	Mechanical properties . . . . .	81
6.3	Light guidance . . . . .	86
6.4	Radiation damage . . . . .	97
6.4.1	Proton beam irradiation . . . . .	97
6.4.2	In-situ irradiation . . . . .	99
6.4.3	Other measurements . . . . .	111
6.4.4	Combination of irradiation results . . . . .	114
6.4.5	Simulation of the light loss due to radiation . . . . .	119
6.5	Summary & outlook . . . . .	123
<b>7</b>	<b>Conclusion</b>	<b>127</b>
<b>A</b>	<b>Appendix</b>	<b>vii</b>
A.1	Proton irradiation . . . . .	vii
A.2	In situ irradiation . . . . .	ix
A.3	Combination of irradiation measurements . . . . .	xvii
A.4	Light yield maps . . . . .	xviii
	<b>Bibliography</b>	<b>xxiii</b>
	<b>List of figures</b>	<b>xxxix</b>
	<b>Acknowledgment</b>	<b>xxxv</b>

# 1 Introduction

The LHCb experiment is one of the four large experiments at the Large Hadron Collider (LHC) [1]. It is dedicated to precision measurements of properties of particles including  $b$  or  $c$  quarks. These allow for a stringent test of the Standard Model of particle physics (SM) [2–4]. The SM is a very successful theory, all the measurements so far are within the predictions and in multiple occasions a particle or parameter has been predicted which was confirmed by an experiment afterwards. However some observations are not described by the SM: Gravitation, neutrino masses, dark energy and dark matter. Deviations of the precise theory predictions and precise experimental observations would constitute an indirect hint for so-called New Physics, physics beyond the SM.

The LHCb detector performed very well in Run 1 of the LHC (2011-2013) [5], collecting the world's largest sample of charm and beauty decays. This enabled the collaboration to make measurements of key parameters. So far, no deviations from the SM have been observed and more precise tests are needed to further test the SM.

To lower the statistical uncertainties significantly, a major upgrade of the LHCb detector is planned for the LHC Long Shutdown 2 [6] in 2019-20. The instantaneous luminosity will be increased by a factor five to  $2 \times 10^{33} \text{ cm}^{-2} \text{ s}^{-1}$ . To gain from the higher luminosity, the hardware trigger will be removed, and the selection will be performed by a much more flexible full software trigger only. This is enabled by the trigger-less read-out of the detector with 40 MHz, implying an upgrade of the on-detector electronics of most sub-detectors. To maintain the excellent performance of the detector at the increased luminosity, the sub detectors are upgraded, especially all tracking detectors need to be replaced.

The LHCb detector is implemented as a forward spectrometer. The tracking system consists of three sub detectors. One tracker surrounds the interaction point, the other two are situated in front of and behind the dipole magnet, respectively. The Tracking Stations behind the magnet are currently realized as a combination of a silicon strip Inner Tracker and a drift tube Outer Tracker. The higher track multiplicity at the upgrade conditions requires a replacement of this sub-detector. Two alternatives were studied: Firstly a redesign with an enlarged Inner Tracker to lower the occupancy in the Outer Tracker; the chosen second technology is a Scintillating Fibre Tracker (SciFi), covering the whole acceptance with a single technology.

The SciFi Tracker covers about  $360 \text{ m}^2$  with modules of thin scintillating fibres [7]. The fibres have a diameter of  $250 \mu\text{m}$  and are arranged parallel, in 2.5 m long 6-layer fibre mats. The scintillation photons are guided along the fibre and detected by multichannel Silicon

## 1 Introduction

Photomultipliers (SiPM) placed at the upper and lower edges of the detector, outside the LHCb acceptance. These are cooled down to  $-40^{\circ}\text{C}$  to limit the radiation induced thermal noise. The SiPMs are read out by a custom designed ASIC, integrating the signal over 25 ns.

The work performed in this thesis contributed to several aspects of the SciFi Tracker R&D. It focussed on the design and construction of the tracker and on the radiation hardness of the scintillating fibres. Many of the studies presented in this document already entered other official documents and reviews of the SciFi group. The first tests of fibre mat production were described in the *Letter of Intent for the LHCb Upgrade (LoI)* [6]. The work on the design of the modules and especially the fibre mats and their production had huge impact to the respective technology choices, which were among others described in the *Tracker Upgrade Technical Design Report (TDR)* [7]. The almost final design was documented in the *Engineering Design Review: Fibres, Mats and Modules* [8].

In parallel to the R&D for the fibre mat production, studies on the properties of scintillating fibres were pursued. Contributions were made to the determination of the basic properties of scintillating fibres, the development of quality assurance measurements for the serial production and the tests of the radiation hardness. The first irradiation results were described in the LoI. In addition to the own studies, the work is expressed in the contributions to the *Viability Assessment of a Scintillating Fibre Tracker for the LHCb Upgrade* [9] and the *SciFi Tracker Technology Validation Review* [10]. The former concentrated on the radiation hardness of the scintillating fibres and the silicon photomultipliers, concluding that it is worth to continue the R&D program. The latter validated the SciFi Tracker as the technology chosen for the Tracking Stations, also comparing it to the enlarged IT alternative. Preliminary results of scintillating fibres irradiated in the LHCb cavern have been described in the TDR.

This thesis is structured as follows: To fit the LHCb experiment in the context, the LHC and the detectors are explained in chapter 2. It is prefaced with a brief description of the Standard Model and the physics studied at the LHC experiments. The LHCb experiment is described in more detail in chapter 3, especially motivating and describing the Upgrade. The LHCb Upgrade conditions result in requirements for the SciFi Tracker, listed at the beginning of chapter 4. These determine the overall design of the tracker and the realization of the components described in this chapter.

Since the work focussed on the design and the production of the modules (especially the fibre mats) and the properties of scintillating fibres, these are described in more detail. Chapter 5 is dedicated to the production of the fibre mats. Therefore, the evolution of the module design and the production procedure of the mats is presented. The described challenges in the winding of the mats lead to the final design of the developed serial winding machine. The chapter closes with the description of quality assurance tests and the planning for the serial production.

Chapter 6 starts with the explanation of the principle of function of scintillating fibres, followed by tests of mechanical properties, and measurements and simulation studies on

the light guidance. The latter ones are used as input for the irradiation tests described in the following sections. The results are complemented by additional studies of the LHCb SciFi group, to define a global model for the radiation damage. This is used to simulate the expected degradation of the light output of the fibres in the course of the runtime of the upgraded detector, which is a crucial parameter to optimise the performance of the SciFi Tracker.

The developments and studies presented in this thesis could not have been performed without the contribution of other people of the SciFi group. Respective documents, such as technical notes and master and bachelor theses, are referenced at the respective positions in the text.





## 2 LHC and the experiments

The Large Hadron Collider (LHC) is the world's largest and most powerful particle accelerator operated by CERN (European Organization for Nuclear Research) at the Franco-Swiss border near Geneva. Detectors record the particles of proton-proton collisions (in addition lead-lead and proton-lead collisions are studied). This chapter gives an overview over the accelerator, the detectors and the physics studied with these.

### 2.1 The Standard Model of particle physics

The Standard Model of particle physics (SM) is a theory which describes the elementary particles and their interactions [2–4]. These are briefly explained in the following.

Quarks and leptons are fermions with spin  $1/2$ . Both exist in three generations with a pair of quarks/leptons each. The quarks are up, down, charm, strange, top and beauty (or bottom) with a respective attribute called flavour. Quarks carry colour charge, they interact via the strong interaction (in addition to all the other interactions). The leptons are the electron, muon and tauon with their corresponding neutrinos. The leptons are colour neutral, the neutrinos do not carry an electromagnetic charge, they only interact via the weak interaction. The particles of the first generation are the lightest ones and are therefore stable (neutrons are only stable in bound in a nucleus), all the known matter consists of up- and down quarks and electrons.

The forces between the fermions are mediated by the gauge bosons. The properties of these particles determine the properties of the interactions. The mathematical description of these interactions can be visualized by so called Feynman diagrams. Photons mediate the electromagnetic force. Weak interactions are mediated by  $W^\pm$  and  $Z$  bosons. Due to the high mass of these bosons, the range of the weak force is short. The weak interaction allows the change of the flavour and to break CP-symmetry (so called CP violation). The electromagnetic and the weak interaction are combined in the electro-weak theory. Gluons mediate the interaction between colour charged particles, the strong force. The fact that gluons itself carry colour, leads to the fact that they can interact with themselves.

Predicted in 1964 and discovered in 2012, the Higgs Boson was the last particle predicted by the Standard Model to be seen in an experiment [15, 16]. Like explained in the next section one of the main goals of the ATLAS and CMS experiments was the discovery of the Higgs. The so-called Higgs mechanism gives mass to the particles of the SM.

On the one hand, the SM is a very successful theory. All measurements are well within the prediction. In multiple occasions a particle or parameter has been predicted which was confirmed by an experiment afterwards. On the other hand, there are many observations which are not described by the SM: Gravitation, neutrino masses, dark energy and dark matter. To solve the remaining open questions, the LHC experiments search for deviations from the SM, so-called New Physics.

## 2.2 Physics at LHC

The Large Hadron Collider (LHC) (together with the experiments) is designed to answer open questions of the Standard Model [11]. The LHC is installed in the existing tunnel of the Large Electron Positron Collider (LEP) but uses protons which enables to reach higher energies. These are needed to investigate particles with higher masses. In contrast to lepton colliders, hadron colliders produce events with a large spectrum of energies. This is caused by the fact that the interactions are dominated by the interactions of the sea quarks and gluons [12]. This eases the search for particles of unknown masses but makes it more challenging to analyse decays with specific energies due to higher background.

One goal of the experiments is to measure the parameters of the Standard Model to a precise level, so that deviations from the theory predictions would be visible. The two largest experiments (ATLAS [13] and CMS [14]) are multi purpose detectors, designed to cover a wide physics spectrum. The main goal was to discover the SM Higgs. A Higgs-like particle was found in 2012 ( [15], [16]). Having more data available in 2013, it was possible to determine properties of this particle which are in agreement with the SM Higgs [17].

The ALICE experiment [18] is specialised in heavy-ion collisions to study the strong interaction sector of the SM, although it also takes data and performs analyses at proton-ion and proton-proton collisions. The high energy density and temperature in the lead-lead collisions are used to address the physics of strongly interacting matter and the quark-gluon plasma.

The LHCb experiment [1] is specialised in heavy flavour physics. It studies CP violation and rare decays of beauty and charm hadrons to search for indirect evidence of new physics, while performing precision tests of the SM. The results from other experiments so far are consistent with the SM. However, the level of CP violation cannot explain the mismatch of matter and antimatter in our universe, a new source of CP violation is needed for this. Many models of new physics show contributions which would be visible in the LHCb observables (an example is given in Sec. 3.2).

## 2.3 The accelerator complex

The LHC is a proton-proton ring accelerator. It is designed to reach a centre of mass energy of up to 14 TeV with a design luminosity of  $10^{34} \text{ cm}^{-2} \text{ s}^{-1}$ . A sketch of the accelerator complex at CERN is shown in Fig.2.1. [19]

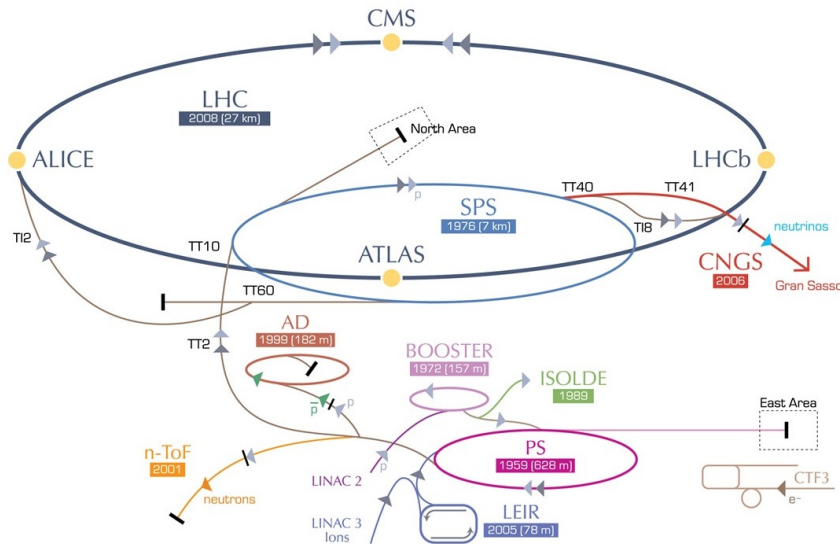


**Figure 2.1:** The CERN accelerator complex. [19]

The LHC is installed in the existing LEP tunnel. The possibility to reuse this had influence on the decision to built LHC at CERN. In addition the caverns for ALICE and LHCb could also be inherited, while those for ATLAS and CMS were newly built. The fact that LHC (in contrast to LEP) is a particle-particle collider leads to the need for two rings.

Because of the lack of space in the tunnel, the twin-bore magnet design was chosen (see Fig. 2.2). This means that two sets of coils and beam channels are installed in the same mechanical structure and cryostat. The high energies of LHC can only be reached with superconducting magnets. The LHC magnets are operated at a temperature of below 2 K with the help of superfluid helium, which is unique among superconducting synchrotrons. Like this a peak dipole field of 8.33 T (design value) can be reached.

Due to the given layout of the LEP tunnel, the LHC is arranged in eight arcs and eight straight sections. ATLAS and CMS are situated at point 1 and 5. Point 2 and 8 are housing ALICE and LHCb and the injections points. The protons are pre-accelerated before entering the LHC. The injection chain for LHC is LINAC2, Proton Synchrotron (PS) Booster, PS and Super Proton Synchrotron (SPS), see Fig. 2.1. Filling LHC requires 12 SPS cycles with 3-4 PS cycles each. Completely filled, the LHC accelerates 2808 bunches of  $1.1 \times 10^{11}$  protons each, with a spacing of 25 ns.

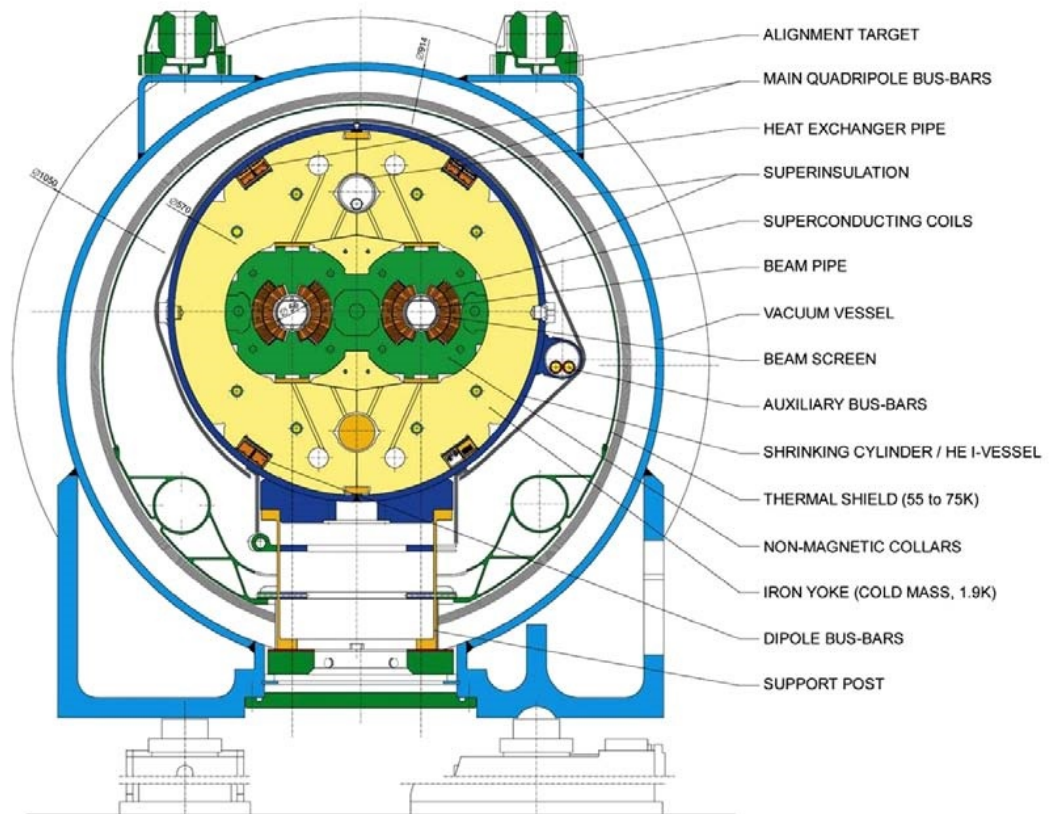


**Figure 2.2:** The cross-section of an LHC dipole magnet. [19]

The beams are brought to collision inside the four experiments. They do not collide head on but under an angle of 150 to 200  $\mu\text{rad}$ , so one does not get unwanted collisions near the interaction points. The luminosity does not stay constant during a run, because the number of protons in a bunch decreases (see Fig. 2.3). The main reason for this are the beam collisions. The luminosity at LHCb is kept small (at  $L = 4 \times 10^{32} \text{ cm}^{-2} \text{ s}^{-1}$ , to obtain events which are clean and better reconstructible), so it can be levelled to stay constant during a fill.

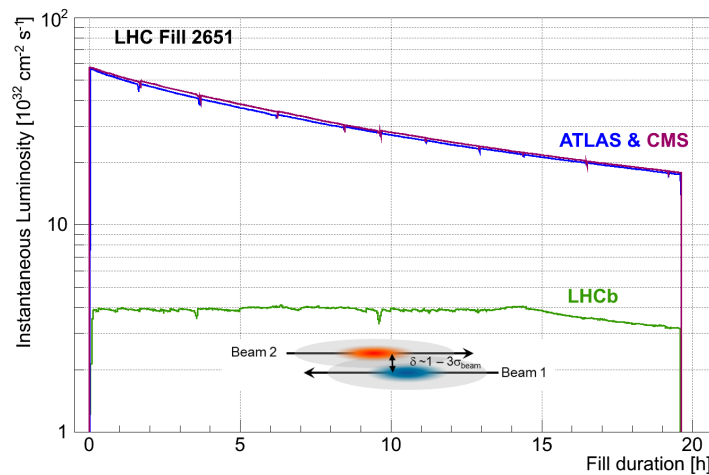


**Figure 2.3:** Luminosity trend during a fill. The levelling keeps the luminosity constant at LHCb for a long time. [5]

The LHC can also be operated with heavy ions. These collisions are essential for the ALICE experiment, but are also used in ATLAS, CMS and LHCb. Operated in this modus, the LHC can reach energies of up to 2.76 TeV per nucleon and a centre of mass energy of 1.15 PeV with a luminosity of  $10^{27} \text{ cm}^{-2} \text{ s}^{-1}$ .

## 2.4 The detectors

The detectors record the decay products of the proton collisions. They were designed to cope with the high bunch collision rate of 40 MHz and the high multiplicity. Up to  $1 \times 10^9$  inelastic events per second can be observed at the LHC design luminosity [14]. Up to 1000 charged particles pass each detector in one bunch crossing. The frequency of events and number of particles requires high-granularity detectors with fast read-out electronics. As an example the CMS Inner Tracker combines 75 million channels to cover  $200 \text{ m}^2$  of which 90 % cover the innermost square-meter. But not all the events include decays interesting for physics and only a small amount of them can be stored. That is why good triggers are essential to select interesting events. In LHCb events are stored

## 2 LHC and the experiments

with 5 kHz (in 2012 data taking [20]) which corresponds to a reduction by a factor  $8 \times 10^3$  (more information on the LHCb Trigger and its upgrade can be found in chapter 3).

The general purpose detectors are designed to have a good geometric coverage with good calorimetry to calculate missing energy in events. They are arranged in a cylindrical way around the beam pipe (e.g. see CMS Fig. 2.4). The sub detectors can mainly be divided in two groups, track finding and particle identification. The tracking detectors are closest to the interaction point, they determine the decay vertices and, with the help of magnets, the momentum of the particles. They are followed by the electromagnetic and hadronic calorimeters, which determine the energy of the respectively interacting particles. Muons are not absorbed by these and are detected in the designated muon chambers, the outermost sub-detectors.

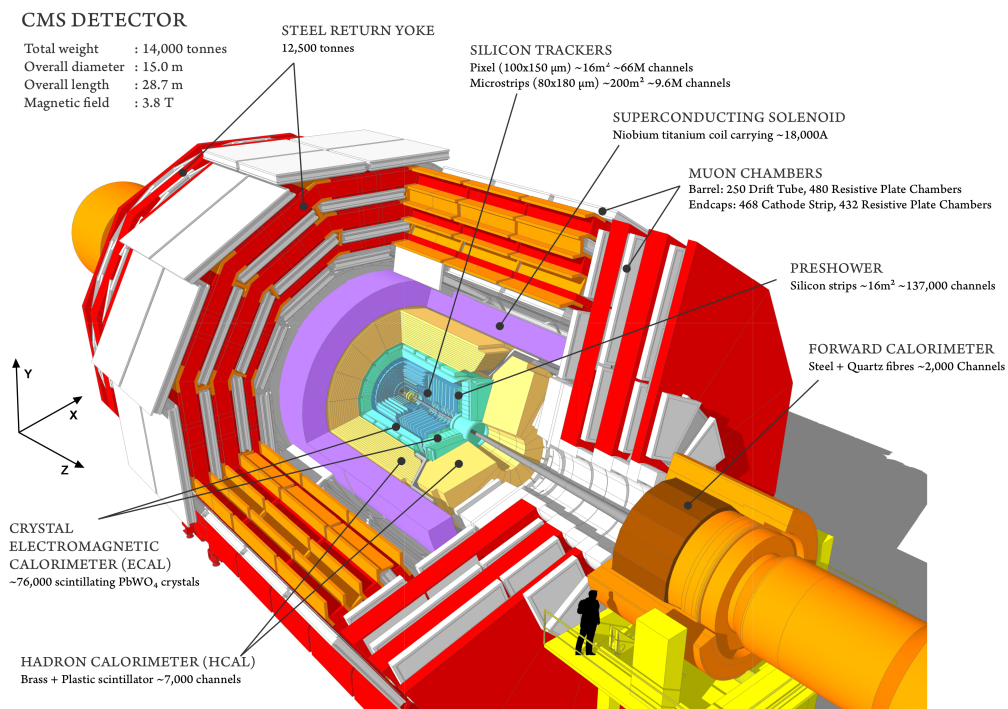


**Figure 2.4:** Cut-away view of the CMS detector. [21]

The LHCb design is optimised to study the decay of B hadrons [1]. At the LHC, gluon fusion is the dominant process for b quark production. It is likely that the gluons have a high momentum asymmetry which leads to a large momentum of the  $b\bar{b}$  pair. It is very likely that both b quarks are produced in small angles with respect to the beam-pipe (see Fig. 2.5). For measurements dedicated to CP-violation, it is essential to detect both b quarks. Measuring the decay products of one, the production state of the other can be determined (flavour tagging). Because of that, the LHCb detector is built as a single arm forward spectrometer (see Fig. 2.6). The central tracking detector (Vertex Locator) is

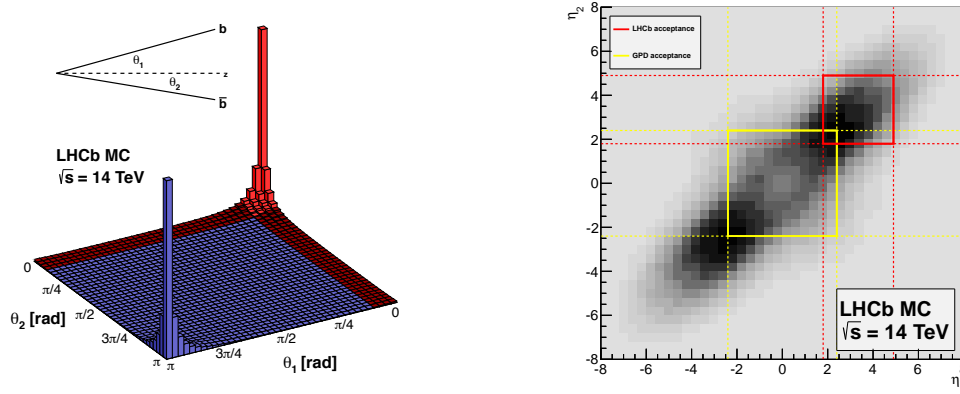


**Figure 2.5:**  $b\bar{b}$  production angles, the LHCb acceptance is marked in red. The number of produced  $b\bar{b}$  pairs is shown as the function of the angle  $\theta$  (left) and the pseudorapidity  $\eta$  (right). [22]

constructed as part of the beam pipe surrounding the interaction point, while all the other sub-detectors are mounted downstream behind one another.

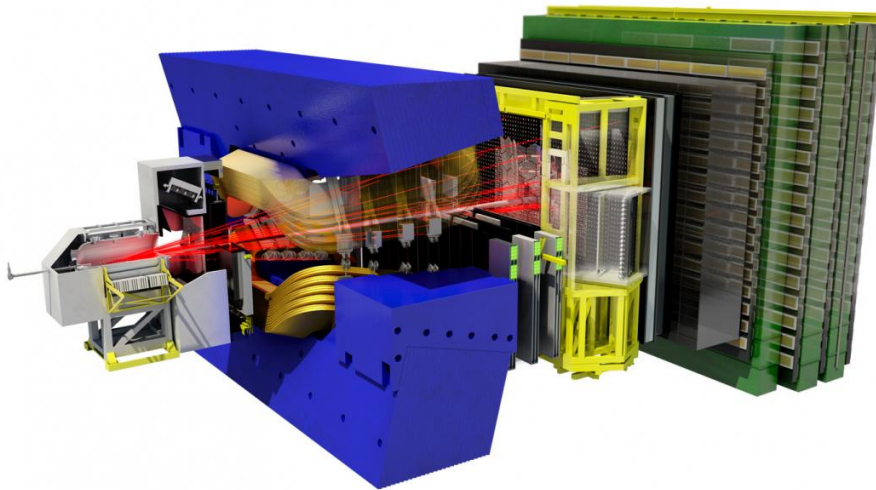


**Figure 2.6:** Cut-away view of the LHCb detector. [23]

To achieve a good charged particle momentum resolution, the detectors need to provide a high magnetic field. The special structure of LHCb enables a large tracking system which can work with a conventional magnet with a lower magnetic field of 1 T (the superconducting magnet of CMS reaches a field of up to 4 T). More details on the LHCb detector are covered in the next chapter.





# 3 LHCb and its upgrade

This chapter describes the current LHCb detector and the key physics results of LHCb in Run 1. To lower the statistical uncertainties, of the examined parameters an upgrade of the detector is planned. The upgrade strategy and the modified or newly developed sub-detectors are introduced later in this chapter.

## 3.1 The LHCb detector

The LHCb detector is built as single-arm spectrometer. It covers the forward region with an angular range of 15 mrad to 300 (250) mrad in the bending (non-bending) plane of the dipole magnet [1], which corresponds to about 2.4 % of the total solid angle. In this acceptance LHCb can observe 25 % of  $b\bar{b}$  quark pairs produced [22]. The Vertex Locator (VELO) surrounds the interaction point, all the other sub-detectors are designed planar and arranged one behind the other (see Fig. 3.1). The right handed coordinate system is arranged with the z-axis pointing in the direction of the proton beam, downstream from the interaction point, and the y-axis pointing upwards. The sub-detectors are described in the following paragraphs, the information is based on [1] and [5].

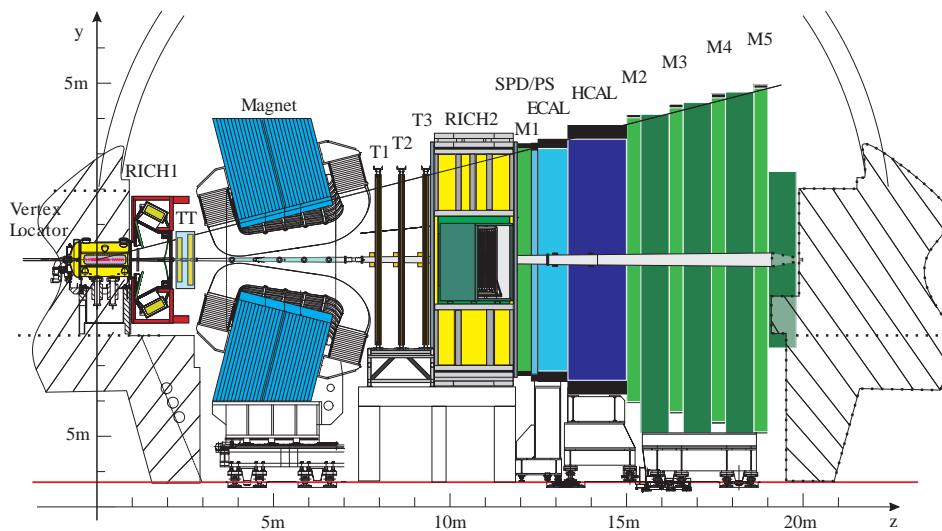


Figure 3.1: Schematic cross section of the LHCb detector. [6]

### 3.1.1 Tracking

The tracking detectors are the Vertex Locator (VELO) at the interaction point, the Tracker Turicensis (TT) in front of the magnet and the Tracking Stations behind the magnet, which are split in Inner- and Outer Tracker (IT / OT). The dipole magnet provides an integrated field of about 4 Tm to determine the momentum of charged particles, the bending plane is oriented perpendicular to the y-axis

#### VELO

The Vertex Locator (VELO) is a silicon strip detector surrounding the interaction point (IP). It is introduced in the beam-pipe inside a vacuum tank which enables a small inner radius of 8.2 mm. This leads to a short distance to the IP and a very good coverage of the high rapidity region.

The VELO consists of modules arranged along the beam, each with strips in radial and azimuthal direction with a strip pitch of 38 to 102  $\mu\text{m}$ . The aperture is smaller than needed for the beam during injections, that is why the VELO is built in two halves which can be moved in and out. In addition, the beam conditions at LHCb are monitored by the so-called BCM (Beam Conditions Monitor). In case of abnormal conditions, the VELO modules are moved out and a beam dump can be triggered.

#### TT

The Tracker Turicensis<sup>1</sup> (TT) covers an area of  $150 \times 130 \text{ cm}^2$  with 183  $\mu\text{m}$  silicon strips. It is built of four layers in an x-u-v-x geometry with vertical strips in the first and last layer (parallel to the y-axis) and stereo-angles of  $-5^\circ$  and  $5^\circ$  in the middle layers. The whole surface sums up to  $8 \text{ m}^2$ .

#### IT & OT

The three Tracking Stations T1-T3 behind the magnet are split in the Inner and Outer Tracker (IT/OT). Each station is built from four modules arranged in the x-u-v-x geometry, with the IT station mounted in front of the OT station, see Fig. 3.2.

The silicon strip IT covers the inner area with high track density. It is cross-shaped with outer dimensions of  $120 \times 40 \text{ cm}^2$ . The strip pitch is 198  $\mu\text{m}$  with strip lengths of 218 and 414 mm. The whole surface sums up to  $4 \text{ m}^2$ .

The OT is a drift tube detector and covers the area outside the IT. The outer dimensions are about  $6 \times 5 \text{ m}^2$ . The whole surface sums up to  $360 \text{ m}^2$ . The OT is built from 200 gas-tight

---

<sup>1</sup>Turicensis is the latin name of Zurich, the main contributor to the construction of this tracker. It was chosen as the original name Trigger Tracker was misleading after a strategy change during the planning phase of LHCb. Thus, the abbreviation TT could be kept.

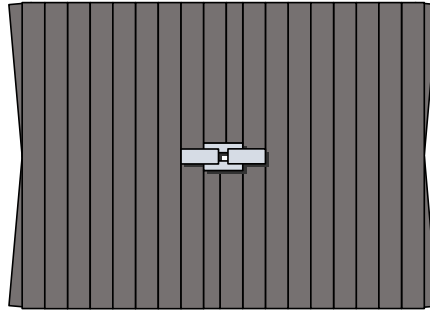


**Figure 3.2:** Schematic of one station of the Inner and Outer Tracker. The direction of view is parallel to the beam pipe, looking from the interaction point. The Outer Tracker is shown in dark grey, the Inner Tracker in light grey.

straw-tube modules. The drift-tubes have an inner diameter of 4.9 mm and are flushed with a gas mixture of Argon (70 %), CO<sub>2</sub> (28.5 %) and O<sub>2</sub> (1.5 %). The drift time stays below 50 ns and the achieved spatial resolution is about 200  $\mu\text{m}$ .

### 3.1.2 Particle identification

#### RICH

The Ring Imaging Cherenkov detectors (RICH) are used for charged hadron identification, especially to distinguish kaons from pions. Two RICH detectors are installed, RICH1 is situated in front of the TT while RICH2 is situated behind the T-stations. Momentum information, provided by the tracking system, combined with particle candidates are used to predict potential cherenkov cones. These are compared to the measured photon distributions (see Fig. 3.3) to obtain respective probabilities.

#### Calorimeters

The calorimeter system is composed of different sub-detectors. The main components are the electromagnetic calorimeter (ECAL) and the hadronic calorimeter (HCAL). To improve the distinction between photons and electrons a scintillating pad detector (SPD) and a preshower detector (PS) are placed in front of the ECAL. In addition to energy determination, the calorimeters provide particle distinction and deliver information for the first level trigger (L0) in selecting candidates with high transverse energy.

All calorimeters follow the same basic principle: The light produced in scintillators is guided to photomultipliers with wavelength shifting fibres. The ECAL is built as shashlik type, the lead absorbers sum up to 25 radiation lengths. The HCAL uses iron absorbers corresponding to 5.6 interaction lengths.

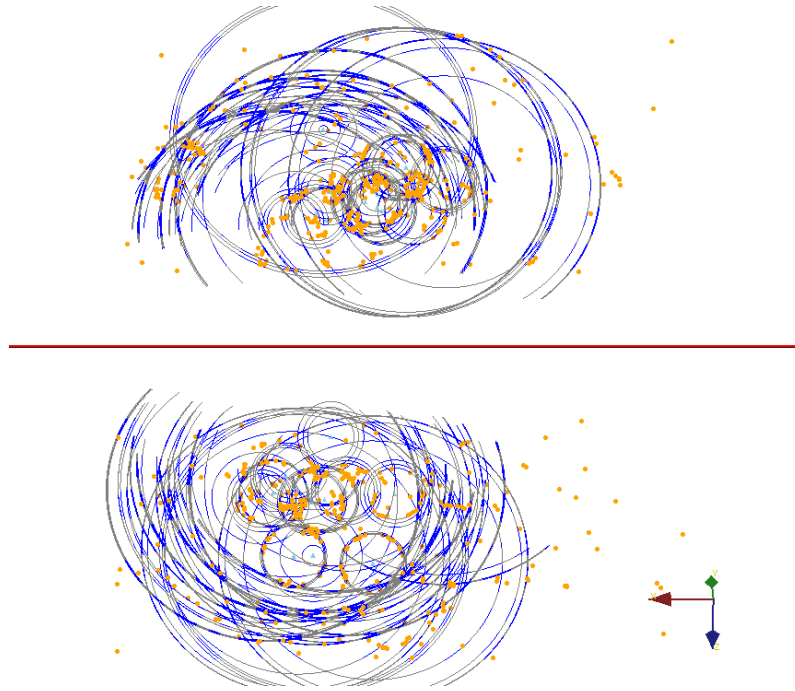


**Figure 3.3:** Rings are fitted to the measured photons (orange) in the upper and lower half of the RICH 1. [24]

## MUON

The five muon stations (M1-M5) are mainly built as multi-wire proportional chambers. M1 is placed before the calorimeters, M2-M5 are the outermost sub-detectors of LHCb. The iron absorbers add up to 20 interaction lengths (including the HCAL). The muon stations deliver important information to the L0 and HLT (High Level Trigger) because muons occur in many final states of important decays.

### 3.1.3 Trigger

The LHCb Trigger is split in two parts (see Fig. 3.4). The first level trigger (L0) is implemented in hardware. It gets information from the calorimeters and the muon stations and works synchronous to the 40 MHz bunch crossing signal of the LHC. The data rate is reduced from 40 MHz bunch crossing rate to 1 MHz. This data is send out to a processor farm where the HLT reduces the rate to 5 kHz. The High Level Trigger (HLT) makes use of the full event data and runs a simplified version of the offline event reconstruction. The remaining data is stored and is available for analysis.

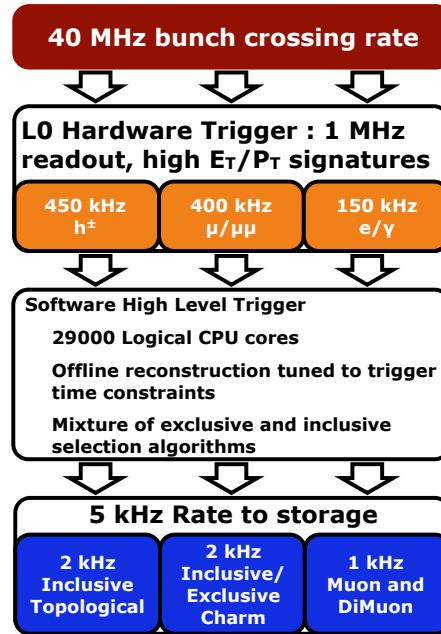


**Figure 3.4:** LHCb Trigger Scheme 2012. The first level is implemented in hardware to reduce the input rate for the software trigger to 1 kHz. [25]

## 3.2 Data taking and physics results

Two important parameters for the operation of LHCb are the instantaneous luminosity and the pile-up, the average number of visible interactions per beam-beam crossing. The evolution of these parameters for Run 1 (2010-2012) is shown in Fig. 3.5. The LHCb detector is designed for a low pile-up to enable clean events for good triggering and reconstruction. Due to the low number of bunches in the LHC in 2010, the pile-up was increased to raise the instantaneous luminosity to the design value. It was shown that the detector can be operated under these challenging conditions. In 2011, the number of bunches in the LHC was increased in steps to the maximum possible with 50 ns spacing. Thus, the pile-up at LHCb could be reduced while the instantaneous luminosity could be raised to twice the design value ( $4 \times 10^{32} \text{ cm}^{-2} \text{ s}^{-1}$ ). The integrated luminosity is shown in Fig. 3.6, LHCb recorded  $3 \text{ fb}^{-1}$  in Run 1. The LHC beam energy was 3.5 TeV in 2010 and 2011 and was increased to 4 TeV in 2012.

In Run 1 LHCb has collected the world's largest sample of charm and beauty decays. This enabled LHCb to make many key results already [5]. In July 2015 LHCb, announced the observation of particles composed of five quarks. They have a minimal quark content  $c\bar{c}uud$  and hence are called pentaquark-charmonium [26]. LHCb contributed to the measurement of many observables in flavour physics. Already after Run 1, world best precision is reached in several of these, e.g. in determining the CKM angle  $\gamma$  [27]. In others it is

### 3 LHCb and its upgrade

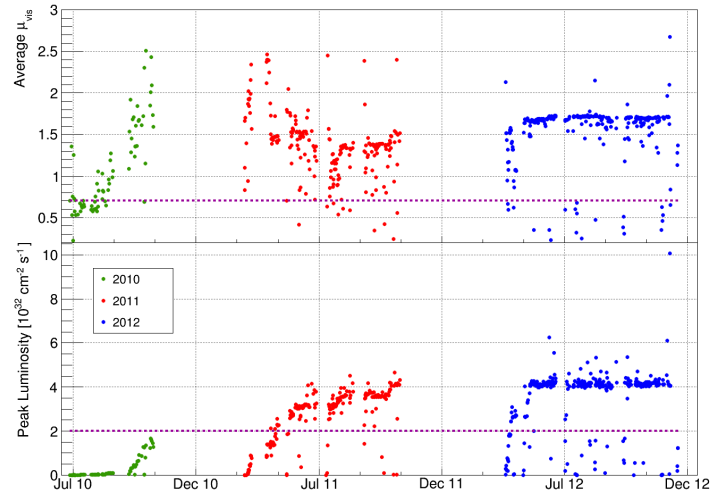


**Figure 3.5:** The pile-up (average  $\mu_{vis}$ ) (top) and instantaneous luminosity (bottom) at LHCb. The dotted lines show the design values. [5]

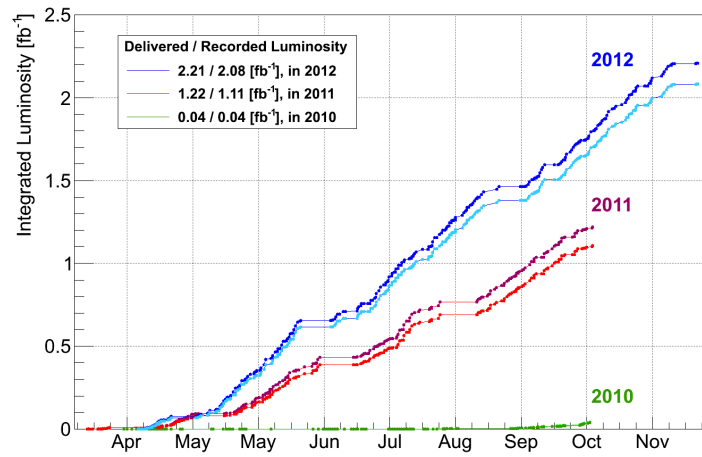


**Figure 3.6:** Development of the integrated luminosity in LHCb in Run 1 (2010-2012). Delivered and recorded luminosities are shown in dark and light colours. [5]

expected to reach world best sensitivity after Run 2, like in consolidating the measurement of the CKM angle  $\beta$  [28].

The measurements in the flavour sector have great impact to the studies of New Physics effects. One key measurement of LHCb is the measurement of the branching fraction of the rare decay  $B_s^0 \rightarrow \mu^+ \mu^-$ . The LHCb experiment published the first evidence in 2012 [29], and the joint LHCb and CMS analysis resulted in the first observation of the decay [30]. It is mediated by a flavour changing neutral current which is highly suppressed in the Standard Model. Various New Physics models allow for higher cross sections.

The current measurements are within the predictions of the SM, but higher sensitivity is needed to confirm or disprove New Physics modifications to the branching fraction. The data set will be enlarged in Run 2, after that a larger step is needed to increase the sensitivity substantially. With the help of an increased luminosity and an upgraded detector in Run 3, LHCb will be able to lower the statistical uncertainties. With this it is additionally possible to reduce the systematic uncertainties as well. Thus, a new level of parameter limits will be reached. Furthermore, even more rare decays like  $B^0 \rightarrow \mu^+ \mu^-$  can be measured.

The LHCb experiment is not the only one performing measurements in the flavour sector. Beside ATLAS and CMS, BELLE II [31, 32] will join, starting to take physics data in 2018. The different experimental approaches guarantee complementarity [33]. Hence it is essential continuing to make strong contributions to the flavour physics field.

### 3.3 Upgrade strategy

An upgrade of LHCb is essential to take the next step in sensitivity after Run 1 and Run 2 [6]. To enlarge the data sample significantly, the instantaneous luminosity is increased from  $4 \times 10^{32} \text{ cm}^{-2} \text{ s}^{-1}$  to  $2 \times 10^{33} \text{ cm}^{-2} \text{ s}^{-1}$ . As mentioned in chapter 2.3, the luminosity at LHCb is kept small to obtain events which are clean and better reconstructible. Hence, for the upgrade, the increase in luminosity can be achieved with the current LHC performance.

But an increase in instantaneous luminosity will not linearly increase the recorded data sample, the limiting factor is the Level-0 hardware trigger [34]. It is currently needed to reduce the readout rate of the detector to 1 MHz and is limited to decisions based on basic signatures like large transverse energy. The reduced efficiency of the trigger chain at higher luminosities, especially for purely hadronic decays (see Fig. 3.7), is dominated by the hardware trigger. The more restrictive thresholds required at higher luminosities also cut away substantial parts of the signal. Therefore, the upgraded LHCb detector will have a trigger-less readout system and the complete data at the full collision rate will be processed by a full software trigger (see Fig. 3.8). To increase the trigger efficiency and reduce the systematic uncertainties, a simplified version of the offline reconstruction is executed in the trigger (see Fig. 3.9), the achieved gain in hadronic event yields is about a factor ten in comparison to Run 1 [34]. The full event reconstruction on trigger level can

only be achieved with detectors optimised for this purpose. The operation of the SciFi Tracker permits to perform the complete tracking sequence on the computer farm.

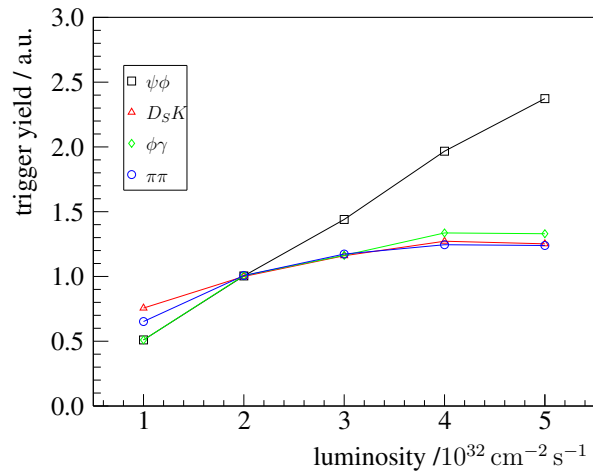


**Figure 3.7:** Trigger yield as a function of the instantaneous luminosity. The yield rises slower than linear due to the lower trigger efficiency with increasing instant luminosity. Data from [6].

## 3.4 Subdetector upgrades

The current sub detectors were designed for low multiplicity. In order to maintain the performance at higher instantaneous luminosity, the detectors will be upgraded. An overview of the upgraded detector is shown in Fig. 3.10. The specific changes are described in the following sections.

### 3.4.1 Tracking

All tracking detectors will be replaced in the course of the LHCb Upgrade. The readout electronics have to send out the data with 40 MHz and the larger amount of tracks calls for a higher granularity.

The VELO will be replaced by a pixel detector [35]. The new VELO is based on modules arranged in a similar pattern (see Fig. 3.11), now with 41 million  $55 \times 55 \mu\text{m}^2$  pixels and features an integrated microchannel evaporative  $\text{CO}_2$  cooling. The new sensors will be closer to the interaction point with a closest distance of 5.1 mm to the beam axis.

The geometry of the tracking detector in front of the magnet stays the same. The new Upstream Tracker (UT) has segments of silicon strips with ASICs connected directly to



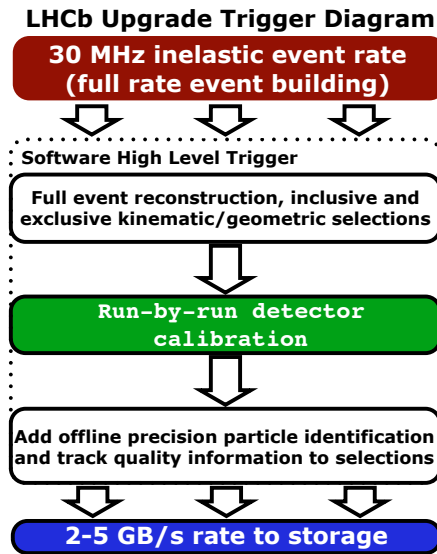


**Figure 3.8:** LHCb Trigger Scheme Upgrade. The trigger is completely implemented in software, analysing the data at the full inelastic event rate. [25]

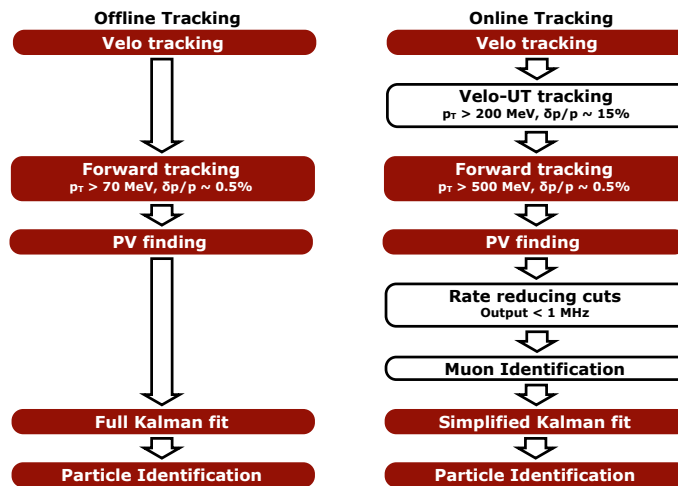


**Figure 3.9:** LHCb Trigger Scheme online-offline comparison, a simplified version of the offline analysis is executed in the trigger. [25]

### 3 LHCb and its upgrade

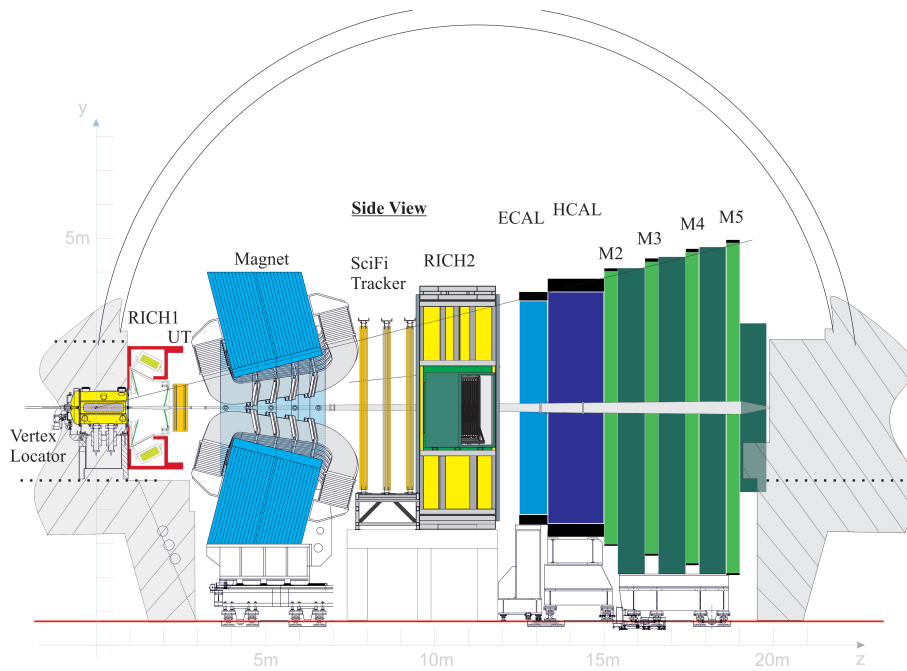


**Figure 3.10:** The upgraded LHCb detector. [7]

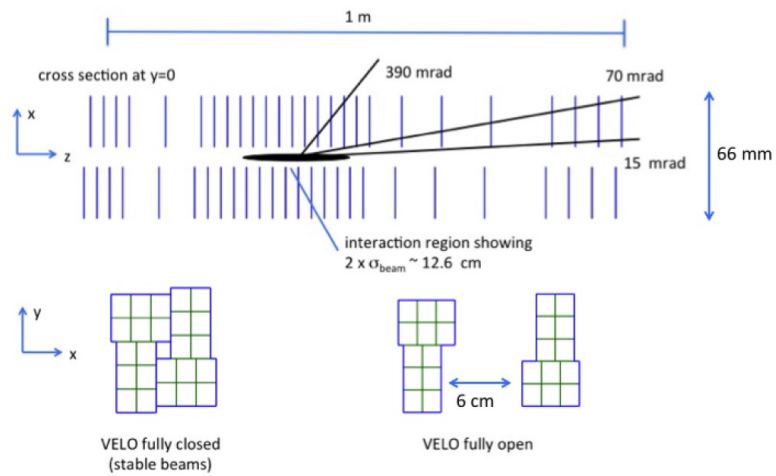


**Figure 3.11:** Schematic layout of the upgraded VELO. [35]

the sensor, see Fig. 3.12. The granularity of the sensors (length and pitch of the strips) is higher close to the beam-pipe.

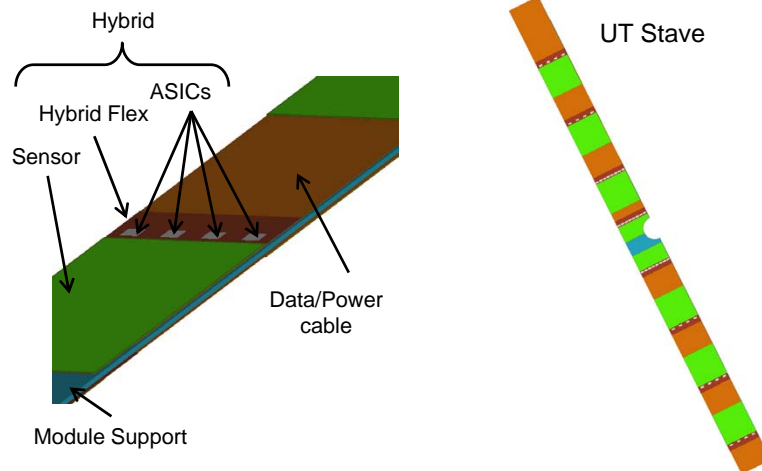


**Figure 3.12:** UT stave structure. [7]

The tracking stations downstream the magnet will be replaced by a new homogeneous technology. The Scintillating Fibre Tracker (SciFi Tracker) is based on scintillating fibres with a diameter of  $250\ \mu\text{m}$  read out by Silicon Photomultipliers (SiPM) with a pitch of  $250\ \mu\text{m}$ . The SciFi Tracker is explained in detail in chapter 4.

### 3.4.2 Particle identification

The general design of the current PID system is well suitable for the harsh environment of the LHCb Upgrade. The main changes are due to the new readout at 40 MHz and the omission of the Level-0 Trigger [36]. The photodetectors of the RICHes need to be replaced. The currently used Hybrid Photodetectors have their 1 MHz electronics encapsulated in the tubes, they will be replaced by Multianode Photomultipliers with external electronics. In addition, the geometry of the mirrors of RICH 1 will be optimised for the new occupancies (see Fig. 3.13).

The electronics of the calorimeters will also be redesigned to enable the 40 MHz readout. The gain of the photomultipliers will be reduced to reduce its ageing effects. The detector itself will stand the increased radiation levels, a replacement of the inner part of the ECAL is considered in LHC Long Shutdown 3, in the course of the running period of the upgraded detector. The Preshower and Scintillating Pad Detector will be removed as they were mainly used to provide information for L0.

The front-end electronics of the Muon Stations already fulfil the 40 MHz readout since the information was used in the L0 trigger. However, the back-end electronics need to be redesigned to provide all detailed information to the full software trigger. Due to increased

### 3 LHCb and its upgrade

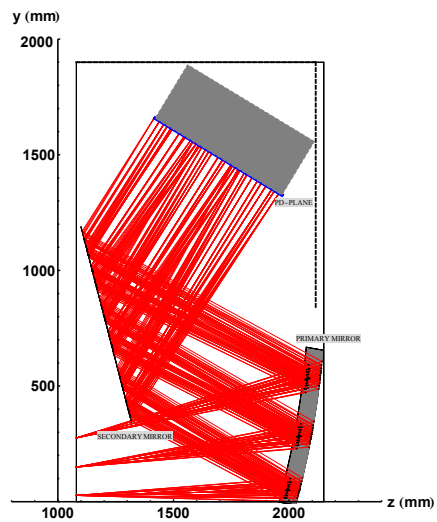


**Figure 3.13:** Simulated Cherenkov photons in the upper half of the upgraded RICH 1.  
[36], modified

occupancies, M1 will be removed and an additional shielding around the beam-pipe in front of M2 reduces the particle rate in the other stations.

# 4 The Scintillating Fibre Tracker

This chapter describes the motivation to use a scintillating fibre tracker in LHCb while explaining the tracking upgrade requirements and the path which lead to the decision in favour of the SciFi Tracker. The group at TU Dortmund had a significant impact in the development of the SciFi Tracker in the early phase and still has for scintillating fibre R&D and module production. The work performed in the course of this thesis contributed to these aspects. The components of the SciFi Tracker are described in the third section of this chapter.

## 4.1 The LHCb tracking upgrade requirements

The purpose of the tracking detectors is to provide a high precision momentum measurement. In addition they measure the trajectories of charged particles for the RICH detectors. The information in this section is taken from [6] and [7].

As mentioned before the tracking system of LHCb consists of three trackers: The Vertex Locator (VELO), the Tracker Turicensis (TT) in front of the magnet and the tracking stations T1-T3 behind the magnet, currently implemented as Inner Tracker (IT) and Outer Tracker (OT). Figure 4.1 shows the arrangement of the trackers and the magnetic field strength profile. Also shown are the different types of tracks, discriminated by the trackers in which they are reconstructed. The most important tracks are so called long tracks, they have excellent resolution close to the primary vertex and precise momentum information due to the position information in front of and behind the magnet. T tracks are used to construct downstream tracks, the latter are important for the reconstruction of daughters of long lived particles which decay outside the VELO. Low momentum particles can be reconstructed with upstream tracks. VELO tracks serve as input for the upstream tracks and to reconstruct the primary vertex.

All trackers are designed to provide a high efficiency and high resolution in x-direction (in the bending plane of the magnet). Increasing the number of tracking layers helps to improve the tracking efficiency and to lower the ghost rate<sup>1</sup>, but it increases the material budget which leads to multiple scattering which worsens the momentum resolution.

In the current T-stations, the hit resolution is 200  $\mu\text{m}$  for the OT and 50  $\mu\text{m}$  for the IT, which leads to a resolution of 80  $\mu\text{m}$  / 25  $\mu\text{m}$  per station. The resulting momentum resolution for low momentum tracks in the OT and high momentum tracks in the IT is  $\delta(p)/p =$

---

<sup>1</sup>Ghost tracks are incorrect reconstructed tracks due to wrongly combined real hits or noise hits.

## 4 The Scintillating Fibre Tracker

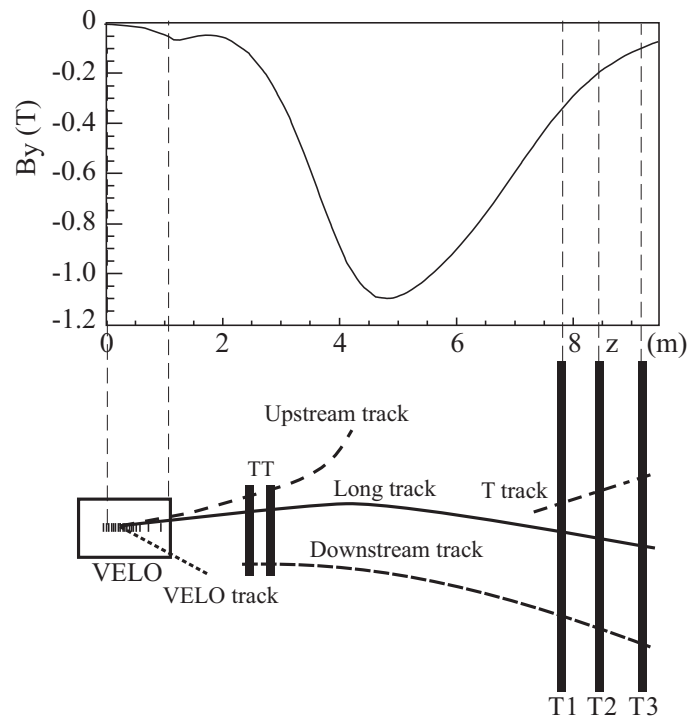


**Figure 4.1:** A schematic view of the LHCb tracking system showing the different track types. The top plot shows the trend of the magnetic field of the LHCb dipole magnet. [5]

## 4.1 The LHCb tracking upgrade requirements

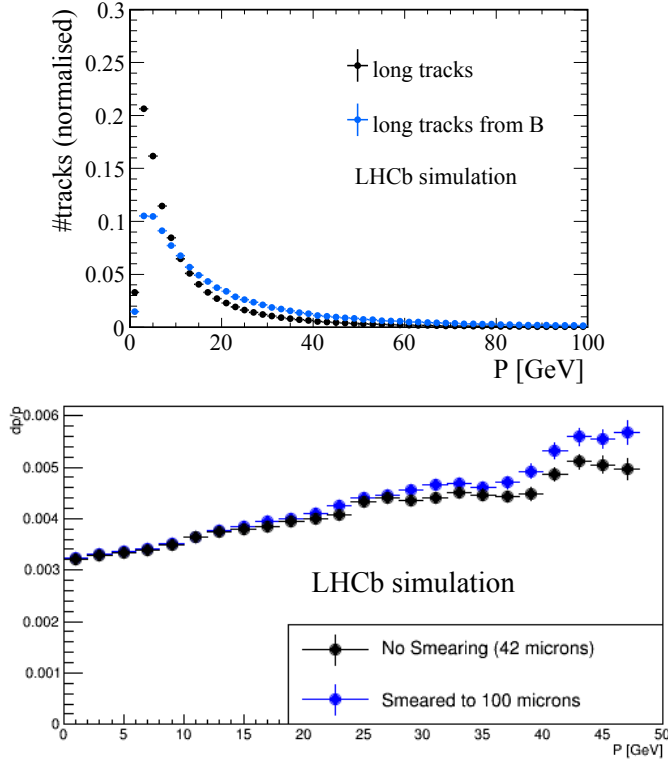


**Figure 4.2:** top: Momentum distribution for long tracks<sup>2</sup>. bottom: Momentum resolution of long tracks for different single hit resolutions of the SciFi Tracker. [7], modified

0.3% – 0.5% in both cases. Especially the low momentum resolution is limited by multiple scattering and not by the hit resolution. Figure 4.2 shows simulation results for the momentum distribution for the Upgrade LHCb and the momentum resolution of the SciFi Tracker as the function of the momentum for two different hit resolutions. It can be seen that the large majority of events has a momentum below 20 GeV, these do not gain in momentum resolution when improving the hit resolution from 100  $\mu\text{m}$  to 42  $\mu\text{m}$ .

Nevertheless, a good hit resolution eases the track reconstruction while allowing for smaller search windows in the tracking which reduces the chance of miss-matched hits. Figure 4.3 shows reconstructed tracks in one event of Run 1, visualizing the track density. The tracking stations are designed as strip detectors, the stereo angle of  $5^\circ$  was chosen as a combination of good experience with the HERA-B detector and dedicated simulation studies. The resulting resolution in  $y$ -direction is 12 times the resolution in the bending plane.

The segmentation of the detectors influences the hit resolution and the occupancy and has to be optimized with respect to the costs. For the current LHCb tracker it was decided to split the T-stations in two regions. The silicon strip IT covers the inner region, while the drift-time detector OT covers the way larger outer region. The IT size was chosen such

<sup>2</sup>To be more precise: For all long reconstructible particles in  $B_s \rightarrow \phi\phi$

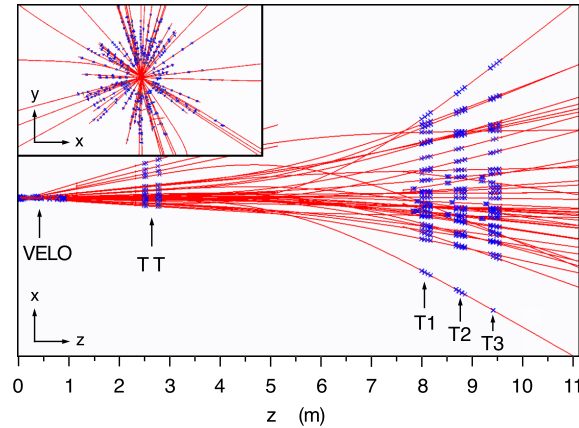


**Figure 4.3:** LHCb reconstructed tracks in an event of Run 1. [1]

that the occupancy in the OT stays below 10 %<sup>3</sup>. Too large occupancies would not allow for a good track reconstruction.

The higher track multiplicity in the upgrade environment requires a redesign of the Tracking Stations. The conservative approach is to enlarge the size of the Inner Tracker to reduce the occupancy in the Outer Tracker modules. The alternative is to use a completely different design based on scintillating fibres.

The requirements for the T-Stations as listed in the LHCb Tracker Upgrade TDR [7] are:

- as large as possible hit efficiency ( $\approx 99\%$ ), with the noise cluster rate staying well below ( $< 10\%$ ) the signal rate at any location of the tracker
- a single hit resolution of better than or equal to  $100\ \mu\text{m}$
- a low material budget, with a radiation length  $\leq 1\%$  per module
- the read-out electronics should read the full event data every bunch crossing (40 MHz)
- this performance should be provided up to an integrated luminosity of  $50\ \text{fb}^{-1}$

To compare different tracking technologies, table 4.1 lists properties and costs for some trackers at the LHC. An alternative to the SciFi Tracker which fulfils the requirements (size, granularity, costs) can only be realized with a mixture of technologies.

## 4.2 The path to the SciFi Tracker

The planning of the LHCb Upgrade began before the first data taking at the LHC. The *Expression of Interest for an LHCb Upgrade* [41] published in 2008 describes the switch

<sup>3</sup>During operation with higher track multiplicities in Run 1, LHCb managed to perform the track reconstruction with OT occupancies up to 25 %.



**Table 4.1:** Overview of different trackers at the LHC. Beside the technology important design criteria like the area to be covered and the expected dose are listed. The Silicon-Pixel detectors are the most expensive ones per area but provide the highest resolution. References to the numbers are given in the footnotes.

Experiment	Tracker	Technology	Area m <sup>2</sup>	Channels × 10 <sup>6</sup>	Resolution μm	Max-Dose/-Fluence	Prize MCHF	Prize/area MCHF/m <sup>2</sup>
LHCb	VELO-Pix	Si-Pixel	0.12 <sup>a</sup>	41 <sup>a</sup>	12/5 <sup>a,b</sup>	8 × 10 <sup>15</sup> neq <sup>c,a</sup>	5.8 <sup>a</sup>	47
	UT	Si-Strip	7.8 <sup>d</sup>	3.5 <sup>d</sup>	61 <sup>d</sup>	3 × 10 <sup>14</sup> neq <sup>c,d</sup>	6.5 <sup>d</sup>	0.83
	OT	Drift-Tube	340 <sup>e</sup>	0.054 <sup>e</sup>	200 <sup>e</sup>	10 kGy <sup>f</sup>	6.2 <sup>e</sup>	0.018
CMS	SciFi	Fibre-SiPM	360 <sup>d</sup>	0.5 <sup>d</sup>	100 <sup>d</sup>	35 kGy <sup>d</sup>	15 <sup>d</sup>	0.042
	Silicon	Si-Pixel	1.1 <sup>g</sup>	66 <sup>g</sup>	< 20 <sup>g</sup>	3 × 10 <sup>15</sup> neq / 840 kGy <sup>g</sup>	11 <sup>h</sup>	10
		Si-Strip	200 <sup>g</sup>	9.3 <sup>g</sup>	< 40 <sup>g</sup>	3 × 10 <sup>15</sup> neq / 70 kGy <sup>g</sup>	66 <sup>h</sup>	0.33
	Upgrade Pixel	Si-Pixel	4.6 <sup>i</sup>	1000 <sup>i</sup>	-/7 <sup>j</sup>	> 10 <sup>16</sup> neq <sup>c,i</sup>	17 <sup>i</sup>	3.7

<sup>a</sup> [35]

<sup>b</sup> Hit resolution and primary vertex resolution (for 100 reconstructed tracks in the vertex)

<sup>c</sup> here: short for 1 MeV n<sub>eq</sub>/cm<sup>2</sup>, number of particles inducing the same damage as the respective number of neutrons with an energy of 1 MeV.

<sup>d</sup> [7]

<sup>e</sup> [37]

<sup>f</sup> Dose expected at the position of the electronics of the IT [38].

<sup>g</sup> [14]

<sup>h</sup> [39]

<sup>i</sup> [40]

<sup>j</sup> Primary vertex resolution (for 100 reconstructed tracks in the vertex)

## 4 The Scintillating Fibre Tracker

to the trigger-less read-out and the need to modify the Tracking Stations. In the same year first ideas for a fibre tracker for LHCb were mentioned [42].

The first possible implementation discussed was an Inner Tracker made of thin fibres. The scintillating fibres would have been coupled to clear fibres to achieve a read-out outside the acceptance [43]. An additional possible field of application was the construction of scintillating fibre Inner Tracking modules as a backup for the silicon strip modules already for Run 2 [44].

Beside that, the idea of a new tracker based on longer scintillating fibres evolved [45]. The *Letter of Intent for the LHCb Upgrade* [6] describes scintillating fibre options for the IT (diameter of 250  $\mu\text{m}$  with clear fibres extension, see Fig. 4.4) and for the OT (diameter of 1 mm). The baseline option for the Tracking Stations was an enlarged and lighter IT combined with an OT with modules of reduced length.

The coupling of the scintillating fibres to clear fibres which need to be guided in front of the OT leads to additional material in the central region above and below the IT. Occupancy studies showed that it would be feasible to extend the Inner Tracker to the full height of two times 2.5 m with scintillating fibres, the so-called Central Tracker (CT) [46]. A CT from scintillating fibres combined with a straw-tube OT was one of the two options beside an increased silicon strip IT with a straw-tube OT described in the *Framework TDR for the LHCb Upgrade* [47] (see Fig. 4.4).

One of the major challenges for a scintillating fibre tracker at the LHC is the harsh radiation environment. The *Viability Assessment of a Scintillating Fibre Tracker for the LHCb Upgrade* [9] concentrated on the radiation damage studies of the scintillating fibres and Silicon Photomultipliers. The positive findings allowed the SciFi group to continue their studies. Beside the studies for the SciFi CT, a larger lighter silicon strip IT was developed in parallel. In the end of 2013 at the *LHCb Upgrade SciFi Tracker: Technology Validation Review* [48], both options were compared and it was decided to concentrate the R&D on the SciFi Tracker. It was also agreed to track the idea of a full SciFi Tracker without a straw tube OT.

Based on that decision, all the components were further developed towards the full SciFi Tracker described in the *Technical Design Report* (TDR) [7] in February 2014. Although the design of the SciFi Tracker has been optimised in many different aspects till then, it has not seen major changes.

### 4.3 LHCb SciFi Tracker Components

The Scintillating Fibre Tracker for LHCb is described in more detail in the following subsections. Due to the fact that it is a project under development this document can not describe the final version.

The SciFi Tracker consists of three stations with four detector layers each (XUVX-geometry), see Fig. 4.5. The active material in one detector layer is made of six layers of

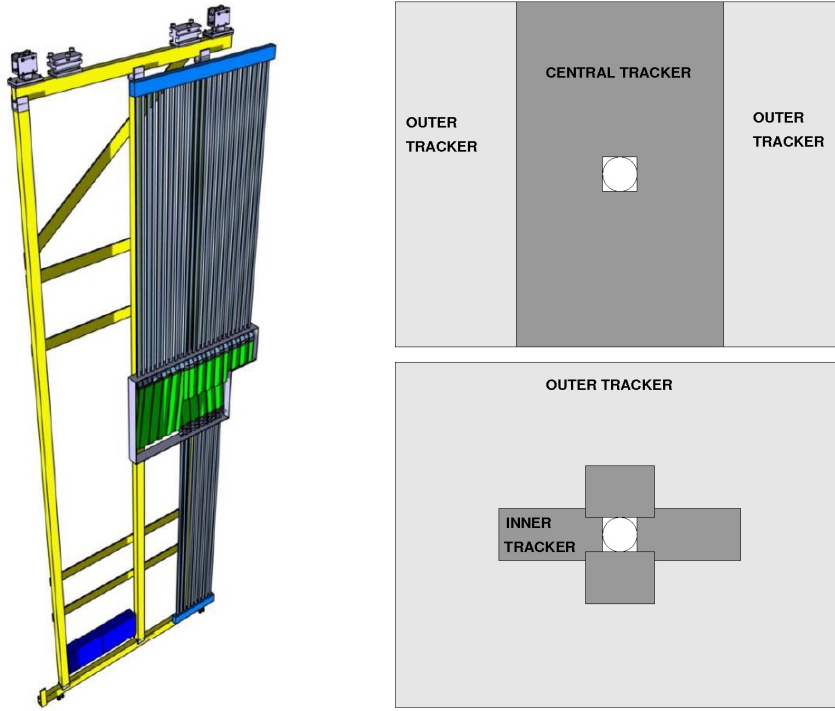


**Figure 4.4:** Left: SciFi Inner Tracker with clear fibres guiding the light to the photo detectors outside the acceptance (left upper half is shown only) as presented in the Letter of Intent for the LHCb Upgrade [6]. The scintillating fibres are shown in green and the clear fibres in grey. Right: Tracking Station options as presented in the Framework TDR: SciFi Central Tracker or silicon strip Inner Tracker, both combined with a straw-tube Outer Tracker [47].

## 4 The Scintillating Fibre Tracker

scintillating fibres with a nominal diameter of  $250\ \mu\text{m}$  to achieve a fine spatial resolution in combination with a high light yield. The photons are detected by multichannel silicon photomultipliers (SiPMs) with rectangular channels of  $250\ \mu\text{m}$  width. The read-out of the SiPMs is based on a custom-designed ASIC chip which integrates the signal over 25 ns. The fibres are supported by sandwich panels. The SiPMs are housed in a closed volume and cooled to  $-40\ ^\circ\text{C}$ .

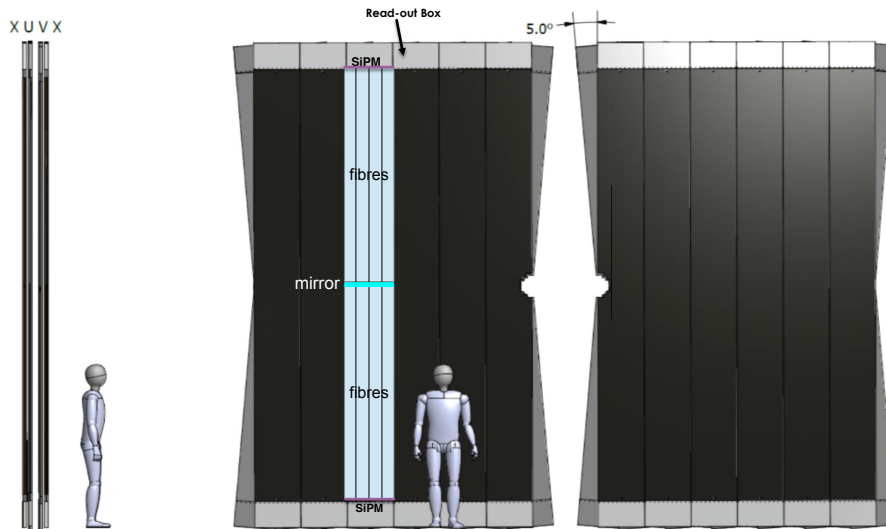


**Figure 4.5:** One station of the SciFi Tracker. One module hosts  $2 \times 4$  fibre mats, these are mirrored on one side, read out at the outside of the detector. [49]

The components are described in two groups. Starting with the signal flow the fibres, SiPMs and electronics are explained. This is followed by the mechanical structure with fibre mats, panels, modules and infrastructure. Its production schedule is discussed following that. The chapter closes with performance measurements and simulations.

### 4.3.1 Signal flow

This subsection describes the signal flow of the Tracker. When a particle passes through a fibre mat it deposits energy in more than one fibre. The scintillation photons travel along the fibres and are detected by multichannel SiPMs. To reduce the noise, thresholds are applied in the electronics and clusters are formed, see Fig. 4.6. The hit position is calculated as weighted average in a cluster which improves the spacial hit resolution.

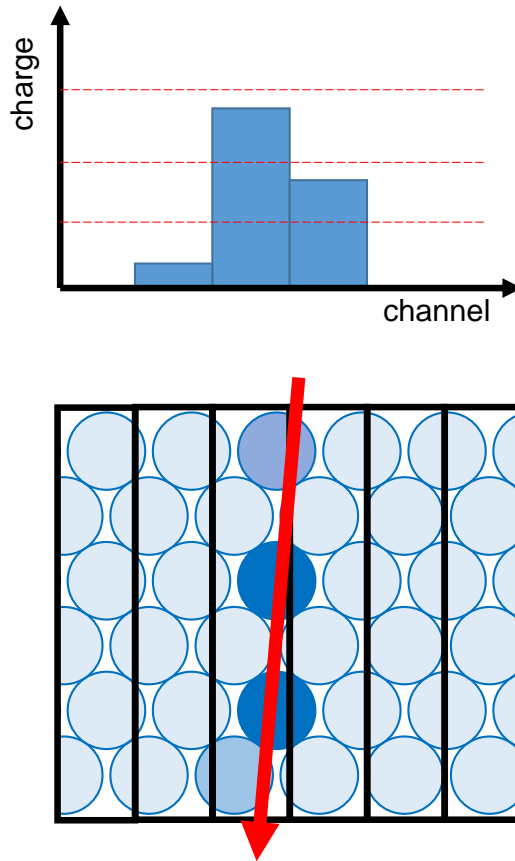


**Figure 4.6:** The SciFi clustering principle. The sketch shows a part of a fibre mat cross section with fibres in blue and SiPM channels in black. A particle crosses the mat which results in a signal in typically more than one SiPM channel. The signal is discriminated by three different thresholds. A cluster is formed in case one channel tops the seed threshold (the medium one) and the sum of all channels which exceed the neighbouring threshold (the lowest one) is higher than the sum threshold. The hit position is calculated as weighted average of all the channels in a cluster.

## Fibres

The fibres considered as baseline option which are also used in the big majority of the tests are Kuraray SCSF-78MJ [50]. These are multicladded plastic fibres. The core is based on polystyrene with additives. The claddings have descending refractive indices to enable light transport via total refraction. The inner cladding is used as linkage to the outer one, which would not be compatible with the core. The fibres are introduced briefly here and explained in more detail in chapter 6.

The amount of light produced scales with the deposited energy. The photons produced travel along the fibre in both directions. To increase the light yield at the SiPMs, the fibres are mirrored at the inner end of the detector. This extends the maximum signal travel time in the fibre. The effective travel speed along the fibre is  $6 \text{ ns m}^{-1}$ , which gives 30 ns for 5 m.

The transparency of the fibres is harmed by the radiation environment. The dose peaks at about 30 kGy close to the beampipe and drops steeper than exponential to the outer regions (see Fig. 4.7). The current estimate for the light loss is 40 % for the fibre damaged the most.

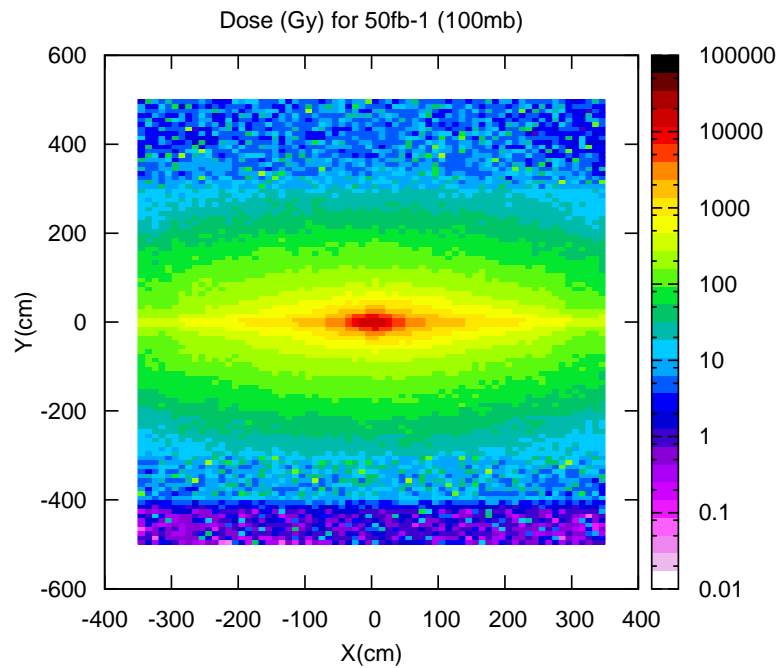


**Figure 4.7:** Simulated dose distribution in Gy at the position of T1 for  $50 \text{ fb}^{-1}$ . [7]

The nominal diameter of the fibres is  $250 \mu\text{m}$ , but however short parts of the fibre can exceed this to above  $400 \mu\text{m}$ , so called bumps. These bumps are an issue in the production of the fibre mats.

## SiPMs

Silicon Photomultipliers are used for the SciFi Tracker because of their ability to detect single photons with their high photon detection efficiency and their beneficial small size with high granularity. In addition they are usable at non cryogenic temperatures and in the presence of magnetic fields.

SiPMs are semiconductor photodetectors. They are based on Avalanche Photodiodes (APD) operated in Geiger-mode. Entering photons (with an energy above the bandgap) introduce an electron hole pair which causes an not stopping avalanche due to the reverse voltage applied (above the breakdown voltage). The avalanche is stopped with the help of a quench resistor which is serially connected to the diode<sup>4</sup>. The signal (current) is independent of the number of entering photons, it is only dependent of the applied voltage. Like this it is possible to reach a gain of  $10^5$  to  $10^7$  [51]. To be able to determine the amount of light, many small diodes (called pixels) are arranged in a matrix<sup>5</sup>. The number of fired pixels represents the number of photons, like this it is possible to reach single photon sensitivity.

The number of fired pixels depends on several parameters. For small amounts of light it is linear to the number of photons, but it begins to saturate when the number of photons is no longer small compared to the number of pixels, see Fig. 4.8. The quantum efficiency accounts for the fact that not all photons cause an avalanche. The geometric efficiency stands for the fraction of the surface which is active. Both effects are combined in the photon detection efficiency (PDE). The PDE of a multichannel SiPM by Hamamatsu is shown in Figure 4.9.

A signal can also be created without entering photons. Thermal noise by random avalanches creates the same signal as a single entering photon. The thermal noise rises strongly with irradiation, entering particles create vacancies which raise the probability for thermal noise. This noise can be reduced by lowering the temperature. The rate is halved every 8 to 10 °C [54]. An additional source for noise is afterpulsing. After a pixel has fired, there is a certain probability that it fires again after some time. For the devices used in the LHCb SciFi Tracker, it contributes only with a minor fraction to the total noise [7]. The average noise rate per channel is expressed as Dark Count Rate (DCR).

The effect of the noise is reduced by applying thresholds (number of pixels fired) in the clustering and the relevant number for the detector is the Noise Cluster Rate (NCR, the rate of cluster formed from primary noise). It depends on the DCR, the typical height of the dark counts and the thresholds. The height of a typical noise signal is mainly driven by the pixel to pixel cross talk<sup>6</sup>. The avalanche in one pixel can lead to the emittance of an additional photon. This can hit a neighbouring pixel and create a signal there. Like this the

<sup>4</sup>The induced current causes a voltage drop across the resistor and the voltage at the diode drops below the breakdown voltage.

<sup>5</sup>It is not feasible to use one large diode to count the photons, because of the dead time caused by the capacity of the diode in combination with the resistor.

<sup>6</sup>Not to be mixed up with channel to channel cross talk which plays a minor role in the LHCb SciFi Tracker.

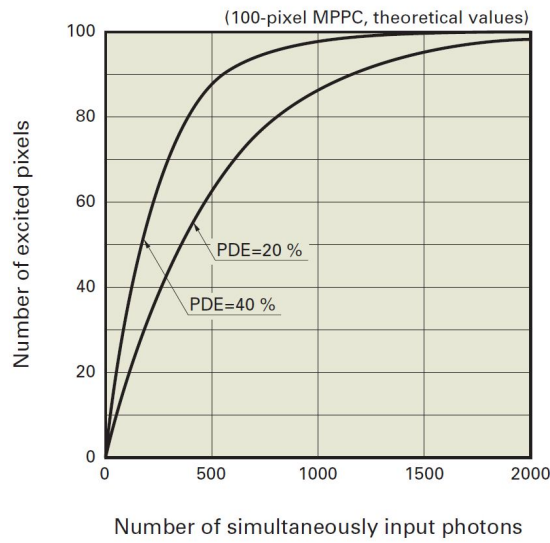


**Figure 4.8:** Number of fired pixels as function of the number of entering photons for two different photon detection efficiencies of a Hamamatsu SiPM. [52]

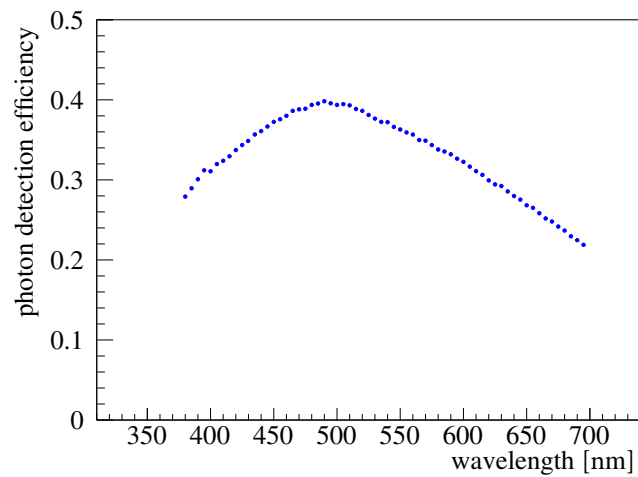


**Figure 4.9:** Photon detection efficiency of an SiPM as the function of the wavelength of the entering photon (a model by Hamamatsu at 3.5 V over voltage, data from [53]).



signal of one primary thermal noise can exceed the thresholds. The influence of the cross talk on the NCR is shown in Fig. 4.10. The PDE and the cross talk are dependent on the over-voltage<sup>7</sup>, so this is a parameter which needs to be tuned for the best signal to noise ratio.

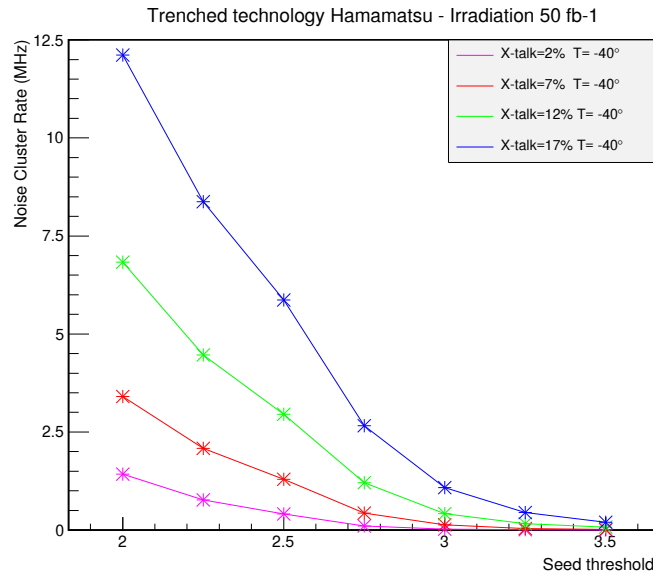


**Figure 4.10:** Simulated noise cluster rate as a function of the cross-talk and the seed threshold in photon equivalents. [7]

The LHCb SciFi Tracker uses 128 channel SiPMs. In fact they are built from two dies with 64 channels on one mechanical unit (see Fig. 4.11). Smaller devices would increase the amount of dead regions, larger ones would be more expensive (more difficult to produce and more prone to failure) and less flexible in operation (e.g. the bias voltage is fixed per dye). The current tests are performed with SiPMs from two manufacturers, Hamamatsu<sup>8</sup> and KETEK<sup>9</sup>, which were both especially designed for this project. The SiPMs of both manufacturers were developed further over the last years, for example to improve the PDE. A major improvement was the introduction of so-called trenches between the pixels. This drastically decreased the cross talk and therewith the noise cluster rate. Nevertheless, the SiPMs need to be cooled down to  $-40^{\circ}\text{C}$  to achieve a NCR which is sufficiently low. The cooling technology is described in Sec. 4.3.2.

<sup>7</sup>The over-voltage is the difference of the applied bias voltage and the breakdown voltage.

<sup>8</sup>Hamamatsu Photonics K.K., 325-6, Sunayama-cho, Naka-ku, Hamamatsu City, Shizuoka Pref., 430-8587, Japan.

<sup>9</sup>KETEK GmbH, Hofer Str. 3, 81737 München, Germany.

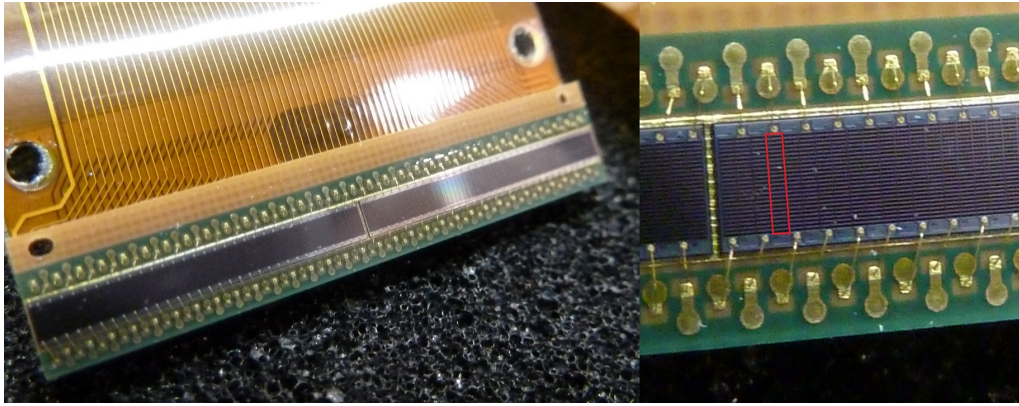


**Figure 4.11:** Photograph of an 128-channel SiPM bonded to a flex-cable. On the right a detailed view is shown. One channel with  $4 \times 24$  pixels is outlined red.

## Electronics

The SciFi-specific electronics are separated in front-end and back-end. They are situated at the detector (as part of the module) and outside the cavern in the counting house respectively. The front-end electronics provide the digitisation and clustering, the back-end electronics are processing these data (see Fig. 4.12).

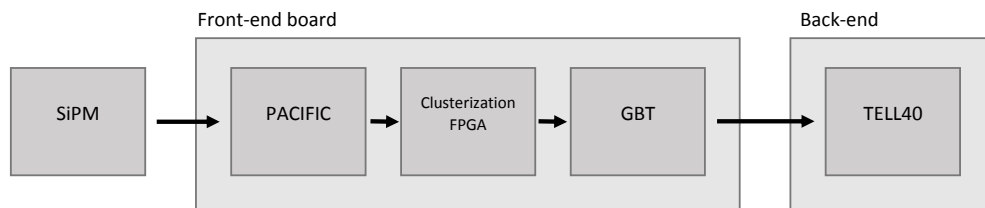


**Figure 4.12:** Scheme of the read-out electronics. The PACIFIC ASIC digitises the SiPM signal. Clusters are formed on a dedicated Field Programmable Gate Array (FPGA) and transferred to the back-end electronics with the help of a GigaBit Transceiver (GBT).

The signals of the SiPM are digitized by a custom designed ASIC called PACIFIC (see Fig. 4.13). The current of the SiPM is amplified, shaped and integrated over 25 ns. The digitization is performed with a non-linear 2 bit ADC, comparing the signal to three individual thresholds. Each PACIFIC handles the data of one SiPM dye, namely 64 channels. The ASIC is under development, as of May 2015 8-channel prototypes are available. The PACIFIC uses two interleaved gated integrators to avoid dead time. The goal is to count all photons of one particle hit. But nevertheless the output is dependent of the arrival time of the signal (the entrance of the photon). Figure 4.14 shows the time dependent output for different input levels (number of photo) for the current bunch crossing (BX0)

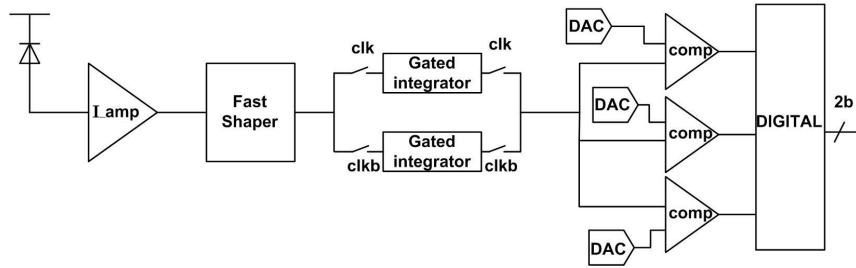


**Figure 4.13:** Scheme of the read-out ASIC PACIFIC. [7]

and the subsequent bunch crossing (BX1). Photons which arrive late in the 25 ns window will produce a lower signal. This decreases the signal of the photons which do not travel directly in the direction to the SiPMs, but are reflected at the mirror in the middle of the detector. As stated before in the fibre subsection photons might also arrive outside the 25 ns integration window and will be assigned to the next bunch crossing.

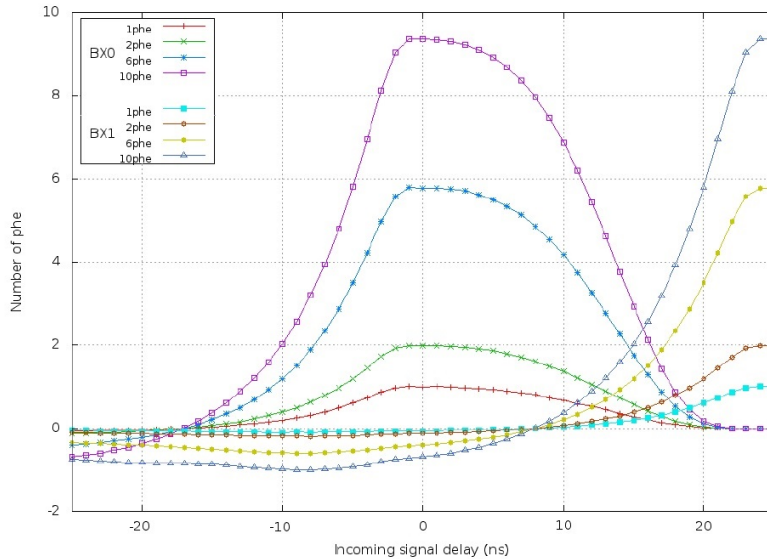


**Figure 4.14:** Relative output of the integrator as a function of the time of detection of a photon at the SiPM. The output is shown for different input signal amplitudes (number of photo electrons, phe). BX0 refers to the current bunch crossing, BX1 to the subsequent one. The offset of the x-axis is arbitrary, the shift has to be optimised. [55], modified

Thresholds are included to distinguish signal from noise. This clustering also serves as zero suppression and reduces the required bandwidth after the ASIC. A typical signal of a particle produces light in several fibres which point to more than one SiPM channel (see Fig. 4.6 on page 33). Three different comparator values (thresholds) are set. When a signal in one channel exceeds the highest threshold (e.g. 3.5 p.e.), it is directly accepted as cluster,

it is unlikely that a noise signal reaches that height. When a cluster does not exceed the high threshold it has to fulfil multiple criteria. At least one channel has to exceed the seed threshold. Together with neighbouring channels (exceeding the neighbouring threshold) they need to pass a sum threshold (this threshold is not a comparator but is applied on the clustering FPGA).

### 4.3.2 Geometry

This subsection describes how all components are arranged and produced to one tracker. The fibres are glued to six-layer mats which are supported by sandwich-structured panels. The fibre mat width is chosen that it matches four SiPMs of 128 channels and four of the mats in width are carried by one panel. The SiPMs and the front-end electronics are situated in so called Read-Out Boxes (ROB), which are attached to the top and bottom of the panels. The solid ends of the panels serve as attachment point to the frames.

#### Mats

The scintillating fibres are arranged in six-layer fibre mats to achieve a sufficient light yield. The fibre is delivered on a spool with the length corresponding to about one fibre mat. It is important to ensure that all fibres are arranged parallel with (small) constant distances. For this, they are wound on a threaded wheel with a pitch of  $275\ \mu\text{m}$  (see Fig. 4.15). The pitch is chosen larger than the nominal fibre diameter to be able to tolerate fluctuations in the diameter. The tension on the fibre is controlled and monitored to ensure a reliable positioning without damages. After finishing the first layer, the fibre is fixed and cut at the end and glue is applied on top of the layer. The first layer serves as thread for the second layer which is wound on top before the glue is cured. Like this, a stack of six layers is completed. The edges of the mat are not produced vertically but like a trapezium, they are wound oversized in width and cut to the correct width later. After the glue is cured the mat is cut orthogonally at a designated position and unfolded. Titanium dioxide is mixed in the glue to turn it white to reduce the cross talk in between fibres.

The fibre mats are aligned to the panels with precision pins (see chapter 5). Special shaped slots are inserted in the wheel surface (see fig. 4.16) which are filled with glue during the winding of the first layer. They result in plastic pins which are positioned along the middle fibre of the mat. The winding procedure and the pin shape were developed by the Dortmund SciFi group, they are explained in detail in chapter 5.

The glue layer on top and on bottom of the mat is very thin, it needs an additional protection for handling and shipping. The mats are laminated from both sides using a  $25\ \mu\text{m}$  thin polyimide foil. These are glued to the surface by hand, where one of the foils has dedicated (oversized) holes for the pins. With the help of the foil the surface and the fragile edges are protected. Before the development of the foil lamination, the baseline option was to cast the mats in a special jig with additional glue. Like this an extra layer of  $80\ \mu\text{m}$  was

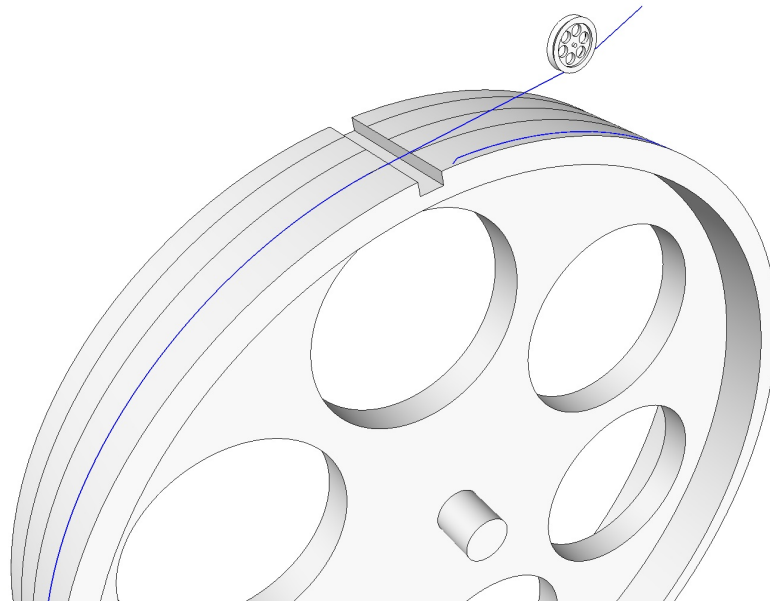


**Figure 4.15:** Sketch of the fibre winding wheel. The pitch is drawn exaggerated to make it visible. In this picture the wheel turns anti-clockwise and the fibre is laid down from the front to the back.

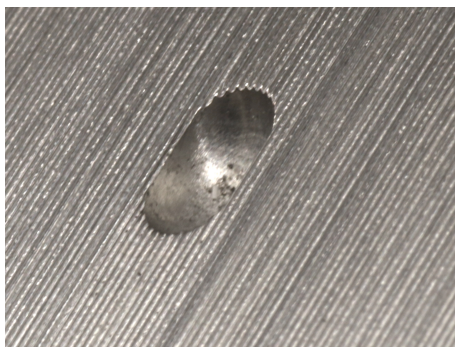


**Figure 4.16:** Pin insert in the winding wheel. It has steep edges parallel to the fibres to ensure a good alignment.

#### 4 The Scintillating Fibre Tracker

added on top and bottom. This would have required more specialised tooling, thus the foil lamination is preferred. At this stage the fibre mat is quite rigid and can be shipped. This enables the separation of the production to different institutes. In addition so called endpieces are glued to both ends of the fibre mat. At the mirror end they serve as protection during the optical cutting, at the other end they are also the mounting of the SiPMs. For this they are equipped with precision holes.

Supported by the plastic endpieces, the ends can be cut to achieve the correct length and the needed optical quality. Now the mirror is glued to the fibre mat. An aluminised Mylar foil is used. Different mirroring techniques were investigated and the Mylar foil showed the best results (optical and handling) [56]. Reflectivities of more than 80 % were reached with fibre bundles.

The mats are cut longitudinal to the correct width with precisely aligned rotating saw blades. After this the production of the fibre mat is complete and it can be positioned in the supporting structure. Figure 4.17 shows the boundary between two fibre mats in the first full size prototype SciFi module (built for the Engineering Design Review (EDR)).

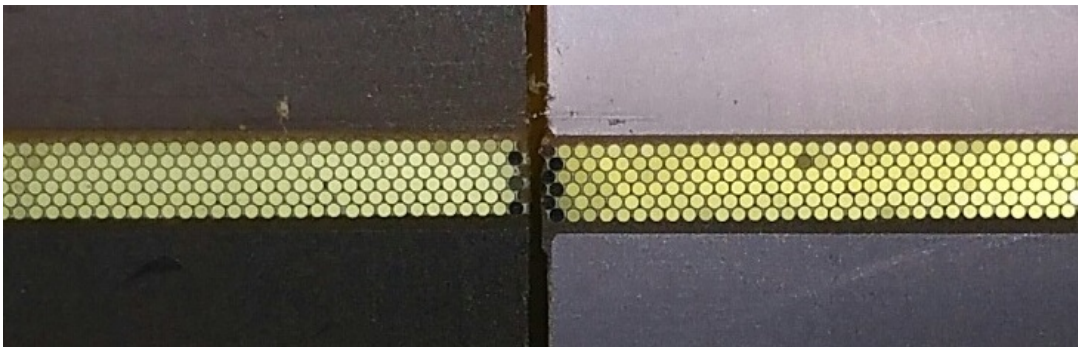


**Figure 4.17:** A boundary between two fibre mats in a module. Light is injected in the fibres and reflected at the other end (the mirrors are mounted). The fibres which appear black are cut somewhere along the length.

#### Support

The supporting panels have to provide good stiffness in combination with a low material budget. The first point is needed to ensure a reliable positioning of the fibres in the LHCb detector. The position of the detector channels can be aligned in hardware and (after that more precisely) in software, but it needs to be stable in time. The detector needs to be light to limit the number of multiple scattering which affects the resolution.

The fibre mats will be centred in a sandwich structure of honeycomb and carbon fibre. The honeycomb structure separates the carbon fibre sheets which are inelastic, this combination ensures the stiffness of the panel. Alternatives to honeycomb were also considered, this is described in chapter 5. At each end of the 5 m high panels, the honeycomb is replaced by



so-called end plugs made of aluminium (outside the LHCb-acceptance). The end plugs carry the mounting to the frames. In addition they serve as connection to the read-out box. A schematic of these components is shown in Fig. 4.18.

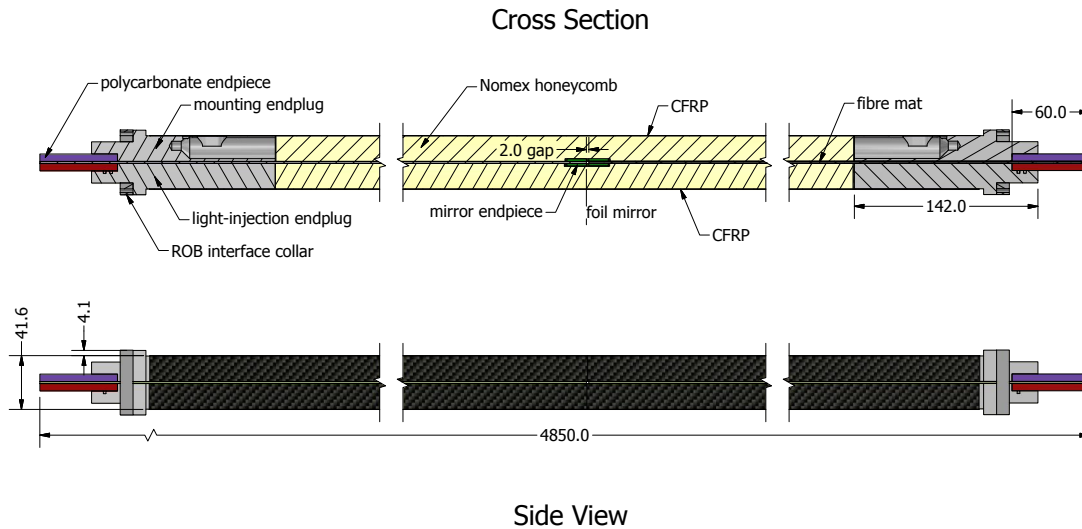


**Figure 4.18:** Schematic of a SciFi module. The fibre mat with attached end-pieces is glued in between a sandwich structure from honeycomb and carbon fibre. The end-plugs serve as mechanical connection to the Read-Out-Box and the frames. [8]

To get a module, eight fibre mats have to be precisely positioned in between the panels. This is done with the help of a precise template. The mats and panels are glued in a multi step process in which each of them is positioned with respect to the template. Like this, no precision holes or groove is needed along the panels to guide the fibre mats while glueing. In a first step the fibre mats are aligned on the template with the help of their pins and one half panel is glued to the other side of the mats, it is aligned to the template with the help of the end-plugs. After the glue is cured the half-module is turned and the second half-panel is glued on top, aligned by the end-plug with respect to the template. This way the fibre mats are kept straight by the template and only the end pieces are aligned to the end plugs which carry precision holes and pins.

The radiation lengths of the materials used are listed in table 4.2. The fibre mat contributes with about 40 % of which about 60 % is active material (fibre cores). Hence about 25 % of the material budget is active material.

To predict the influence of different environmental parameters, finite element calculations were performed [57]. The deformation under different loads was simulated (as example see fig. 4.19). In addition, the influence of temperature differences during production and in operation were investigated. It could be concluded that the deformations during handling and in operation are all uncritical.

**Table 4.2:** The material budget for a single SciFi module in the main part of the panel, given as fraction of the respective radiation lengths  $X_0$  (the region of end plugs and end pieces contains more material). Data taken from [8].

Material	Thickness( $\mu\text{m}$ )	Layers	$X_0(\text{cm})$	$X/X_0(\%)$
Core	20000	2	1310	0.305
CF skin	200	2	23.3	0.172
Panel glue	75	4	36.1	0.083
Fibre mat	1350	1	33.2	0.407
Casting glue	120	2	36.1	0.066
Total	42290			1.02

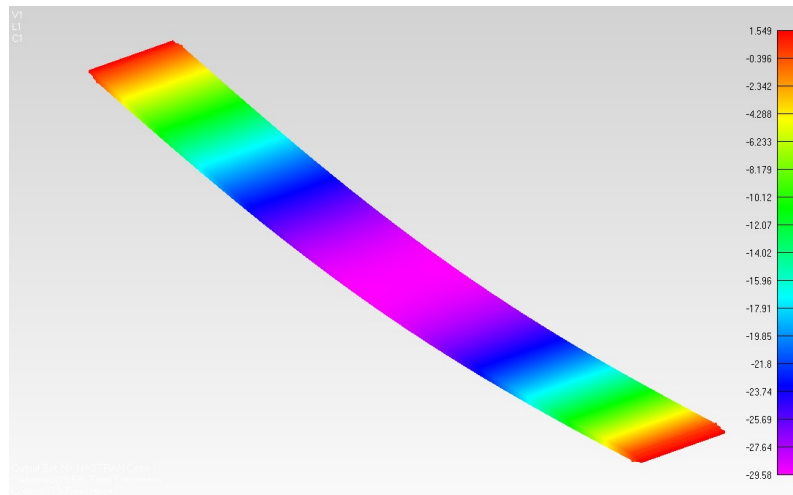


**Figure 4.19:** Simulation of the deformation of a module through its own weight. The colour code shows the deformation in mm. [57]



## Read Out Box

As motivated in section 4.3.1 the SiPMs need to be cooled down to  $-40^{\circ}\text{C}$  to reduce the dark count rate to a reasonably low level. The current through these devices is low and because of this the heat produced is little. Cooling single SiPMs down to  $-40^{\circ}\text{C}$  is fairly simple to achieve. But in case of the SciFi Tracker with about 150 m of multichannel SiPMs there are challenges to overcome. The cooling causes condensation and frost building of the humid air. This requires insulation and isolation of the SiPMs. The inner part of the insulated cold box can be flushed with dry air, while the outer surface needs to be warm enough to stay above the dew point. The Read-Out-Box (ROB) consists of two parts. The cold box houses the SiPMs with the cooling bars while the electronics are separated. Figure 4.20 shows a cross section of the cold box. The delicate part of the insulation are the sides, the borders to the neighbouring modules (not visible in the picture). The insulation needs to be thin to keep the dead regions small.

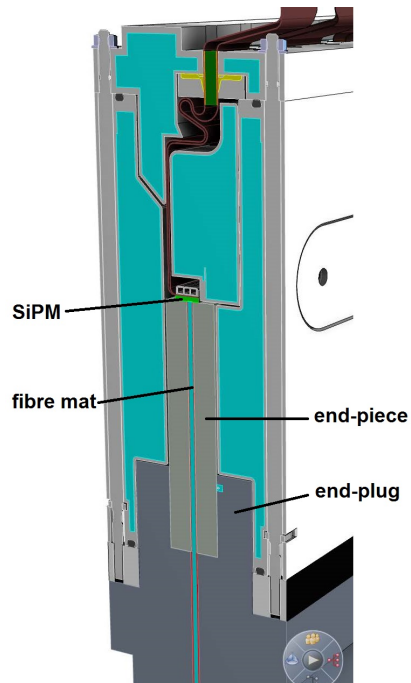


**Figure 4.20:** Schematic view of the cross section of the cold box which is part of the read-out box. The insulation material is shown in cyan. [58], modified

Several options for the cooling were considered (thermoelectric and different liquid cooling options), a single liquid cooling was chosen as the most robust solution. The SiPM arrays are cooled via a pipe which is pressed to them with the help of springs. A second challenge are the different thermal expansions of the materials, the design has to try to avoid mechanical stresses. For this reason the cooling pipe is split in segments which are connected by bellows. One important criterion is the temperature gradient along the pipe,

#### 4 The Scintillating Fibre Tracker

which needs to stay below 1 K along one SiPM die [7]. The temperature influences the over voltage and with this parameters like the gain and the cross talk.

So far simulations and measurements of mock-ups could be performed [7]. They show that the heat load of one ROB is below 20 W, which corresponds to 6 kW for the entire SciFi Tracker and that the requirements can be fulfilled.

#### Infrastructure

The SciFi Tracker is arranged rather similar to the current layout of Inner- and Outer Tracker. The detector is built of three stations with four layers each, arranged in an x-u-v-x geometry. The single modules are attached to so-called C-Frames, each carrying two layers of one side. These 12 C-Frames are carried by the table at the bottom and the bridge at the top (see Fig. 4.21). They are mounted on rails, so it is possible to slide them out (away from the beam pipe) for maintenance.

The bridge and the table installed can be re-used with small modifications [7]. Technically it would be possible to just modify the C-Frames as well, but the tight schedule for dismantling the current detector and installing the new one requires pre-assembly of the C-Frames on the surface.

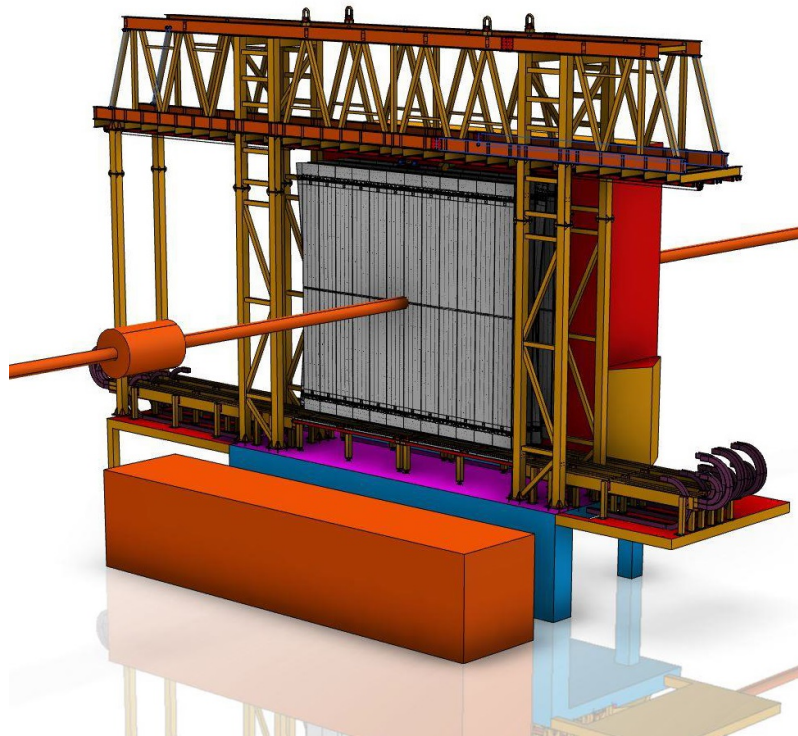


**Figure 4.21:** Bridge and table of the T-stations carrying the SciFi Tracker modules [58].

The cooling infrastructure matches the modular design of the tracker. The supply of the ROBs was chosen to be implemented with serial connections. The low radiation level, the constant temperature in the cavern and the unimportance of the material budget makes it possible to use reliable well known components. As cooling liquid Novec<sup>TM</sup>649 was chosen. In contrast to Perfluorohexane C<sub>6</sub>F<sub>14</sub>, which is widely used as cooling liquid at the LHC, it is environmental friendly (with a Global Warming Potential<sup>10</sup> of 1 instead of 7400). It has very similar properties, so that C<sub>6</sub>F<sub>14</sub> can stay as backup solution.

### 4.3.3 Schedule

The start of the production of components for the SciFi Tracker starts in Q1 2016 with the delivery of the first fibres. Shortly after they are processed to fibre mats, which are combined with the panels to modules. The components for the SiPMs and electronics are purchased from external companies and tested. They are installed in the Cold Boxes and Read-out Boxes. The frames are equipped with the finished modules on the surface, and tested before they are installed in the cavern. More detailed information can be found in [59].

Table 4.3 lists the main milestones for the production of the SciFi Tracker, as respective Engineering Design Reviews (EDR), Production Readiness Reviews (PRR) and the start and end of the production of the individual components. Technology defining reviews and documents are listed in chapter 4.2.

### 4.3.4 Performance

The requirements for the SciFi Tracker are listed above in chapter 4.1 (page 25). The low material budget is guaranteed by the design of the support panels. The trigger-less readout is reached by the fast electronics including gated integrators. The hit efficiency and the hit resolution are driven by the signal to noise ratio throughout the runtime of the experiment.

To quantify the performance of the detector with respect to the requirements, measurements are performed by the LHCb SciFi group in the laboratories and at test beam campaigns. Not all the right conditions can be achieved in the measurements, for this dedicated simulations are performed.

### Test Beam

Two test beam campaigns were carried out in 2015. Small modules of the size of a single fibre mat were built for this purpose and tested for their light yield, single-hit efficiency

---

<sup>10</sup>The Global Warming Potential is a relative number, comparing the greenhouse effect of the respective gas to the same amount of carbon dioxide.

<sup>11</sup>Includes the installation of SiPMs and electronics and the testing.

**Table 4.3:** Main milestones for the production and installation of the SciFi Tracker. The dates are mainly taken from [59].

Component	Start date	End date
<b>Modules</b>		
EDR		Q3 2015
Fibre delivery	Q1 2016	Q1 2018
PRRs Fibre Mats	Q1 2016	Q2 2016
Fibre mat production	Q2 2016	Q2 2018
PRR Modules		Q2 2016
Module production	Q2 2016	Q2 2018
<b>SiPMs</b>		
EDR		Q2 2016
SiPM delivery	Q4 2016	Q2 2017
SiPMs tested		Q4 2017
<b>Electronics</b>		
EDR		Q2 2016
PRR PACIFIC		Q2 2017
PACIFIC production		Q3 2017
PACIFIC packaging and testing		Q2 2018
PRR boards		Q2 2017
Board production	Q2 2017	Q3 2018
<b>Cold Box &amp; ROB</b>		
EDR		Q2 2016
component production	Q4 2016	Q2 2017
production complete <sup>11</sup>		Q4 2018
<b>Frames</b>		
EDR		Q4 2016
Frame delivery		Q2 2017
Frame assembly	Q2 2017	Q2 2018
<b>Installation</b>		
module installation to frames	Q2 2018	Q2 2019
remove IT & OT		Q2 2019
SciFi installation		Q3 2020

and resolution. The device under test in the first test beam was a module based on the actual design of a SciFi module including a six-layer fibre mat. An eight-layer mat with increased pitch (see chapter 5.2.3) was added for the second test beam. Both mats were wound at TU Dortmund. The final electronics with 40 MHz were not yet available, the SiPMs were read out with slow electronics which have the advantage of an ADC with finer steps (compared to the PACIFIC read-out with a 2-bit ADC). Combined with a long shaping time (with a constant gain for all photons of an event) it is possible to measure the photo-electron spectrum of the signal which is not possible with the comparator based PACIFIC electronics.

The single-hit efficiency and the spatial resolution are measured with the help of telescopes. These detectors with multiple tracking layers define whether and where a particle crossed which is compared to the measurement of the fibre detector under test. The simplest telescope is to use the information of the additional fibre modules installed in the beam.

The fibre module is tested at different positions along and across the fibres and under different angles. Figure 4.22 shows the collected charge at the position close to the mirror. The mean number of photons detected (photo electrons) is 16.5. The width of the distribution is caused by the fluctuation of the particle path length through the cores of the fibre, the energy deposited in these, the photons produced by this, the number of photons lost along the length of the fibre and the amount of them which is detected by the SiPM (in addition the signal includes the cross talk of the SiPM).

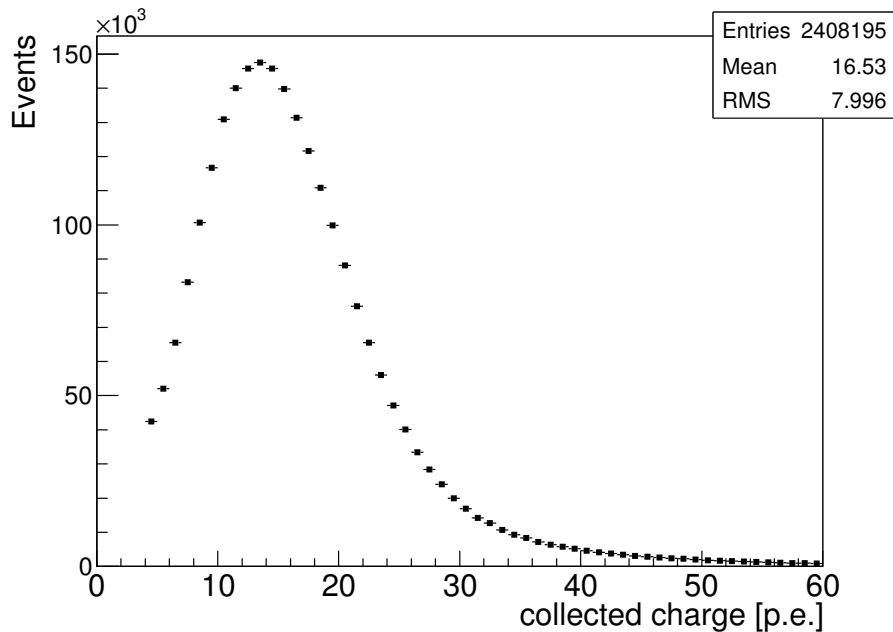


**Figure 4.22:** Collected charge distribution (light yield) close to the mirror. [8]

The hit position in a fibre module is calculated as weighted average over the channels in the cluster. Therefore the spacial resolution is better with increased light yield (due to

smaller relative uncertainties). The read-out with the real comparator based electronics can not profit as much from the weighting as with a finer ADC, therefore the spacial resolution is slightly worse. The resolution measured close to the mirror is  $79.11 \pm 0.52 \mu\text{m}$  for the charge weighting and  $85.34 \pm 0.54 \mu\text{m}$  for a PACIFIC-like weighting [8].

The fluctuation of number of photons detected cause a certain amount of events which stay below the thresholds of the clustering (these thresholds are needed to reduce the noise rate caused by the thermal noise of the SiPMs). These events cause the drop of hit efficiency to lower than 100 %. Figure 4.23 shows the single-hit efficiency as a function of the position vertical to the fibres (in SiPM channels) for different clustering thresholds. The average efficiency for the design cluster threshold is  $98.66 \pm 0.04 \%$  [8].

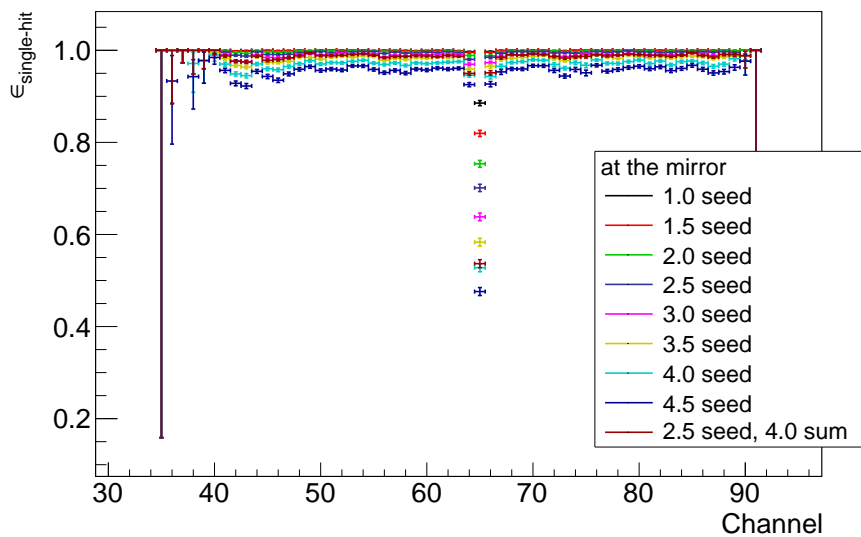


**Figure 4.23:** Single-hit efficiency (particle hit to cluster) close to the mirror for different positions across an SiPM array for different cluster thresholds (the legend lists the seed thresholds). SiPM channel 65 corresponds to the gap between the dyes. [8]

The lower the mean number of photons, the greater the ratio of events which stay below the thresholds. Thus, the single-hit efficiency is a function of the light yield. To show the dependency, several data points from various positions along different modules with five and six layers and with and without mirror, are combined in one plot, see Fig. 4.24.

The 8-layer mat with increased pitch shows a slightly increased efficiency (not included in the plots). This is caused by the more homogeneous structure<sup>12</sup>. A technical note with detailed information and results of the test beam campaigns in 2015 is currently (effective winter 2015/16) under preparation [61].

<sup>12</sup>The minimum path length through a 6-layer mat is three fibre diameters while it is four for an 8-layer mat although the mat is not much thicker due to the increased pitch.

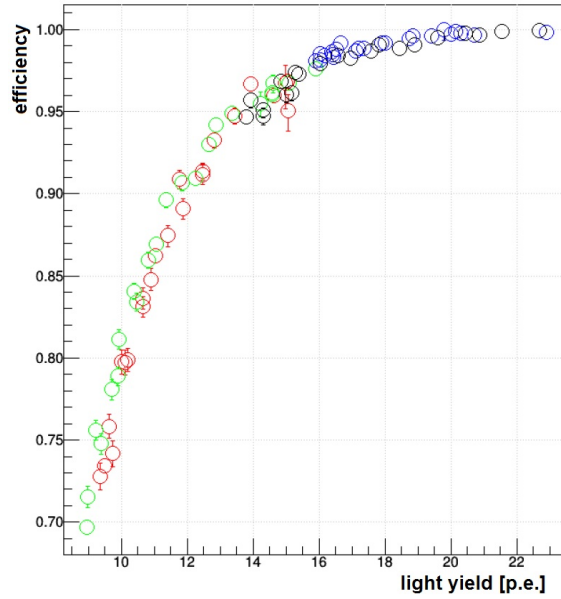


**Figure 4.24:** The single-hit efficiency determined in the test beam analysis as a function of the corresponding mean light yield. The data points were obtained for different modules (5-layer (green&red), 6-layer (blue&black)) and different positions along the modules. Some of the data points were obtained without a mirror. [60], modified

## Simulation

To evaluate the performance of the SciFi Tracker at LHCb Upgrade conditions, simulations are essential. The different components (fibres, SiPMs, electronics, panels, cooling) are studied with dedicated detailed simulations in the LHCb SciFi group. In addition, effective models are used to simulate the whole SciFi Tracker as part of the Upgrade detector to study the tracking performance.

At the time of the Technical Design Report [7], the signal flow of the detector was roughly implemented as follows: Dead regions are included in the geometry. Particles crossing an active part of the detector deposit energy in the fibre mat material, where the fibre mat is made from homogeneous rectangles in line with the SiPM channels. The deposited energy is attenuated as a function of the position in the detector to account for the attenuation in the fibres. This attenuation map is computed for the direct and the mirrored photons separately using a parametrisation of the attenuation as a function of the dose, obtained from lab measurements. The position of the hit across the SiPM channel is used to calculate the signal distribution to the neighbour channels. The position of the particle hit along the fibre mat defines a time of arrival for the direct and the mirrored photons. This is used to compute the attenuation due to the time dependence of the electronics. Finally the noise of the SiPMs and electronics is added, comparator thresholds are applied and clusters are built.

#### 4 *The Scintillating Fibre Tracker*

The cluster charge distribution and the single hit efficiency of the simulation was compared to the test beam measurements<sup>13</sup> in the Dortmund SciFi group. It is found that it is possible to adjust the average light yield to the correct level, but the distribution is too narrow which leads to overestimated hit efficiencies. Therefore a new implementation of the signal height computation from energy deposition is developed with large contribution from the Dortmund group. This implementation uses the geometry of the single fibres to calculate the signal height for every channel in a cluster. In addition, the attenuation maps are produced with the help of a detailed single fibre simulation (see chapter 6). Effective winter 2015/16 this is work in progress, but the first results show a good agreement between simulation and measurements.

The simulation is used to predict the performance of the detector for the whole lifetime. The innermost region of the detector is affected the most from irradiation damage (see chapter 4.3.1 & 6). The attenuation in the fibres increases which leads to a reduced light yield resulting in a drop of single-hit efficiency. To compensate this, the implementation of additional tracking layers for the innermost modules is currently studied. This might recover the tracking efficiency<sup>14</sup>.

---

<sup>13</sup>The simulation of the SciFi Tracker was modified for this to reproduce the test beam setup.

<sup>14</sup>Adding tracking layers enables to increase the tracking efficiency without increasing the rate of ghost tracks by adapting the tracking algorithms.



# 5 Module construction for the Scintillating Fibre Tracker

This chapter describes the design of the fibre mats and modules in more detail. It focuses on the evolution of the module design and the production process of the fibre mats, because these are the parts where contributions were made in the course of this thesis.

## 5.1 The design of the SciFi modules

After the establishment of the Central Tracker as an option for the LHCb Upgrade in the Framework TDR [47], concrete R&D started on how to design the modules. Independent of the construction of the fibre mat, the design of the support panels and the SiPM cooling enclosure were planned. The design criteria are:

**Stiffness** The purpose of the support panels is to provide the needed stiffness for the fibre mats. The aim is to position all the fibres straight and parallel. Some misalignment can be corrected in software, the most important requirement is therefore that the positioning is stable in time.

**Material budget** To limit multiple scattering, the material budget should be kept small. A certain amount of material is needed to guarantee the desired stiffness. The only possibility to reduce it, is to use the same support for more than one fibre mat layer, the so-called bi-layer design explained below.

**Manufacturability** A simple and modular design is beneficial to limit the required research and development. It also eases the production of the modules in reducing the number of different parts which need to be produced.

To achieve a uniform material distribution, a support built as sandwich panels was agreed on from the beginning. It is based on a core with low density and carbon fibre skins. Two different arrangements were discussed. The so-called mono-layer design has the fibre mat in the middle of two half cores and the skins, while the bi-layer design arranges two fibre mats symmetrically on the outside of the skins of a sandwich.

But in fact the bi-layer modules would not be completely symmetric. It combines a vertical and a stereo-angle fibre mat, which is rotated by  $5^\circ$ . This would cause a non-overlap width of about 22 cm (of 50 cm panel width) at the outer ends. Additional central skins in this regions would be necessary to try to compensate for that. Moreover, the fibre mats would

require a protection and light sealing from the outside which would further increase the material to close to the mono-layer panels.

An additional design criterion is the choice of the top/bottom and middle boundaries of the stereo layers, whether to cut these perpendicular to the fibres or parallel to the vertical modules, see Fig. 5.1. The tapered cut at the SiPM end would require slightly different fibre mat widths. On the other hand, the perpendicular cut introduces boundaries of different temperature between modules. The choice for the perpendicular cut of the fibre mats in the middle of the module required tuning of the tracking algorithms. Before, the track finding was separated in an upper and lower half. This is not possible any more with the saw-tooth cut in the stereo layers, because the two halves of the detector layer are interleaved.

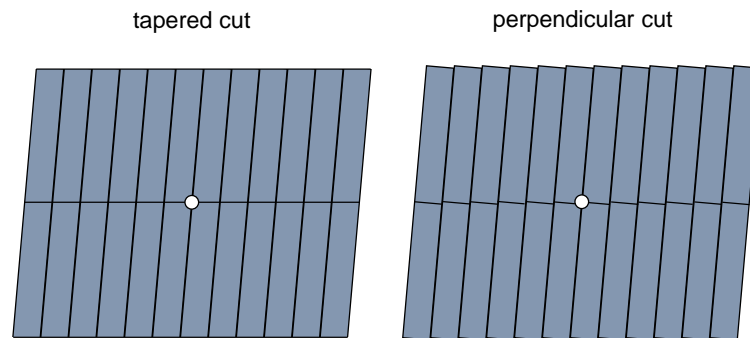


**Figure 5.1:** Schematic drawing of a stereo layer with tapered cuts on the left and perpendicular cuts on the right.

After weighing of the advantages of the different techniques it was decided to go with the cleanest most modular design: mono-layer panels with perpendicular cut fibre mats at both ends [62]<sup>1</sup>. This choice has the advantages of a complete symmetric structure and the same module design for the vertical and stereo modules (except for the innermost modules with the beam-pipe cut-out).

Different materials for the core were suggested and compared (structural foam and honeycomb). The foam has advantages in the precision of the edges which is essential for some designs. The chosen production concept transfers the precision from the fibres through the pins to the panels with the help of precise templates. This allows to use a core made from honeycomb, which has a lower average density. As explained in chapter 4.3.2 the precision of the fibres is transferred to the detector frames via the end-plugs and to the SiPMs via the end-pieces.

---

<sup>1</sup>The perpendicular cut at the mirror side was decided later, after it was shown that this does not introduce problems in tracking.

## 5.2 Winding of fibre mats

The production of fibre mats from a spool of scintillating fibres is the most delicate, time consuming, and labour intensive process in the module production. The major part of the fibre mat production is the winding of the fibres on a rotating base to a fibre matrix. The group at TU Dortmund worked on the winding method the last five years, major contributions were made in the course of this thesis. This chapter describes different winding concepts and different detail solutions which result in the final method. Special challenges for the winding are explained which result in the design of the prototype winding machine. From the experience gained with this prototype, a machine for the serial production was developed together with a company.

### 5.2.1 Winding concepts

A fibre mat of a width of  $\varnothing$ (10cm) and a few layers requires more than a thousand 2.5 m long fibres arranged parallel to each other with a precision better than 100  $\mu\text{m}$ . For the final design of a full SciFi Tracker with 6-layer fibre mats, this sums up to about 3 million fibres of 2.5 m length which implies a highly automated production. Previous experiments mainly worked with fibres laid down by hand side by side or in grooves (e.g. for HERMES [63]).

The possibility to produce fibre mats by an industrial partner was studied in the LHCb SciFi group [64]. It was found that several companies work with comparable products (e.g. textile industry), anyhow it would require a huge R&D effort for them to plan and manage the production. A production at an external partner requires precise specifications and well defined and performed quality control. These agreements need to be defined early. It was concluded that this can not be achieved. Retrospectively, one can confirm this, the general parameters such as the quality of the fibres and the design of the fibre mats underlie consistent changes and optimisations till the start of the serial production.

Therefore an LHCb internal R&D was started in 2010 in Dortmund. The first machine developed for LHCb to wind a matrix of fibres was based on a rotating frame, see Fig. 5.2. The basic principle is adapted from machines to wind wire chambers. The fibre feeding is adapted from the fibre scanning machine developed in the group [65–67]. The tension of the fibre is given by the weight of a loose spool. A more detailed description of the feeding unit can be found in Sec. 5.2.4.

The fibres are laid down side by side and pre-guided by a small spool which is precisely moved on a slide with a stepping motor (see Fig. 5.2, right). This guidance spool moves a step of 250  $\mu\text{m}$  every full turn of the frame. The experience gained with the rotating frame showed that small irregularities can cause disorder of the matrix. This can be caused by deviating fibre diameters or drops of glue (the smallest drop size achievable is greater than the cross section of a fibre). Due to the necessary low tension on the fibre, the force to keep the new fibre in line is very small.

## 5 Module construction for the Scintillating Fibre Tracker

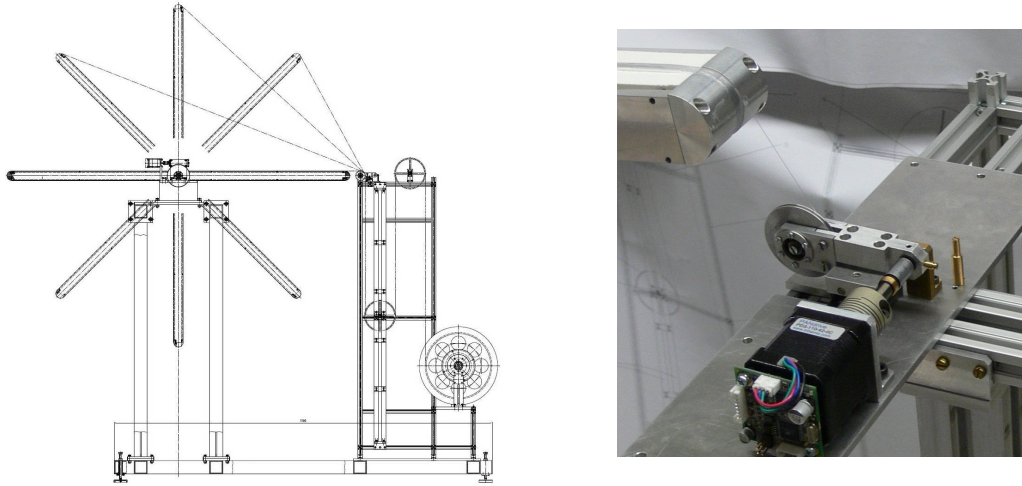


**Figure 5.2:** Fibre winding machine based on a rotating frame. Left: Construction drawing, the flat frame is shown in multiple angles on the left, while the fibre feeding unit is placed on the right. Right: Picture of the guidance spool and one end of the rotating frame.

An alternative approach to the flat frame was tested at CERN. Instead of the frame, a rotating wheel is used. The method is based on the procedure used in the fibre mat production for the PERDAix Experiment by the group at RWTH Aachen<sup>2</sup> which itself is similar to the one used for the CHORUS scintillating fibre tracker (see Fig. 5.3) [68–71]. In this first test for LHCb, the fibre was wound on a wheel of about 1 m diameter without grooves, the fibre was laid down side by side guided by hand. A photograph of the winding is shown in Fig. 5.4 and a cross section of the mat in Fig. 5.5. The pressing of the fibre next to each other is not a reliable and reproducible procedure for the serial production, it was performed to save the milling of the thread.

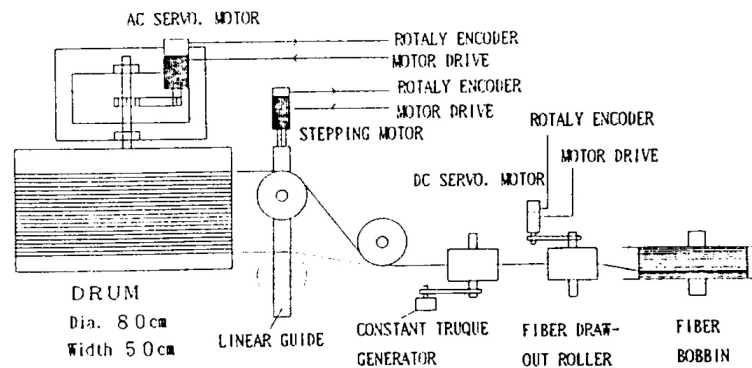


**Figure 5.3:** Schematic view of the fibre winding machine for the CHORUS scintillating fibre tracker [71].

<sup>2</sup>The Aachen group was not part of the LHCb SciFi group at that time but collaborated with the Dortmund group in general R&D for scintillating fibre trackers with SiPM read-out.

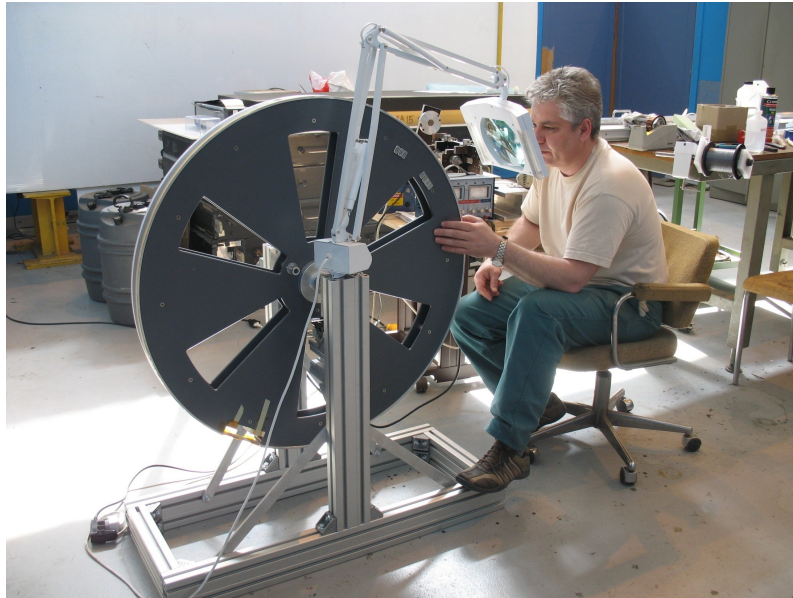


**Figure 5.4:** Photograph of the winding of a LHCb prototype mat at CERN. The fibre is guided by hand to lay down side by side. [72]



**Figure 5.5:** Cross section of a hand wound 2.5 m fibre mat on a wheel without a groove. [47]

## 5 Module construction for the Scintillating Fibre Tracker

One issue of the winding on a wheel was that the tension of the fibre needed to be adjusted from layer to layer in order to obtain a flat mat after removing it from the wheel. The experience with the large test wheel<sup>3</sup> showed that the mat stayed sufficiently flat without adjusting the tension. However, aligning the fibre by hand next to each other is not feasible for the serial production. But due to this promising test, it was decided to produce a large wheel with a thread.

The first large test wheel with a thread was produced in house at TU Dortmund. It replaced the rotating frame in the prototype winding machine, the linear slide of the guidance spool was adapted to the greater width of 160 mm. A more detailed description of the machine can be found in the dedicated section (Sec. 5.2.4). Since then the machine and the wheel are used to optimise the winding technique details. In addition, a small wheel was built which can be re-machined more easily to test new ideas.

One important step in the production is the application of the release agent. This is required to enable the removal of the mat from the wheel. In case of inaccuracy or failing agent, the mat is glued to the wheel, which destroys the mat and might damage the wheel. Because of this, an alternative was proposed by the CERN group. A Coverlay<sup>TM</sup> patterned Kapton<sup>®</sup> foil is wrapped around a wheel without grooves. The pattern is applied in a photo-imageable process and serves as guidance for the fibres. It is realised as parallel lines with a rectangular cross section. After finishing the mat the foil stays attached to the mat, a new patterned foil is used for each mat, so that no cleaning of the wheel is necessary.

The CERN group provided a patterned foil to perform a test on the Dortmund machine. For this, the foil was attached to the threaded wheel and a full fibre mat was produced, a photograph of the winding process is shown in Fig. 5.6. The winding process itself went fine, but two problems were noticed afterwards. In an area of about 4 mm, one additional fibre was merged in the first layer (the pitch of the fibres in this area is smaller than the one given by the Coverlay pattern), see Fig. 5.7. This region shifts diagonal across the mat and is probably caused by the improvable alignment of the foil on the wheel which could only be performed by hand at that stage. The second issue is caused by the elasticity of the fibres. The tension applied expands the fibre by about 1 cm per turn, after the vertical cut and the taking off of the mat it contracts again. The tension of the whole mat is so high that it contracts the Kapton foil underneath, but the foil gets wavy at the sides where no fibres are glued to it. This is the region where markers are included which should be used to transport the alignment of the groove pattern to the further steps in the processing (cutting and glueing to the support). This is not possible with the wavy foil, it prohibits a proper alignment. Because of this it was chosen to stick to the threaded wheel.

The application of the glue is performed by hand and it would be preferred to apply the glue automatically if possible. For this a glue dispenser with a brush was used. The dispenser pushes an adjustable amount of glue in adjustable intervals in the brush. Two different methods were tested. In the first case the fibre is guided through the brush before it is laid on the wheel (see Fig. 5.14 on page 66). In the second approach the brush is placed on the

---

<sup>3</sup>The diameter of the winding wheel for the production for PERDAix is only 300 mm, matching the shorter length of the modules.

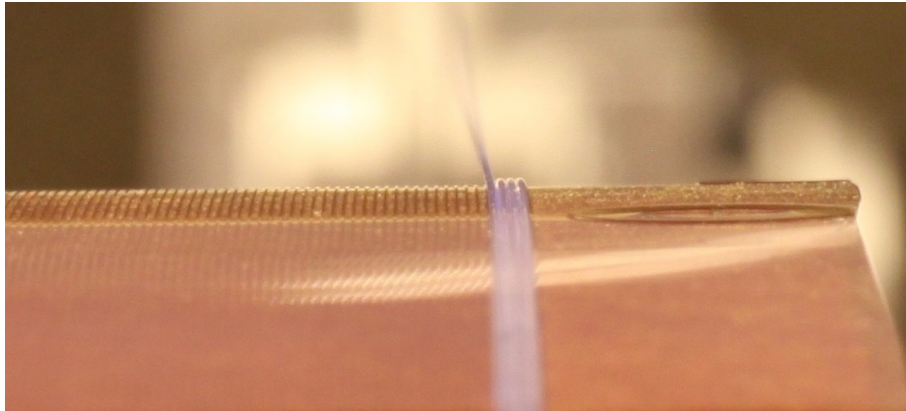


**Figure 5.6:** Fibre mat winding on a Coverlay patterned Kapton foil. The picture is taken tangential to the wheel three turns after the start of the first layer. The fibre is guided by the groove pattern on the foil.

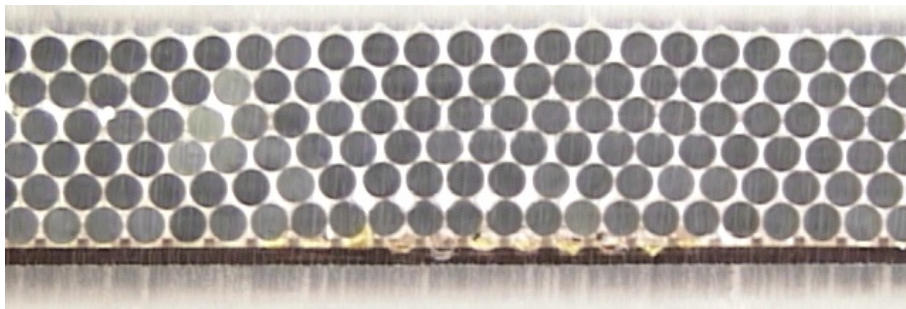


**Figure 5.7:** The cross section of the fibre mat wound on the Coverlay foil. The foil and the pattern are visible. The photograph shows the region with the additional fibre in the first layer, the fibres are not positioned in the grooves. [73]



fibres which were laid down, a few turns after the newest fibre. In both cases it was found that it is not possible to tune the amount of applied glue to the correct level. Moreover, the glue does not spread even enough, so that one nevertheless has to distribute it by hand. That is why it was agreed to apply the glue manually after each layer.

### 5.2.2 Alignment of the fibre mat

The final fibre mats need to have a rectangular cross section, such that they can be placed side by side in the module. It would be beneficial to achieve this shape with the correct width directly through the winding procedure. It was tested to achieve a vertical edge of the mat by the help of a sidewall. This was performed with the rotating frame in Dortmund. It was found that the placement of the fibres was not reliable and a trapezoidal shape which is cut rectangular afterwards is preferable. In addition to the placement of the fibres, a flat surface is beneficial in terms of manufacturing, mat removal and cleaning.

One of the challenging parts of the winding process which involves human influence and experience is the start of a layer. The fibre end is fixed nearby the grooves with the help of a screw and guided to its designated groove by hand. In order to achieve a reliable trapezoidal matrix corresponding clamps were designed<sup>4</sup> (see Fig. 5.8). These clamps guide the first fibre of each layer to the correct groove, a different clamp is used for each layer. It was found that many clamps would be needed along the circumference to guide the fibres, and it was not possible to achieve a perfect trapezoidal shape. Therefore the edge of a fibre mat can not be used to align the fibres.

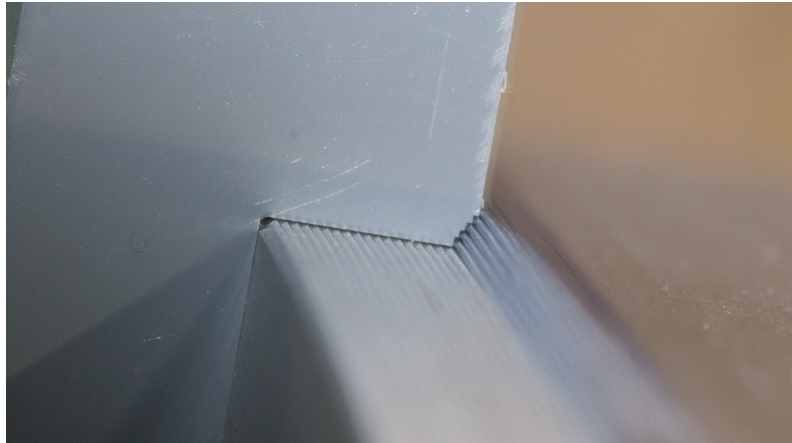


**Figure 5.8:** A fibre guiding clamp attached to the edge of the winding wheel. The photograph shows the clamp for the fifth layer only. It guides the fibres to a trapezoidal shape. This test winding was performed without glue.

<sup>4</sup>The clamps were designed by Alexander Trofimovich from Institute for Theoretical and Experimental Physics in Moscow who was situated in Dortmund at that time.



The thread in the wheel keeps the fibres straight and parallel during winding. But after removing the mat from the wheel, this reference is lost and the position of the fibres along the mat is not known any more. Different approaches were tested to align the mats to the support. Shining light in one fibre and aligning the opposite end is appropriate for short mats, but the long mats are too flexible so that the straightness in between the ends can not be guaranteed like this. A second optical method tested was the colouring of the central fibre which can be used to align the fibre mat with the help of a microscope, but the colouring was not reproducible enough. To achieve a better contrast a thin wire was glued in a fibre groove of the top layer instead, like this an optical alignment was possible. However, an alignment by eye is time consuming and not reliable enough, a mechanical method was preferred.

The preferred realisation should transport the position of the fibres, which is given by the thread in the wheel, to the position of the fibres in the final module, any intermediate steps would increase the uncertainty. The chosen method (described in chapter 4.3.2) is based on alignment pins. These pins are formed from glue during the winding process by insertions in the winding wheel. They are used in further processing to align the mat for the long cut, to align the end-pieces (which align the SiPMs) and to align the mat on the support panel.

The shape of the pins was optimized in steps. The design needs to combine a precise alignment vertical to the fibres, a shape which allows easy extraction and producibility. Different shapes tested in the small wheel in Dortmund are shown in Fig. 5.9. A cylindrical pin sticks in the pin-hole too well, that is why a small cylindrical base with a hemisphere was proposed which was implemented in the large wheel built in Aachen. Several tests were performed in Aachen and in Dortmund and it was found that the contraction of the mat after the vertical cut (see chapter 6.2) tends to shear the pins of the mat. The tension of the single fibre is 50 cN, summing up to about 1.5 kN for the entire mat. The final design takes this into account by lowering the angle of the pin hole in the direction of the fibres (see Fig. 5.10, a photograph is shown in Fig. 4.16 on page 41). This way the pin can push itself out when it is pulled by the fibre.

### 5.2.3 Influence of diameter fluctuations of the fibres

After the alignment of the fibre at the starting edge, the winding of a layer runs very smooth in case of no disturbance. As mentioned in chapter 4.3.1 and further discussed in chapter 6.2, the diameter of the fibres is not constant. The normal fluctuation of the diameter is not critical for the winding process, but at random distances ( $\mathcal{O}(1\text{ km})$ ) the diameter is increased for a few millimetres to values greater than the pitch of the grooves. This can cause a jumping of the fibre to the next groove or disorder layers above.

Dedicated simulations were carried out to investigate the influence of these so-called bumps on the winding process [75, 76]. A random fibre diameter was simulated with normal pieces of fibres and bumps. Figure 5.11 shows an exemplary result of such a simulation.



**Figure 5.9:** Different shaped prototype pin holes in the small Dortmund wheel. The cylindrical hole on the left is realised with a Teflon<sup>®</sup> inlet to avoid the need of a release agent.

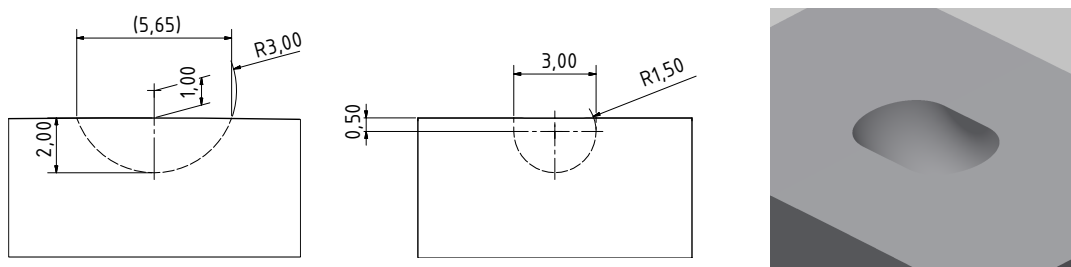


**Figure 5.10:** Drawings of the final alignment pin-hole shape. The holes are aligned along the circumference of the wheel. They have rectangular edges on the side (parallel to the fibres) and sloping ones in the direction of the fibres. [74], modified

It can be seen that nearly all disordered fibres originate from a bump. But in fact small dispositionings like this are not a big issue since they affect only a few fibres in a mat.

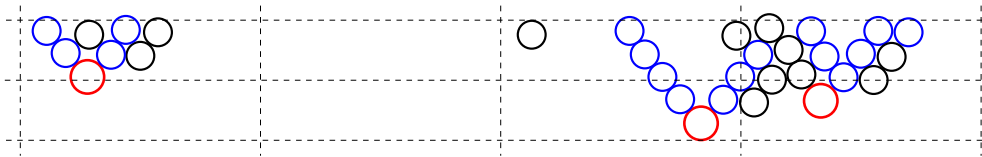


**Figure 5.11:** An exemplary result of a simulated fibre mat cross section. Fibres with about  $300\ \mu\text{m}$  diameter are shown in red. Fibres with a diameter of about  $250\ \mu\text{m}$  are shown in black when their offset to their nominal position is greater than  $10\ \mu\text{m}$  and in blue when their offset is greater than  $20\ \mu\text{m}$ . Fibres with offsets within  $10\ \mu\text{m}$  are not shown. It is visible that nearly all disordered fibres originate from a bump. Data taken from [75].

The jumping of a fibre to the next groove is more difficult to simulate. It is not only the diameter which causes the jumping, other parameters like the tension perpendicular to the fibre, the amount of glue, the wobbling of the wheel and vibrations have great impact. Some bumps which cause a jump during the winding at the first place, can still be included in the mat by reducing the speed of the wheel at this position<sup>5</sup>. In case a bump is too large to be included without a jump or it would cause disorders in the higher layers, it has to be removed. A missing fibre can not be tolerated, it causes great disorder in the layers above.

A technique was developed to cut out the bumps without degrading the performance of the mat or wasting too much fibre. For this, the region of the vertical cut is used. This is where the mat is cut to be removed from the wheel. In the course of the further processing, the mat is cut to a shorter length. Thus, this position is a region with a length of about 10 cm which will not be part of the finished fibre mat. This place is used to attach fibres without optical connection. After the jumping of a fibre due to a bump the fibre is wound back to before the jump and is glued to its neighbour at the vertical cut position with instant glue, see Fig. 5.12. After a few minutes the fibre can be cut. The bump is cut out and the end of the fibre is re-attached, while being glued to its neighbouring fibre.

The time needed for this procedure is about 15 min, the winding of one layer takes 30 to 45 min. Including the time needed for the glueing of the layers and preparations beforehand, one can cut out one bump per layer on average to wind one mat in a working day. The producer of the fibres keeps working on the quality of the fibre but till now it can not be guaranteed that the required maximum of bumps can be reached. Due to this, different alternatives are under test. One approach proposed and currently tested by the Aachen group is to cut out the bumps before the winding. This requires a proper glueing of the ends which is strong enough and does not include create glue bumps.

In addition it was investigated to choose a larger pitch to increase the threshold for bump cut-outs. A pitch of  $350\ \mu\text{m}$  was chosen, which gives about the same average light yield

<sup>5</sup>If the fibre jumps, one stops the wheel and winds back to before the jump. After that the speed of the wheel is reduced till the critical position is passed.

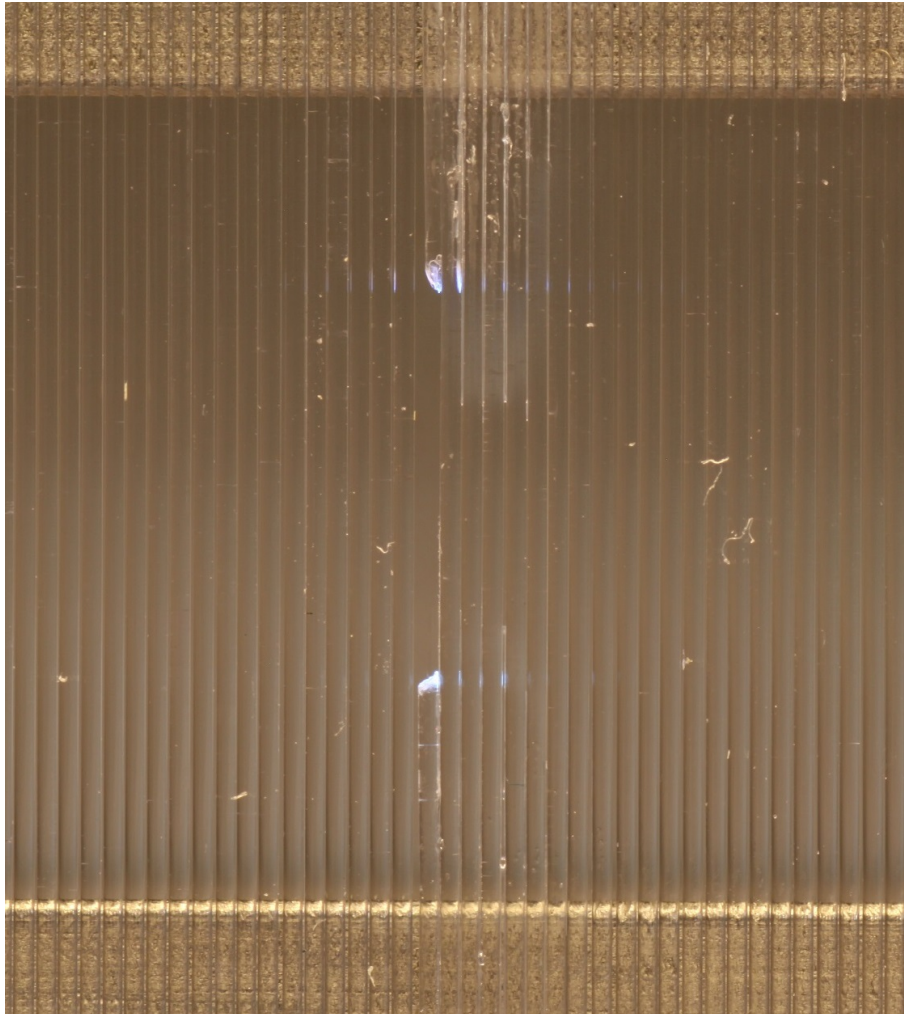


**Figure 5.12:** Cut and re-attached fibre in the first layer on the winding wheel. Light is emitted at the cut fibre ends. They were glued to their neighbour fibres to the right (winding direction right to left). The picture was taken after the layer was completed.

when switching to eight layers of fibres. Due to the more homogeneous distribution of fibres, it is expected to have a slightly increased single-hit efficiency (assuming constant thresholds), which was confirmed by dedicated simulations in the LHCb SciFi groups. Encouraged by this, the Dortmund wheel was re-machined with the enlarged pitch and an according fibre mat was produced. No bumps needed to be cut out. The mat was used in a test beam and the slightly increased single-hit efficiency was confirmed (see chapter 4.3.4). On the other hand the increased height would probably require enlarged SiPMs which would result in increased noise resulting in higher thresholds reducing the single-hit efficiency. It was decided not to switch to the increased pitch in case it is not necessary for the fibre mat production.

### 5.2.4 The prototype winding machine

As described before, the prototype winding machine was and is under constant development. The machine as it exists at the moment was used for the production of important fibre mats and for the development of the serial winding machine and is therefore described in this section.

A photograph of the machine with highlighted fibre is shown in Fig. 5.13, it can be split in three subsystems. The fibre feeding part (on the right) is adapted from the fibre scanning machine developed in the Dortmund group ([65–67]). A loose spool defines the tension (the weight is about 100 g). The position of the spool is controlled with light barriers which detect whether the spool is moving up or down and the motor of the feeding spool will change its speed accordingly. This control loop is realized as program on the controller of the stepping motor and runs independent of the rest of the machine.

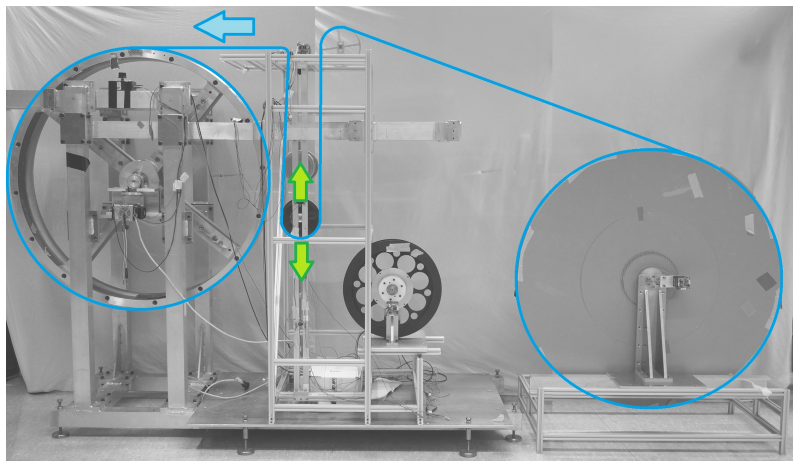


**Figure 5.13:** The prototype winding machine. The blue line indicates the path of the fibre.

The winding wheel is equipped with a thread and pin-holes as described before. The stepping motor reads a potentiometer which controls the turning speed. Although the



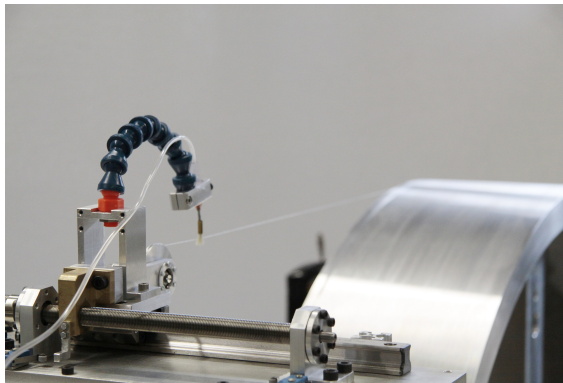


**Figure 5.14:** The positioning spool of the prototype machine moves on a linear rail. In the photograph a dispenser with brush tip is mounted to apply glue to the fibre before it enters the wheel.

acceleration is limited in software, it can not be guaranteed that no slippage occurs. Because of this, the movement of the positioning spool (see Fig. 5.14) is not controlled by the potentiometer. A light barrier reads the turns of the wheel by the help of a mirror mounted to the wheel. Every time the mirror passes the light barrier, the positioning spool is moved by one pitch (nominally  $275\ \mu\text{m}$ ). The distance of the positioning spool to the winding wheel is big enough that moving in this steps is precise enough, the wobbling of the wheel was nevertheless larger for the first iterations. This ensures that the movement is very precise in the long term (along the width of a layer).

The machine is well suited for the development and to produce a couple fibre mats. The modularity achieved by autonomous subsystems is well suited to adapt to changing requirements. Like this it was possible to mount winding wheels of different size (even at the same time), implement external winding wheels<sup>6</sup> and to use different-sized feeding spools. At the same time the machine is not appropriate for a serial production, it requires too much expertise to operate it properly and it does not run reliable enough. Despite the handling the pure production quality fulfils all requirements in terms the quality of the fibre mats. The two major fibre mats used in the test beams and the fibre mats in the EDR module were produced with this prototype machine.

### 5.2.5 The serial production winding machine

Based on the experience in Dortmund and Aachen a machine for the serial production was developed. For this, a list of requirements was defined [77], which helped companies to provide offers. It was decided not to define the properties of the fibre mats produced, this would have required large effort of companies to develop a production method. Instead the gained experience was used to sketch the method and define the parameters and

<sup>6</sup>The first test with coverlay foil was performed on a wheel provided by CERN.

functionality of the machine which then ensures good fibre mats. Rather than listing requirements here, the properties of the machine are described. The machines are produced by STC Elektronik GmbH<sup>7</sup>. The company is specialised in computer based controls for facilities, special machines and interconnected systems. The design of the machine was developed in close cooperation of the company and the institutes. A photograph of the machine in the lab in Dortmund is shown in Fig. 5.15.

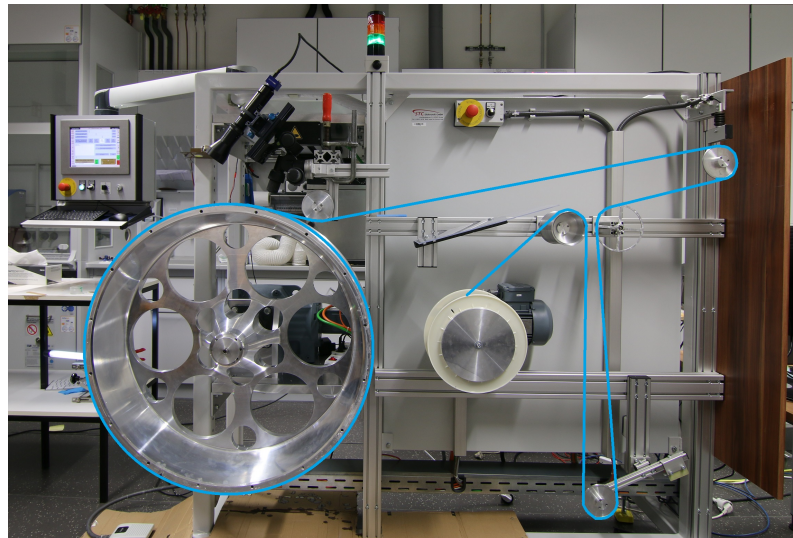


**Figure 5.15:** Serial winding machine in the Dortmund lab. The path of the fibre is drawn in blue.

The general concept of the prototype machine could be adopted, the mechanics were tuned in details. The spools are mounted on one side to enable an easy applying of the fibre (see e.g. Fig. 5.16). The mounting of the winding wheel is also implemented one-sided to enable a quick exchange of the wheel. It is constructed more precise and more rigid to reduce the wobbling and the motor is stronger to enable a faster emergency stop. The positioning spool is moved homogeneously and is mounted close to the wheel, which improves the fibre guidance.

The main difference is the hardware and software which controls the machine and monitors the parameters. The machine is operated via a graphical interface (see Fig. 5.17), it offers different modes for the different production steps in which unnecessary features are disabled. Parameters like winding speed, acceleration, tension of the fibre and the pitch can be changed and are monitored and stored together with the number of turns of the wheel and length of fibre wound. In order to cut out bumps the machine can read in a data file with bump positions (produced by the fibre scanning machine) and stop shortly before it would be wound on the wheel. The movement of the positioning spool is always synchronised to the turning of the winding wheel (in winding mode). But it is possible to set an offset during the winding process, which is sometimes needed to overcome delicate

<sup>7</sup>STC Elektronik GmbH, Krellenhäuser 3, 07973 Greiz, <http://www.stc-forum.com/>

## 5 Module construction for the Scintillating Fibre Tracker



**Figure 5.16:** One-sided mounting of the positioning spool of the serial winding machine. The fibre is guided with the lower part of the spool which enables a large spool and a short distance to the winding wheel.



**Figure 5.17:** Control PC of the serial winding machine. The interface is a mixture of hardware knobs/switches and touchscreen software control.



passages (smaller bumps, start of a layer). All parameters are saved in a log file together with comments added by the operator.

Finally the machine operates safer and more reliable. For the operator it means that the force to the wheel is limited, so that the wheel can be stopped by hand even at full speed. To limit failures, the machine is equipped with an uninterruptible power supply. This ensures that, even in case of power cuts, the wheel is constantly turned in glue hardening mode and the control PC is shut down without data losses.

## 5.3 Quality assurance

The production of more than 1000 fibre mats at four different winding sites requires reliable and standardised quality assurance and quality determination methods. In addition, the determination of the quality of the fibre mats at different steps is essential for the development and the optimisation of the production steps. The R&D in the Dortmund group focusses on fibres and fibre mat winding, so does the quality control of this parts.

The first component to test are the scintillating fibres as delivered by the producer. They are tested for their light guidance and diameter (more sophisticated tests like the light yield and the radiation hardness will only be performed for some samples). Results obtained in the course of this thesis are presented in chapter 6. For the serial production the tests will be performed centralised at CERN.

The essential part in the winding is that the fibre lays down at the correct position. Due to bumps, dust, glue drops and vibrations, it can jump to the next groove or jump back on top of the current layer. It is important to detect defects like this early to correct them, otherwise they will generate large defects in the upcoming layers. The transparency of the fibres and uneven amounts of glue makes it difficult to judge by eye whether the fibre is shifted or not. It was found that looking at the horizon of the mat, tangential to the wheel, gives the best contrast. During the development phase this was monitored with the help of a standard consumer digital single lens reflex camera whose live view video was followed on a monitor. Figure 5.18 shows a photograph of the monitor. The large aperture leads to the effect that one sees the fibre as circles, Fig. 5.19 shows a photograph with a smaller aperture.

Before the introduction of this monitoring method it was not unusual that a layer contained an error. The online control enabled to detect jumps reliable and fast for the first time which increased the fibre mat quality drastically. Like this, it was possible to wind mats from fibres with small bumps without errors. The later developed bump cut out (see chapter 5.2.3) was the next big step, allowing the production of good fibre mats from fibres with large bumps.

During serial production it is not practical to watch a monitor during the complete winding process. For this an automatic error detection is currently under development in Dort-



**Figure 5.18:** Screenshot of the camera picture taken during the winding. The fibre is wound from right to left. The newest fibre shines blue due to its illumination with room light on its path to the wheel.

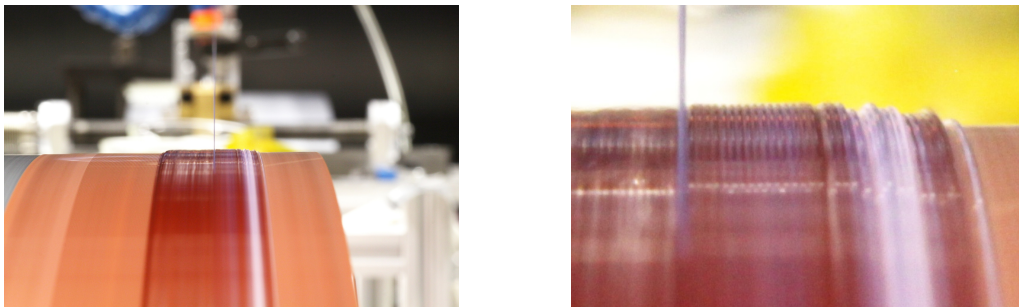


**Figure 5.19:** Photograph taken during the winding of a coverlay mat. The small aperture allows to see the trend of the fibres. The magnified right picture shows the imperfect starting edge of the mat.

mund [78]. It uses the video input from an industrial camera mounted on the linear motion slide of the positioning spool, see Fig. 5.20.

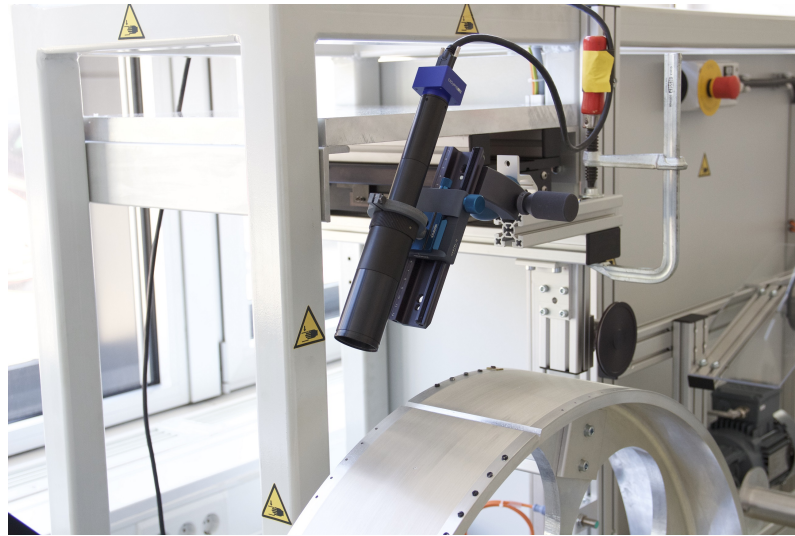


**Figure 5.20:** The industrial camera mounted to the serial winding machine.

After finishing the fibre mat including the optical cut, it is possible to analyse the cross sections at the ends. Just looking at the fibres with homogeneous back light shining through or with front light enables to determine the positions of the fibres at this cross section. This can be performed with the help of automated circle detection [76] and provides a hint whether the winding overall went well. For example it is expected that the average deviation of the perfect distance between the fibres increases from layer to layer. This is a measurement which will be performed with every mat in the serial production.

In the beginning of the development it was not excluded that fibres jumped or crossed, which is not necessarily visible at the end of the fibre mat. It may happen that missing fibres in one of the first layers are filled up by fibres of the subsequent layer, after all layers are finished it will look like an error in the uppermost layer. To identify this it is needed to compare the position of each fibre on both ends. This is possible with the illumination of a few fibres on one end and controlling the pattern on the other end. Figure 5.21 shows the photograph of a cross section for which the other end was attached to a monitor showing a picture of black stripes. This allows a quick check of the fibre mat, to improve this method a display with a higher resolution is necessary.

A similar approach which was tested in the Dortmund group is to use a mechanical slit aperture [79]. Using an aperture narrower than a fibre diameter illuminates one or two fibres (dependent on the position of the aperture). Analysing the photographs of the opposite side enables to detect shifted fibre layers as shown in Fig. 5.22.

These analysing methods which are based on patterned illuminating of fibre mats take more time and are more difficult to automate compared to the homogeneous illumination.

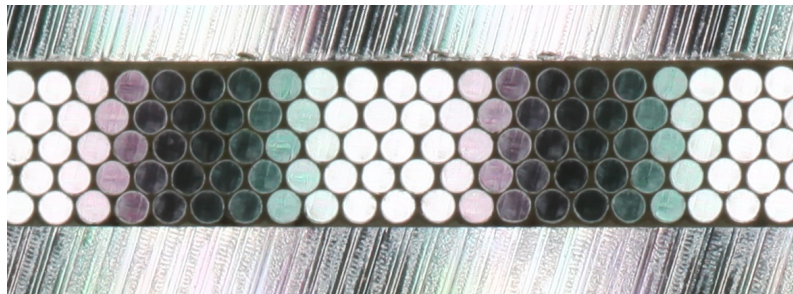


**Figure 5.21:** Photograph of a fibre mat cross section, the other end was illuminated by a screen showing black and white stripes. The green and red colours are caused by the pixel structure of the illuminating screen

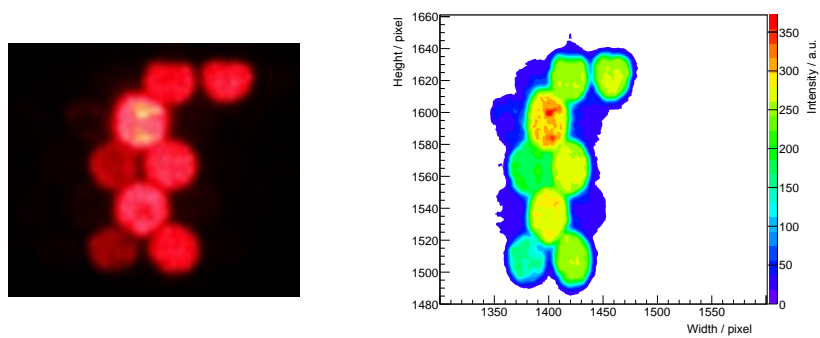


**Figure 5.22:** Photograph of a fibre mat cross section, the other end was illuminated by a laser shining through a slit (left). The right picture shows the colour coded intensities of the photograph. It is visible that the uppermost layer is shifted by one pitch along the length of the mat. [79], modified

Due to the improvement of the winding and the online monitoring it was decided not to further improve these setups. The unlikelihood of a crossing appearing without being detected and corrected during the winding and the small decrease of the performance of the fibre mat in case do not justify an additional quality test.

## 5.4 Serial production

The SciFi Tracker has three stations with four layers each. Each layer is built from twelve modules with two times four fibre mats, this results in 1152 fibre mats (about 1300 mats will be produced to account for possible rejects [8]). Assuming 42 weeks of full production per year and four days a week, five production lines are required to produce all the fibre mats in the scheduled time of 1.5 years. Four winding centres are foreseen (TU Dortmund, RWTH Aachen, EPFL in Lausanne and Kurchatov Institute Moscow) with one running double shifts (Kurchatov).

The complete cycle of winding one fibre mat takes three days. The winding itself takes one working day, followed by 36 h curing time till the mat is taken off the wheel. After that the wheel has to be cleaned and the release agent needs to be renewed. Due to this, each production line uses three wheels which are interchanged. The next steps in the production which require glueing (casting, end-piece glueing, mirroring) also require multiple tooling because of the curing time. The optical cut at the ends enables to test the fibre positions and to test the light yield.

Before applying the longitudinal side cuts, the tested mats are shipped to one of the two module centres (University Heidelberg and Nikhef in Amsterdam). Here, the long cuts are performed and the fibre mats are used to built a module. More detailed information can be found in the Engineering Design Review Report [8].

## 5.5 Summary & outlook

The main challenge of the module production is the fast and reliable processing of the fragile scintillating fibres to precise fibre mats. The displacement of the fibres should be small compared to the envisaged spatial hit resolution of the tracker of  $<100\ \mu\text{m}$ . In order to produce one fibre mat in one working day, the fibres have to be laid down with a minimum speed of  $0.5\ \text{m s}^{-1}$ , which requires an automated procedure. During the processing the force applied to the fibre has to stay below 50 cN to minimize stresses and avoid damage.

A machine to wind multi-layer fibre mats was constructed and built. This machine was used to test different production techniques. The basic principle is adapted from other experiments: The fibre is wound on a threaded wheel and glue is applied on top. This is repeated till the required number of layers is reached, where the respective previous layer is used as the guidance for the fibre. After the glue has cured, the mat is cut perpendicular

## *5 Module construction for the Scintillating Fibre Tracker*

to the fibres at a designated position, and taken from the wheel. To achieve a raw fibre mat length of up to 3 m, a threaded wheel with about 1 m diameter was produced in-house. The fibre is guided to the wheel with a spool positioned on a linear slide, the tension is given by the weight of a loose spool. This prototype machine was built from autonomous, modular sub-systems, such that new technologies could be implemented and tested easily.

Even after production, the fibre mat is a fragile and flexible object. In order to position it in the detector, it is aligned to the sandwich support panels with the help of alignment pins. These pins are produced from glue through slots in the wheel. The shape of these alignment holes was optimised in several steps to ensure an easy removal of the mat from the wheel. The tension applied to the fibres during the winding process leads to a contraction of the mat of about 1 cm at the perpendicular cut. The developed pin hole shape is designed such that the pin pushes itself out of hole when pulled along the fibre direction.

In the course of the evolution of the SciFi Tracker project, the fibre mats of the respective latest design were produced with the help of the prototype machine, to name but a few, the first full size fibre mat, the first 6-layer mat, the final-design fibre mat for the test beam and the eight fibre mats for the first module, produced for the Engineering Design Review. Thus, the feasibility of the production procedures was proven. With the help of the gained experience, a winding machine for the serial production was designed in collaboration with a company. The principle design is adapted from the prototype machine. It is optimised for the increased requirements on reliability, operability, and working safety. Four machines were constructed by the company and were handed over to the winding centres.

The procedures developed will be implemented in the production of about 1300 fibre mats at the four winding centres. As one of these, 20 % of the fibre mats are planned to be produced by the Dortmund SciFi group. The Production Readiness Review for the Dortmund group will take place in Q2 2016.

# 6 Scintillating fibres research

At first the general principle of light production and guidance in the scintillating fibres is summarised. The following sections present more detailed aspects, which were studied in the course of this thesis. The focus is on the attenuation of the light travelling along the fibres. Especially the effects of the angle of the photon tracks and of radiation damage is determined. Results obtained in supervised bachelor theses are respectively referenced.

## 6.1 Basic principle

The principle of function of scintillating fibres can be split in the production of light and the light guidance along the fibre.

### 6.1.1 Scintillation

The scintillating fibres for the LHCb SciFi Tracker are multi-cladded plastic fibres<sup>1</sup>. The core is based on polystyrene which is an organic scintillator. Ionizing particles excite the valence electrons from benzenoid rings in the  $\pi$ -orbitals of the polymer [80]. These electrons can emit scintillation photons during relaxation.

But pure polystyrene has a low scintillation light yield, that is why a dopant is added [81]. With a high enough concentration (typically 1 %) the distances are short enough that the energy can be transferred radiation-less via the so-called Förster Transfer [82]. Figure 6.1 includes the emission and absorption spectra of polystyrene and p-Terphenyl, which is the dopant used for the LHCb fibres. The emission spectrum of p-Terphenyl lies at too low wavelength to be used as single dopant, the absorption of the polystyrene and losses due to scattering are too high [81].

To achieve a better separation, a second dopant is added which emits in the transparent region of polystyrene. The LHCb fibres use tetraphenyl-butadiene (TPB) [7] which is added with lower concentration to avoid too much self-absorption (see Fig. 6.1). The lower concentration does not enable the energy to be transferred locally, the second dopant acts as wavelength shifter (WLS), absorbing the emitted photons of the first dopant, re-emitting them at higher wavelengths. A low concentration can cause photons of the first dopant to leave the fibres before they are absorbed by the WLS which can reduce the light yield,

---

<sup>1</sup>The fibres used in all studies in this thesis are Kuraray SCSF-78MJ.

while a higher concentration increases the self-absorption. Simulation studies with varying WLS concentrations are described in [54].

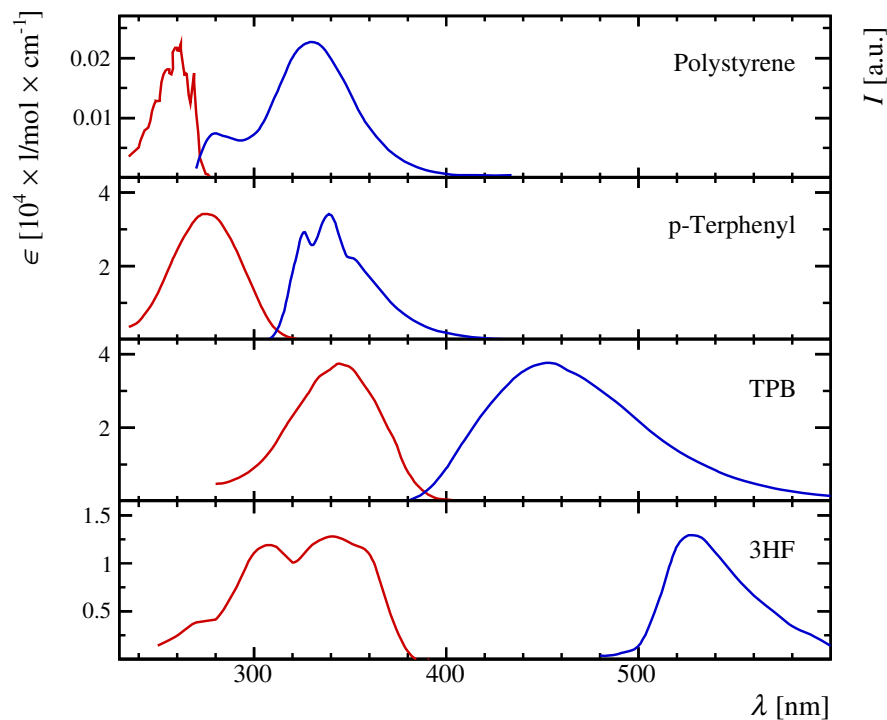


**Figure 6.1:** Absorption (red) and emission spectra (blue) of some compounds used for scintillating fibres. The absorption is shown as the decadic molar attenuation coefficient and the emission as intensity (number of photons) in arbitrary units. Polystyrene is the core material and p-Terphenyl and TPB the primary and secondary dye of the Kuraray SCSF-78MJ, the data is obtained from [83]. 3HF is an alternative dye with a larger Stokes Shift, the data is obtained from [84]. The figure is taken from [54].

Figure 6.1 also shows the spectra for the dopant 3-HF, due its larger Stokes Shift it is more transparent and especially more radiation hard (the radiation damage is smaller at higher wavelengths, see chapter 6.4). But due to its lower initial light yield and its slow timing characteristics it can not be used for LHCb [7].

The spectrum of a scintillating fibre at varying distances to the photo-detector is shown in Fig. 6.2. The maximum of the spectrum shifts to higher wavelength with increasing distance to the photo-detector. This is caused by the higher absorption at low wavelengths, mainly due to the self-absorption of the wavelength shifter.

Recently a new type of scintillating material was developed in which so-called Nanostructured Organosilicon Luminophores (NOL) are mixed to the polystyrene base material [85].

<sup>2</sup>0.1–0.6 m: 0.1 m steps, 0.6–3.0 m: 0.2 m steps, 3.0–12.0 m: 0.6 m steps.



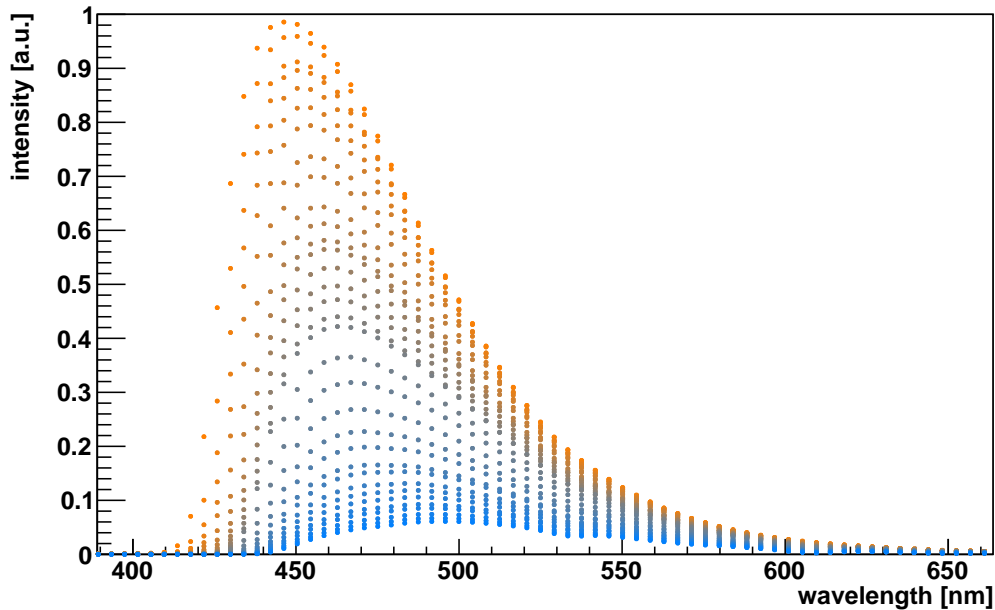


**Figure 6.2:** The spectrum of a scintillating fibre for different distances to the detector from 0.1–12 m (orange to blue, the distances are not equidistant<sup>2</sup>). The spectra were recorded with a spectrometer which was pre-calibrated by the manufacturer.

In traditional scintillators the first dopant and the wavelength shifter are randomly distributed in the base material, whereas the NOL material couples the dopants with bridges of Silicon nanoparticles, see Fig. 6.3. With this method, the efficiency of the transmission of photons from the first dopant to the WLS can be improved, resulting in an increased light yield (up to about 50 % are reported in [85]). This is especially beneficial in thin scintillating fibres, where the chance of photons (emitted by the first dopant) to leave the fibre before exciting the WLS is particularly high.

The LHCb SciFi group initiated the collaboration of the NOL manufacturer LumInnoTech<sup>3</sup> with the fibre manufacturer Kuraraya and first fibre samples including NOL material were received and tested [8]. The development is still in an early phase and the parameters need to be tuned (e.g. the concentration of the material). However the first results are already promising, the best fibres reached the light yield and attenuation lengths of the standard fibres. In addition to the potentially increased light yield, the possibility to tune the spectrum of the emission offers a great opportunity. NOL fibres which emit in the green are being produced, which do not suffer from long decay times (in contrast to 3-HF). These will probably show a lower effective radiation damage.

<sup>3</sup><http://www.luminotech.com>

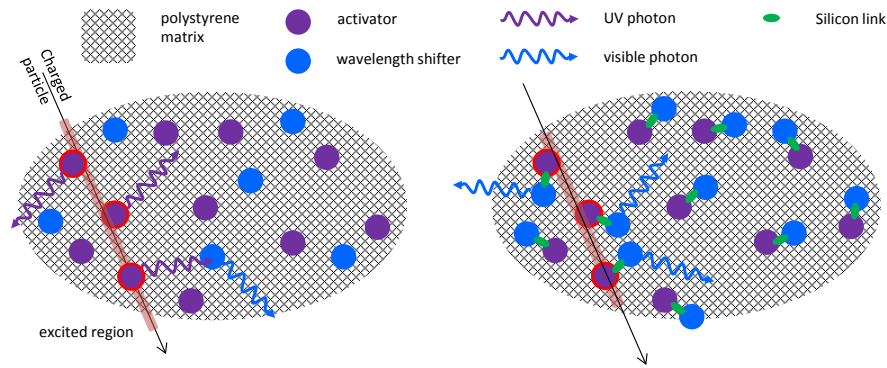


**Figure 6.3:** Simplified principle of NOL scintillators. The left plot shows a standard scintillator, photons emitted by the first dopant can be lost before exciting the wavelength shifter. The right plot shows a NOL scintillator. The WLS is coupled to the first dopant, resulting in an increased light yield. [86]

### 6.1.2 Light guidance

The photons are guided along the fibre with the help of total reflection, therefore the claddings have decreasing indices of refraction (see Fig. 6.4, the inner cladding is only needed for a proper bonding). The light of the wavelength shifter is emitted isotropically, but photons emitted under the proper angle are only a small fraction. The trapping efficiency for photons emitted from the axis of the fibre is given by  $\frac{1}{2}(1 - (n_{clad}/n_{core}))$  [81] for one hemisphere which gives about 5.3 %.

For skew light rays following a helix path (see Fig. 6.4) the trapping efficiency increases (for photons emitted uniformly over the cross section the efficiency is  $\frac{1}{2}(1 - (n_{clad}/n_{core})^2)$  for single cladded fibres), but these photons are attenuated more due to a higher amount of reflections at the core cladding boundary. The expected effective gain in trapping efficiency from these light rays is in the order of 10 to 30 % [87].

The light guided along the fibre is subject to different attenuations. The photons can be absorbed, scattered or lost at the boundaries (due to scattering) instead of being reflected. The first two factors scale with the photon path length and are shown in Fig.,6.5. The absorption in pure polystyrene is dominated by electronic transitions below 450 nm and by scattering above. Molecular vibrations are of minor importance in the spectral range of the scintillating fibres. Although the concentration of the second dopant is rather small, the re-absorption of wavelength shifted photons is the major source for light losses in the scintillating fibre below 450 nm.

The attenuation factors mentioned above are all fixed and could only be improved by changing the composition of the fibres. In reality, the fibres are not perfect and additional factors increase the attenuation. The photons can be scattered at dust particles or absorbed in foreign matter like water. In addition the photons can be lost at the boundary between core and inner cladding or between the claddings instead of being reflected or refracted.

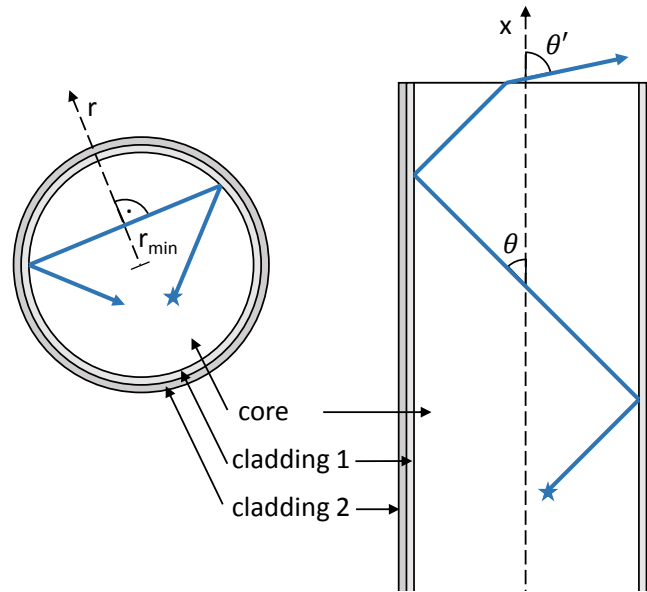


**Figure 6.4:** Fibre total reflection scheme. The value  $r_{\min}$ , the closest distance of the photon path to the fibre axis, defines the skewness. The angle  $\theta'$  is the exit angle of the photon, which is used in the analysis.

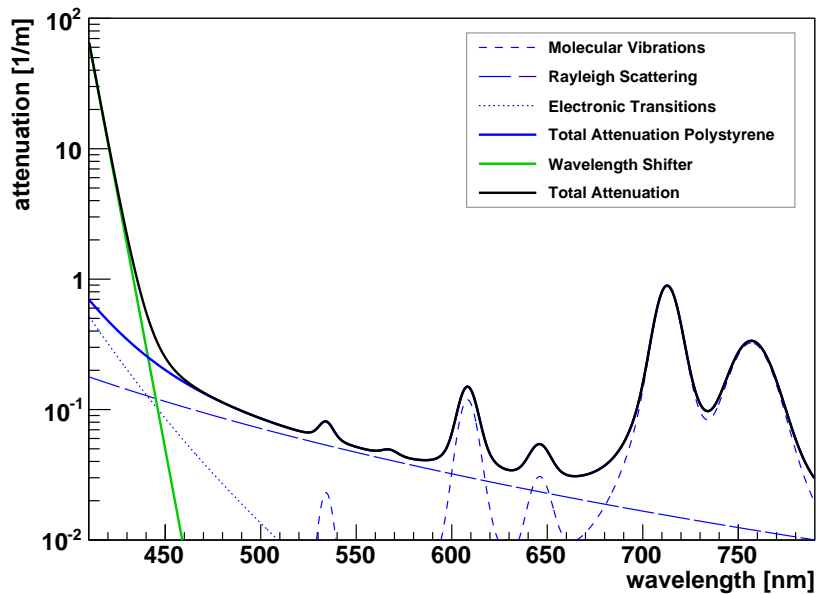


**Figure 6.5:** The basic attenuation coefficients relevant for the scintillating fibres. The attenuation in pure polystyrene is due to rayleigh scattering, molecular vibrations and electronic transitions. The re-absorption of the wavelength shifter TPB is the dominant factor for the attenuation in scintillating fibres. The data is taken from [54].

This is the only factor of attenuation which does not scale with the path length but with the number of reflections.

The path length and the number of reflections scale with the angle. The track length  $L$  as function of the distance  $x$  and the angle  $\theta$  is given by [88]

$$L = \frac{x}{\cos \theta}.$$

The number of reflections  $N$  additionally depends on the closest distance of the photon path to the axis  $r_{\min}$  (relativ to the core radius  $R$ ), the number increases when the path is “more skewed” [88]:

$$N = \frac{x \tan \theta}{2\sqrt{R^2 - r_{\min}^2}}.$$

This leads to the fact that light which travels under large angles, especially in a strong helix shape, is highly absorbed. The angular behaviour of the attenuation is studied in chapter 6.3. The angle quoted in the measurements is the photon exit angle in air  $\theta'$ .

### 6.1.3 Radiation Damage

In addition to the initial attenuation the transparency is further harmed by irradiation. The expected dose for the SciFi Tracker is largest close to the beam-pipe (30 kGy) and falls rapidly to the outside (see Fig. 4.7 on page 34). The irradiation damage of scintillating fibres is a complex process and still lacks a proper description. The attenuation increases with the applied dose due to the formation of absorption and scattering centres from free radicals (like benzyl, cyclohexadienyl and possibly others [89]). Annealing of these damages occurs through re-combination of the radicals among themselves or with oxygen.

Considering different radiation damage studies of scintillating fibres lacks consistent and conclusive results [90]. It is essential to perform own irradiation tests with conditions as close as possible to the real conditions. The forming and annealing of radicals strongly depends on the structure and environment. The availability of oxygen strongly influences the radiation effects, for example in forming absorption centres during annealing [91]. During irradiations at high dose-rates the oxygen is consumed faster than it can diffuse into the fibre, while at low dose-rates oxygen is available throughout the irradiation [92]. This may lead to a dose-rate dependence of the damage. Additionally, the annealing of absorption centres may be influenced by the kind of particles used [93].

Different types of damages are observed, permanent and short-lived annealing ones. The main damage for scintillating fibres is observed as tails of permanent absorption centres in polystyrene peaking at short wavelength (250–320 nm [89]). Scintillating fibres with different dopants show divergent short-lived absorption centres at higher wavelength (500–700 nm [94] [95] [96]). The permanent damage is observed to grow linearly with dose (additional attenuation per dose [ $\text{m}^{-1} \text{kGy}^{-1}$ ]) while the annealing one grows faster at low doses [89] [94].

Additional damage may occur when the quality of the core cladding interface is harmed by irradiations. A larger damage in the transmission loss of clear fibres with respect to polystyrene discs is observed, which could be explained by this [54]. The transmission loss in the claddings due to irradiations is of minor importance due to the fact that permanent damage in PMMA is expected to be comparatively small [54] and the relative path length of the photons in the cladding is low (see chapter 6.3).

Damage to the scintillation and wavelength shifting processes are not expected in the dose range relevant for the LHCb Upgrade. Designated measurements did not show any effect [7].

## 6.2 Mechanical properties

The light production and light guidance are important for the performance of the tracker. Mechanical properties are those which are important for the fibre mat winding. The elasticity of the fibre leads to a contraction of the fibre mat after taking it from the wheel. Diameter fluctuations influence the positioning of the fibres.

A certain tension is needed during the winding to enable a reliable positioning of the fibre in the thread. The standard force used is 50 cN<sup>4</sup>. The extension of a 30 cm long fibre was tested with different weights, see Fig. 6.6. The result gives an extension of  $(7.0 \pm 0.5) 10^{-5}/\text{cN}$  which corresponds to an elastic module of  $(2.3 \pm 0.2) \text{ kN mm}^{-2}$ . For a force of 50 cN and a wheel circumference of 280 cm the contraction of the fibre mat is expected to be about 1 cm, which is also observed in the production of fibre mats, see Fig. 6.7. This contraction was a challenge for the design of the alignment pins and a reason not to further follow the coverlay winding technique, see chapter 5.2.1.

The production of scintillating fibres is a delicate process. The diameter is regulated via the drawing speed of the fibre which is adjusted via an online measurement of the diameter [7]. The nominal fibre diameter is 250  $\mu\text{m}$  but the real diameter fluctuates due to the regulation process. However the fluctuations are small and the typical average fibre diameter is 250  $\mu\text{m}$  within 1  $\mu\text{m}$  [97].

As explained in chapter 5.2.3 short large fluctuations of the diameter<sup>5</sup> (see Fig. 6.8) can cause jumping fibres during the fibre mat winding and therefore they need to be cut out. The position of these bumps needs to be known for the winding. Dedicated fibre scanner machines were developed at different institutes to measure the diameter and to check the fibre for light leaks [65].

The diameter is measured with a laser micrometer in two rectangular directions (called x and y). An example of the diameter trend is shown in Fig. 6.9. The trend shows that the fibre is oval and that the orientation in the machine is not constant. In order to check the

<sup>4</sup>Effective January 2016, but successful tests were also performed with 30 cN.

<sup>5</sup>According to informations of the producer the bumps are caused by impurities of the base material [7]

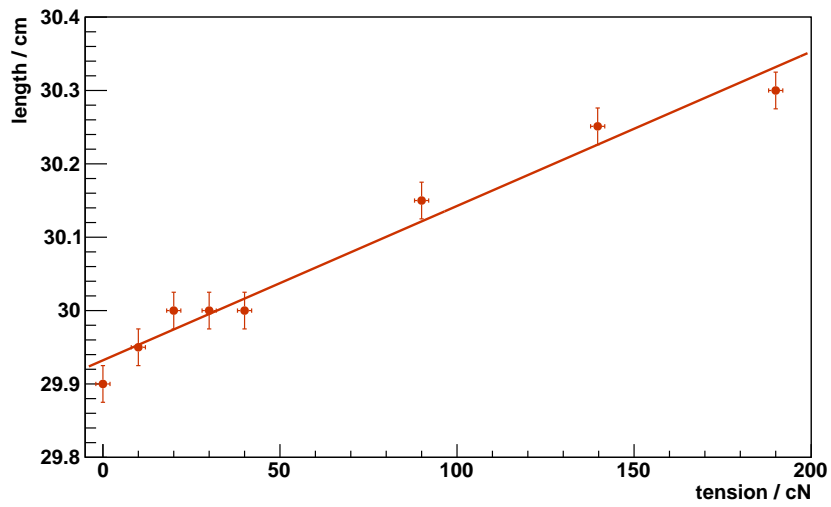


**Figure 6.6:** The extension of a scintillating fibre under different forces. The linear fit gives an relative extension of  $(7.0 \pm 0.5) 10^{-5}/\text{cN}$  which corresponds to an elastic modulus of  $(2.3 \pm 0.2) \text{ kN mm}^{-2}$ .

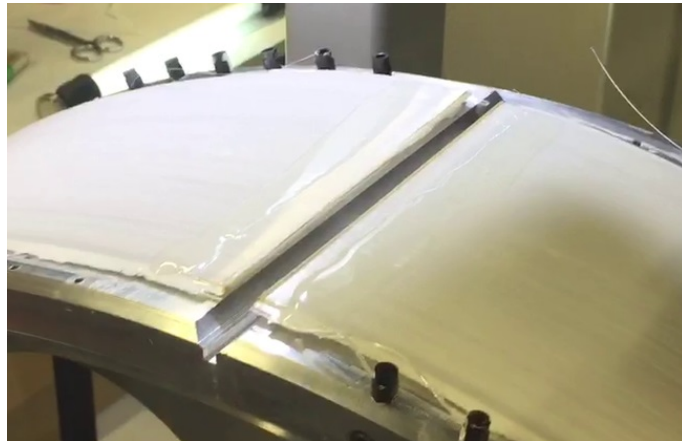


**Figure 6.7:** The contraction of a fibre mat right after the vertical cut.

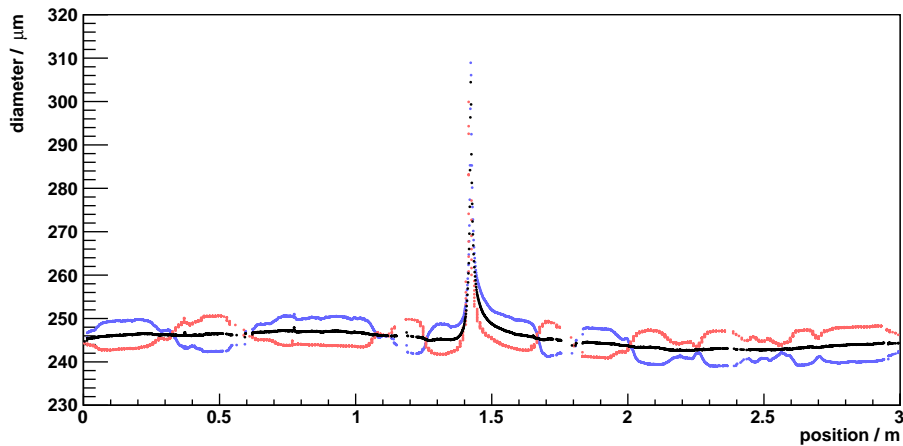


**Figure 6.8:** A diameter trend including a bump at the position of about 1.4 m. The red and blue points show the two perpendicular measurements, while the black points are the average of the two.

real evolution of the diameter the mean of the x- and y-value has to be considered. The evolution was checked for periodicity in a dedicated study but no regularity was found [98].

In order to determine the ovality, the x- and y-values are plotted in a two-dimensional histogram (see Fig. 6.10-left, the data was taken for the coverlay mat). It seems like the fibre has two preferred orientations, but the shape is caused by the projective measurement setup. A designated simulation with a randomly orientated oval fibre gives the result in Fig. 6.10-right. To judge the ovality, the larger and smaller diameter value are averaged independently (see Fig. 6.11). The average of the smaller values is  $244.2 \mu\text{m}$  and  $249.1 \mu\text{m}$  for the larger values. The ovality is not critical for the fibre mat production, it is small compared to the diameter fluctuations.

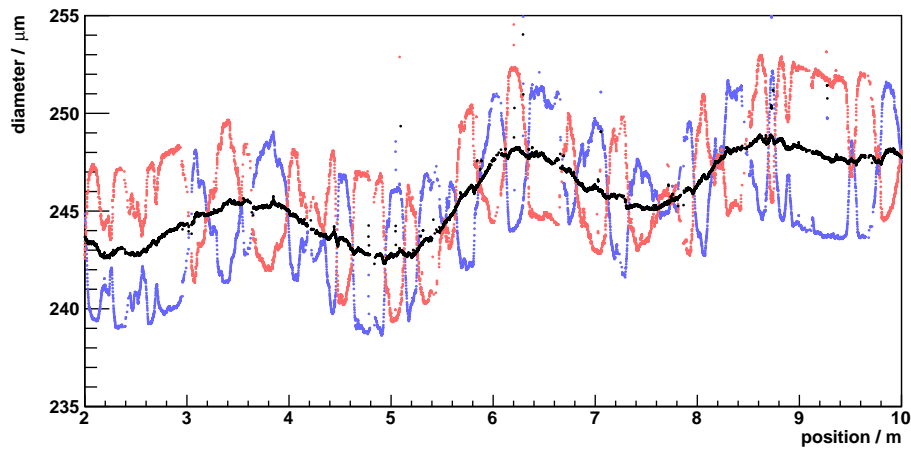


**Figure 6.9:** Fibre diameter trend. The red and blue points show the two perpendicular measurements, while the black points are the average of the two.

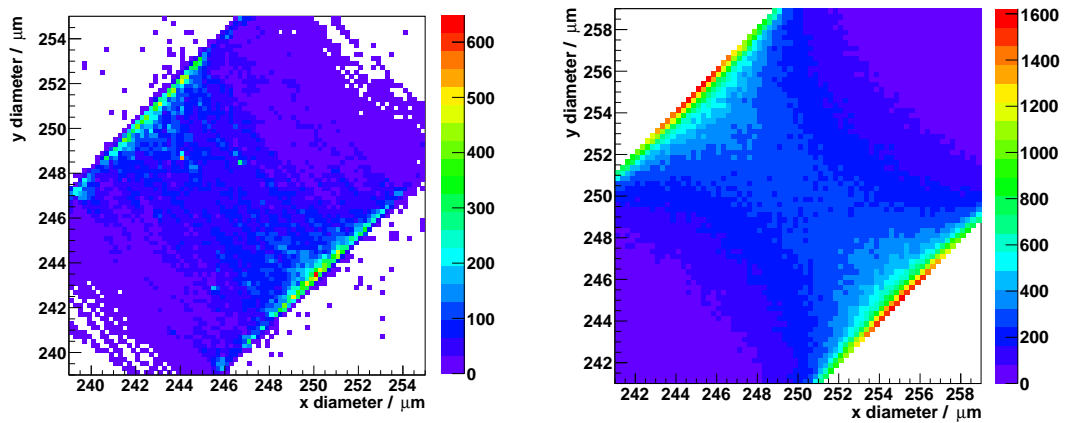


**Figure 6.10:** The distribution of the fibre diameter measured in two perpendicular directions. The left plot shows a measurement result. The right plot shows a simulated measurement of an oval fibre which is randomly orientated.



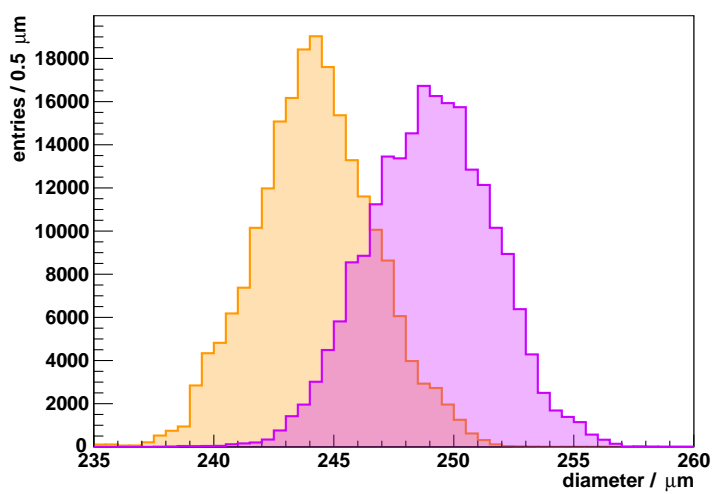


**Figure 6.11:** The distribution of the diameter of an analysed fibre. The diameter values of the perpendicular measurement are split in larger (purple) and smaller diameter (orange) at each position along the fibre. The average of the smaller values is  $244.2 \mu\text{m}$  and  $249.1 \mu\text{m}$  for the larger values.

## 6.3 Light guidance

As explained above the transmission in the fibre is affected by different factors. In addition to the absorption and scattering from the base material (polystyrene and wavelength shifter) the signal can be attenuated by impurities in the material and by reflection losses at the boundaries. To quantify these effects dedicated measurements and simulations were performed.

The attenuation of a fibre is typically determined exciting it at different positions and measuring the amount of light reaching one fibre end with a photo-detector. Cutting the fibre in different lengths and measuring the transmission (as needed for pure light guiding fibres) would be more difficult, less precise and would obviously not allow repetitive measurements of the same piece of fibre. To measure the attenuation along the fibre it is not needed to excite it with ionizing particles. An UV-LED does not trigger the scintillation but excites the wavelength shifter which is sufficient to determine the attenuation. The UV-light of a single LED does not excite the fibre as uniform across its cross section as minimizing particles, but simulations performed in [54] showed that no effect on the average attenuation is expected.

Measuring the attenuation with an SiPM or a photo-diode includes all the photons leaving the fibre. The attenuation is not the same for all the photons, it depends on their wavelength and their path along the fibre (the angle and the skewness), therefore this kind of measurement gives an effective attenuation. The wavelength spectrum and the angular distribution change with the distance to the excitation point, hence the average attenuation changes. The ratio of photons which are highly attenuated decreases and with it the average attenuation. To get comparable results, the LHCb SciFi group and the manufacturer agreed to state the effective attenuation fitting a single exponential curve to the intensities between 1 – 3 m distance to the photo-detector. This makes it possible to compare the values obtained in different labs.

To predict the performance of the fibres and the whole tracker in scenarios not achievable in a lab it is essential to perform simulations, see chapter 4.3.4. A single fibre simulation based on the GEANT4 toolkit [99] was developed in Dortmund [54]. To tune the parameters it is necessary to determine the actual (non-effective) attenuation for the photons with different wavelengths and angles. With this, the simulation can be used to compare different measurement setups.

The setup illustrated in Fig. 6.12 is used to determine the attenuation of a 12 m long scintillating fibre. A spectrometer<sup>6</sup> determines the amount of light as a function of its wavelength. The spectrometer is pre-calibrated by the manufacturer, but the calibration does nevertheless not effect the attenuation measurement. The fibre is excited by four UV-LEDs which are mounted in a white diffusing housing which was developed by the CERN SciFi group.

---

<sup>6</sup>The used spectrometer is a Hamamatsu C10083CA, based on a transmission grating made of quartz and a CCD image sensor (charge-coupled device) [100]

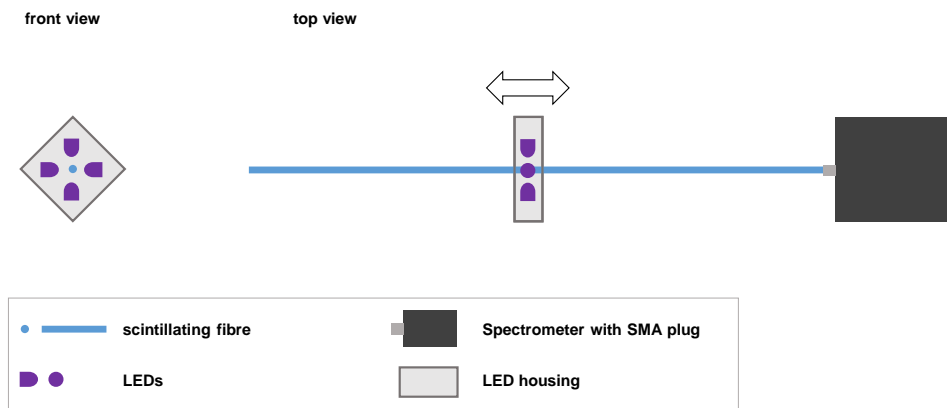


**Figure 6.12:** Sketch of the setup to measure a single fibre with a spectrometer. The fibre is excited by four UV-LEDs which are mounted in a white diffusing housing to ensure a proper excitation.

The light output is recorded for several positions along the fibre, in addition dark count measurements are performed. The intensity for every wavelength is fitted with an exponential decay to determine the attenuation, a single exponential curve is applied from 0.5 – 12 m. The attenuation per wavelength stays constant along the length, see Fig. 6.13. However the measured attenuation of the fibre is larger than of pure polystyrene plus wavelength-shifter, as shown in Fig. 6.14. The mismatch can have multiple reasons. The thin fibres are very fragile and performing measurements with them is a delicate process, small cracks can occur easily during handling. Moreover, the mechanical quality of the fibres might already be degraded coming from the manufacturer. Nevertheless this fibre is assumed to be mechanically fine. This illustrates that there are additional factors which reduce the transparency. Additional absorption and scattering can occur due to contaminations of the base material (water, air, dust) and photons can be lost due to imperfect boundaries between the core and the claddings. The latter will have a minor influence in this measurement because the numeric aperture of the spectrometer is rather small ( $n = 0.22$  [100]), covering an angular range of  $\pm 12.7^\circ$ . To better understand the influence of the boundary losses, dedicated measurements are performed.

In contrast to the real detector single fibre measurements are performed with the fibre in air. This enables total reflections at the outer boundary of the fibre. Due to the fact that the refractive index of air is very low compared to the fibre materials (core: 1.6, cladding 1: 1.5, cladding 2: 1.42, air: 1.0), a large increase in light yield at high angles is expected. A measurement setup was constructed [101–103] allowing the spectrometer to be rotated around the end of the scintillating fibre in a distance of 6 cm<sup>7</sup>, see Fig. 6.15. The spectrometer is mounted to a rotating arm, allowing to change the angle in the horizontal plane from  $-90$  to  $90^\circ$ . The angle in the vertical plane can be changed when mounting the

<sup>7</sup>The distance of 6 cm gave the best compromise of intensity and angle accuracy.

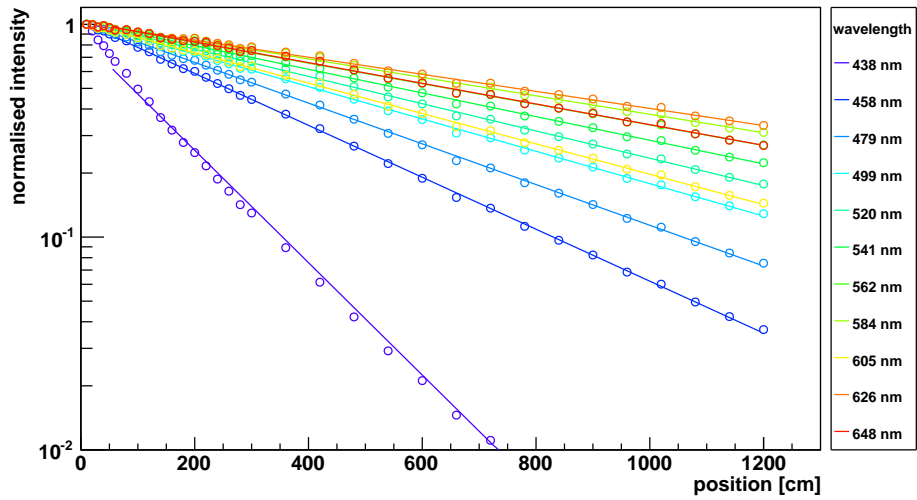


**Figure 6.13:** The normalised intensity as a function of the excitation position (distance to the spectrometer) for a 12 m long fibre for various wavelengths. The trend is fitted with an exponential curve to obtain the attenuation shown in Fig. 6.14.

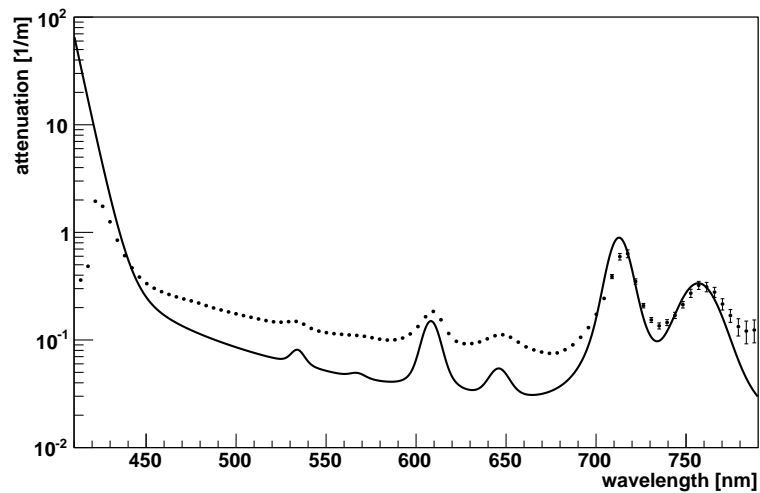


**Figure 6.14:** The spectral attenuation of a scintillating fibre. The points are the results of a measurement of a 12 m long fibre (see Fig. 6.13), the black line gives the attenuation for pure polystyrene plus wavelength-shifter from Fig. 6.5.

spectrometer at a different position along the arm (0 to 80°). It was found that the vertical angle typically gives systematic deviations in the data. This is caused by the imprecise positioning of the spectrometer in the dedicated mounting holes, therefore these data are mostly not used in the analysis.

The measurements are compared to the respective results of the single fibre simulation. Figure 6.16 shows the intensities for an excitation in a distance of 25 cm. In addition to the measured data, the simulated angular spectrum of photons reflected at the boundary core - cladding 1, cladding 1 - cladding 2 and cladding 2 - air are shown. The comparison reveals that photons entering the outer cladding are lost with a high probability although they enter in the correct angle to be totally reflected. Included in a fibre mat this would be the case anyhow (the refractive index of the glue is higher than the one of the claddings), but this study shows that it is also true for single fibre measurements in air. The tail to low angles of the photons which are reflected in the claddings is caused by photons leaving the fibre from a cladding. Their angle outside the fibre is lower than the one of the photons leaving the fibre from the core, although they are travelling with the same angle inside the core.

Figure 6.17 shows the same data but only for photons which are not reflected at the outer surface. The measured intensity for angles corresponding to the photons reflected between the claddings is systematically lower than the simulation results. This suggests that the probability for photons to be reflected at this boundary is smaller than 1. Simulation results with reduced reflection probabilities are shown in Fig. 6.18. The respective probabilities are  $2 \times 10^{-5}$  for core-cladding 1 reflections and  $6.3 \times 10^{-4}$  for cladding 1-cladding 2 reflections. However the measurement data at a single excitation point is not precise enough to determine these numbers reliably.

The reflection losses can be quantified measuring the attenuation (intensity drop along the fibre) as a function of the angle. The reason for this is that the travel length and the number of reflections scale different with the angle (see chapter 6.1.2), the increase in attenuation at higher angles is dominated by the reflection losses. Effective winter 2015/16 the simulation parameters are based on the measurement of one fibre. More measurements are planned to consolidate the numbers.

The attenuation measurement is performed in a similar manner as the intensity measurement, but now the angular intensity is determined for several excitation points along the fibre [105]. The parameters of the simulation are adapted in a way that they describe the data [106]. The attenuation due to reflection losses is negligibly small for the 0° measurement so that the attenuation of the base material can be adjusted with the help of this data point. The probability that photons are not reflected at the boundaries is then tuned to describe the larger attenuation at higher angles. For now the loss-probability is assumed to be the same for the core-cladding 1 and cladding 1-cladding 2 boundary. With more measurements available these parameters can be adjusted individually. Figure 6.19 shows the measurement results and two simulation results, one without and one including boundary losses. The parameters obtained with the help of this measurement are used in the following simulation studies. The additional attenuation due to impurities

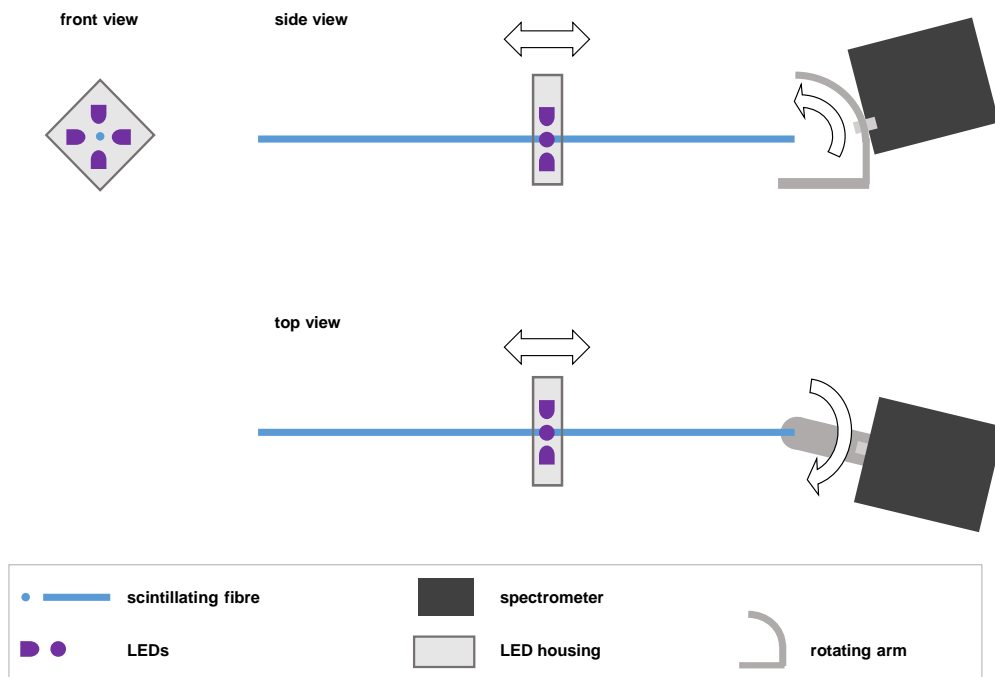


**Figure 6.15:** Sketch of the setup to measure the angular intensity of a single fibre with a spectrometer. The fibre is excited by four UV-LEDs which are mounted in a white diffusing housing to ensure a proper excitation. The spectrometer is mounted to an arm which can be rotated in the horizontal plane. The angle in the vertical direction can be changed by mounting the spectrometer to a different position along the arm. A photograph of the spectrometer mounted to the arm is shown in the appendix in Fig. A.4. (For the measurements concerning the reflections at the outer surface a single LED was used.)

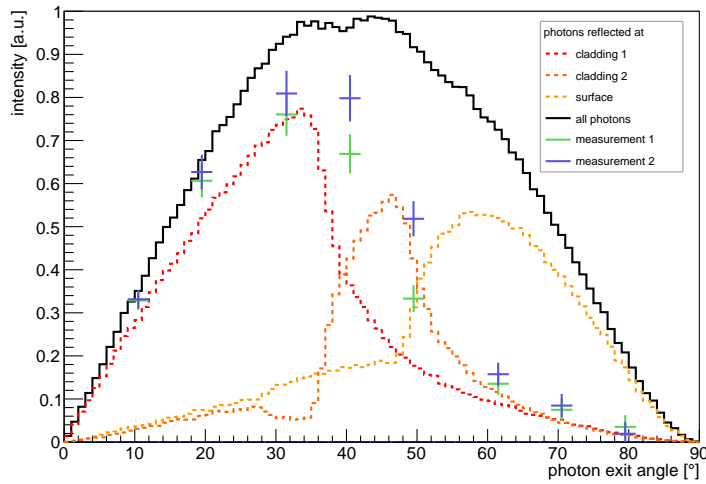


**Figure 6.16:** Angular intensity for photons leaving the fibre end. The different simulated curves represent different points of reflection of the photons. The trend of the measurement points indicates that photons which are reflected at the surface of the fibre are lost. Measured data from [104].

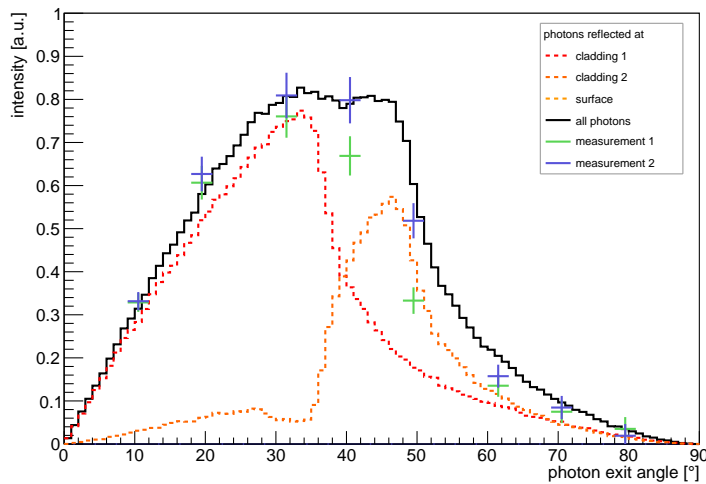


**Figure 6.17:** Simulated angular intensity for photons leaving the fibre end, where reflections at the surface of the fibre are forbidden. Measured data from [104].

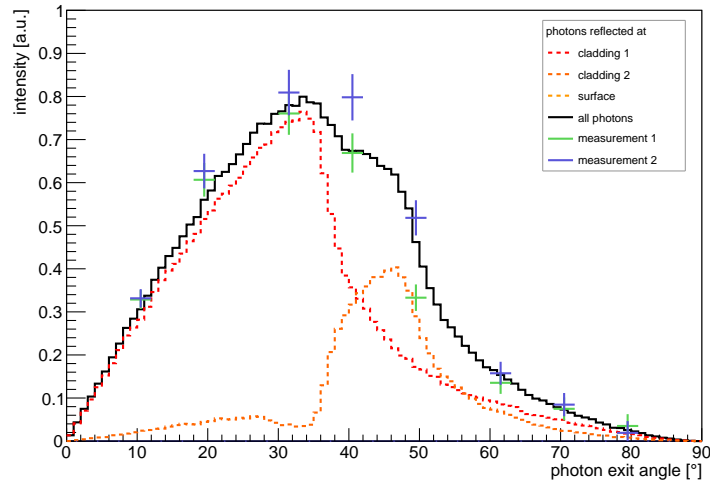


**Figure 6.18:** Simulated angular intensity for photons leaving the fibre end, including reflection losses for the boundary core - cladding 1 and cladding 1 - cladding 2. Measured data from [104].

is  $4.65 \times 10^{-2} \text{ m}^{-1}$  and the reflection loss probability is  $2 \times 10^{-5}$ , both are assumed to be constant with the wavelength at this point.

The track length and reflection losses for different photon exit angles are studied with the single fibre simulation (see also [107]). The contribution to the total attenuation as a function of the angle is shown in Fig. 6.20. The attenuation due to reflection losses accounts to about one third in between 30–40° with which angle the most photons are emitted.

At an angle corresponding to an exit angle of 35° the photons are not reflected at the first cladding but enter it to be reflected at the boundary between the two claddings. Corresponding to the thickness of the claddings and the refractive indices they travel about 10 % of their total path length in the first cladding (see Fig. 6.21). Due to the given angle the path length of the photons is longer than the direct distance between the excitation point and the end of the fibre, the ratio is shown in Fig. 6.22. The relative path length increases with the angle as expected (see chapter 6.1.2), but in addition an increase in the relative path length can be observed for excitation points close to the fibre end. Photons which leave the fibre end from the cladding have a small angle outside the fibre, although they have a larger one inside the core. These travelled a long path, but exit the fibre under small angles and can therefore influence the mean relative path length. This difference in path length changes the attenuation seen in a measurement with short fibres and needs to be taken into account. For a distance to the fibre end of 25 cm and an angular measurement at 0° the correction is 10 %.

The irradiated fibres examined in this thesis are much shorter than the ones used in the detector and do not allow for a measurement of the attenuation between 1–3 m (see chap-



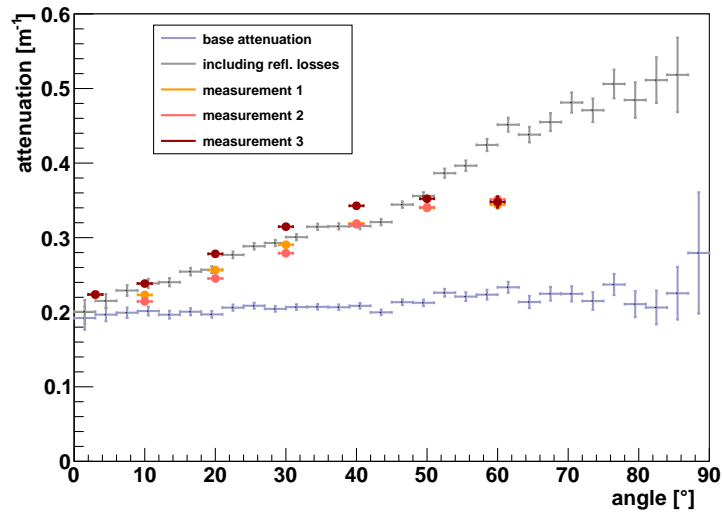


**Figure 6.19:** Angular attenuation in measurement and simulation as a function of the photon exit angle. The measured attenuation is the result of one single fibre. Simulation results are shown for a fibre without reflection losses and with a probability to loose the photon of  $2 \times 10^{-5}$  at the core-cladding 1 or cladding 1-cladding 2 boundary. Data from [107]

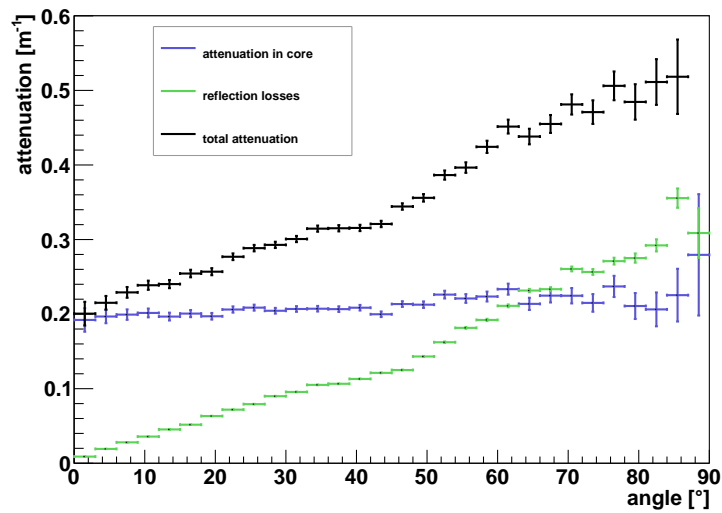


**Figure 6.20:** The simulated contributions to the attenuation as a function of the photon exit angle. The absorption and scattering in the material stays rather constant with the angle, while the attenuation due to boundary losses at the reflections increases with the angle. Data from [107].

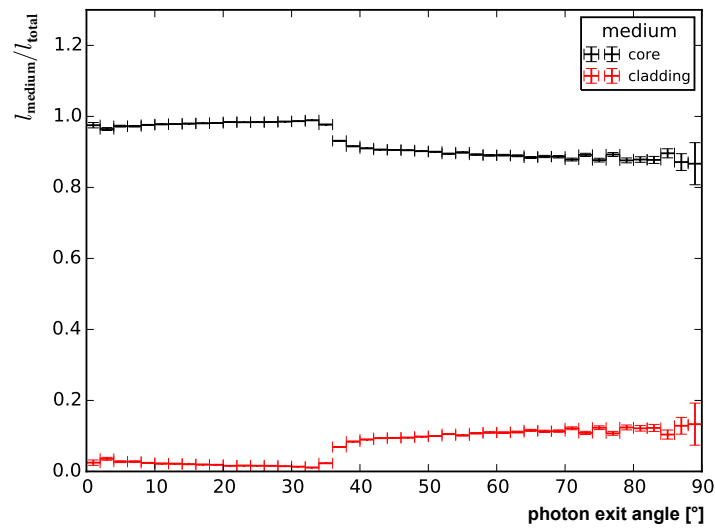


**Figure 6.21:** Simulated relative photon path lengths in core and cladding. [107], modified

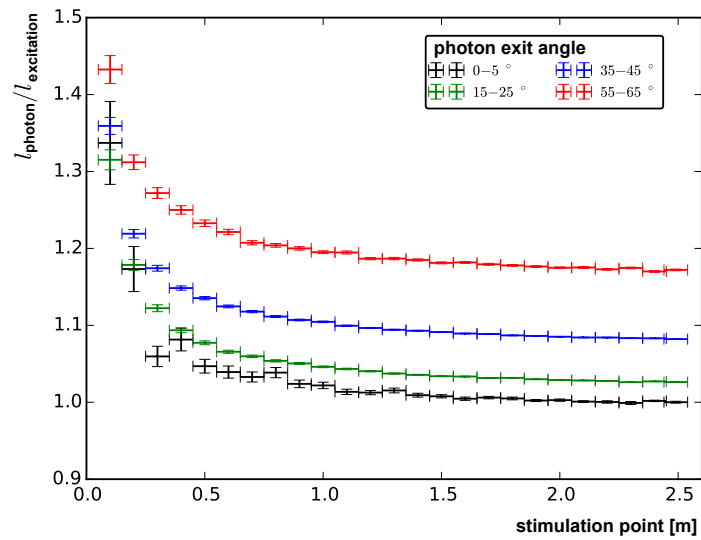


**Figure 6.22:** simulated photon path length divided by the excitation distance as a function of the stimulation point for different exit angles. [107], modified

ter 6.4). To ensure that they give comparable results, the attenuation length was determined for different angles for exciting positions from 0.2–1 m and 1–3 m with simulation data, see Fig. 6.23. The comparison at 0–5° is limited by the small sample but the other angles show a good agreement.

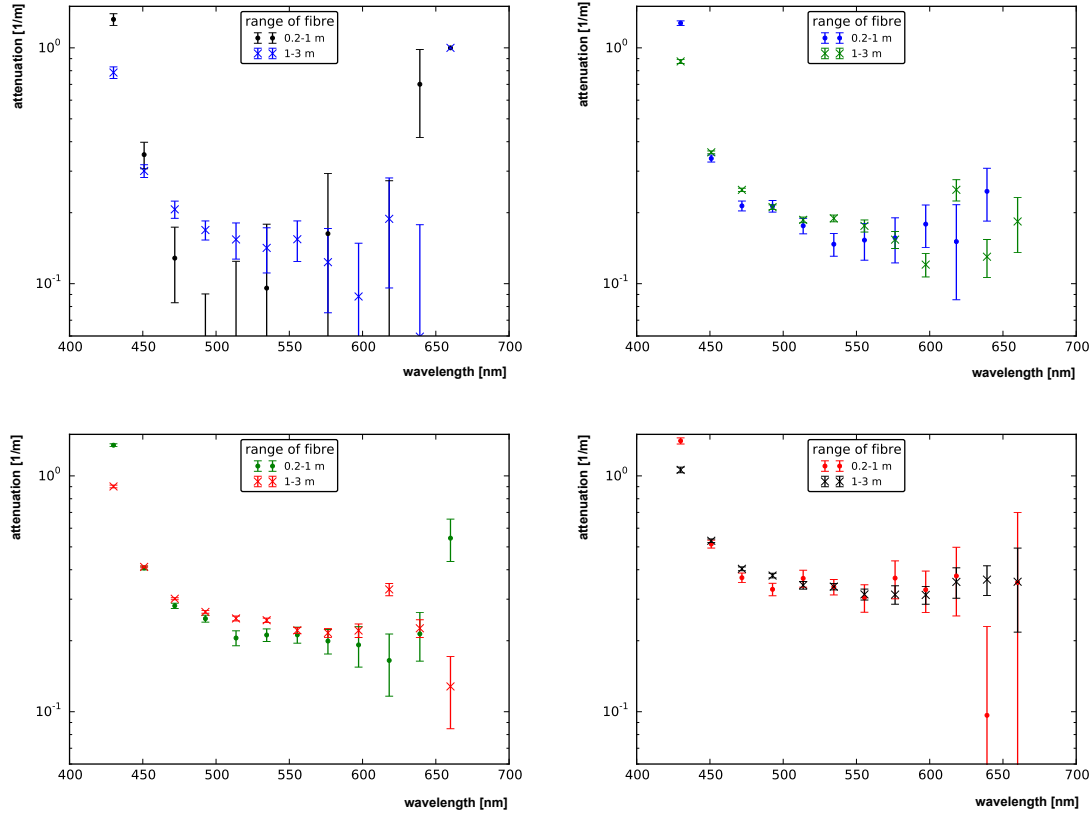


**Figure 6.23:** Simulated attenuation as a function of the wavelength split up into two fibre sections. Analysed angles (top down): 0 – 5° left, 15 – 25° right; 35 – 45° left, 55 – 65° right. [107], modified

The wavelength dependent measurement with a spectrometer helps to determine the contribution of the reflection losses. The attenuation caused by them is constant with wavelength (to current knowledge), in contrast to the attenuation in the base material which is dominated by the re-absorption of the wavelength shifter which therefore decreases rapidly to longer wavelengths. The attenuations for different parameter combinations are shown in Fig. 6.24 for all photons (0–90°) and for photons leaving the fibre with an angle of about 60°. For the sum of all photons the reflection losses account for at least one third of the attenuation above 500 nm.

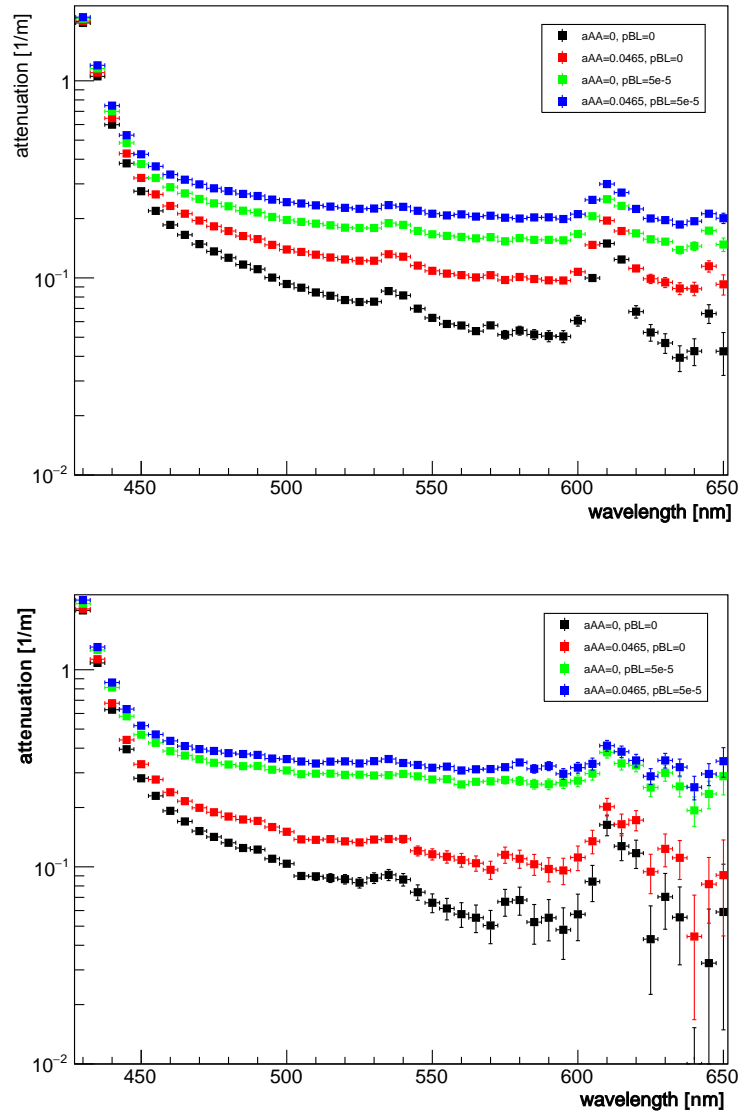


**Figure 6.24:** Simulated wavelength dependent attenuations for different parameter combinations. The black line shows the attenuation for pure polystyrene plus wavelength-shifter, the red line adds attenuation in the base material (aAA), the green line adds reflection losses instead (pBL). The blue line shows the attenuation considering all the attenuation factors. Top: for all photons (exit angles  $0-90^\circ$ ), bottom: for the exit angles  $55-65^\circ$ . [107], modified

## 6.4 Radiation damage

The amount of light reaching the SiPMs is a crucial parameter for the performance of the SciFi Tracker. The most tracks pass through the central region of the detector, therefore it is the most important part of the detector but also the one which suffers the most from radiation damage of the scintillating fibres. Several irradiation campaigns were performed in the LHCb SciFi group to determine the increase in attenuation for different doses. The next two sections describe irradiation campaigns performed in the course of this thesis. Following that the results are compared to others to give the current knowledge.

### 6.4.1 Proton beam irradiation

Several pieces of fibres were irradiated at the tandem accelerator of the Maier-Leibnitz-Laboratorium at Forschungszentrum Garching near Munich. The first qualitative results were presented in the Letter of Intent for the LHCb Upgrade [6], whereas the detailed analysis is presented here.

Four 50 cm long fibres are arranged parallel on a support made from foam. At one end they are bundled and glued in a glass pipette (a photograph is shown in the appendix, see Fig. A.1). Four groups of these fibres were irradiated with 21 MeV protons to different dose levels, only the ones with the highest dose of 100 kGy are analysed here, due to their unique high dose. The dose was reached after an irradiation time of 2.5 h. The irradiation is limited to the central region of 5 cm length. The spread across the fibres was achieved by the controlled deflection of the beam, the spread along the fibres with the help of a linear slide, moving the module. The dimensions were additionally constrained by an absorber plate (see Fig. A.2 and A.3). The dose was determined via the measurement of the beam current before and after the irradiation with the help of Faraday cups, it could not be monitored in between. The uncertainty on the dose is estimated to be 20 %.

To analyse the attenuation, the fibres are excited by an UV-LED and read out with a spectrometer under different angles, see Fig. 6.25. The read-out is the same described before for single fibres. Due to the fact that the fibres are glued to a support, they can not be excited with the 4-LED array. A single LED is moved perpendicular to the fibres in small steps with a measurement taken at each step. Only the measurement with the highest intensity is used for the analysis, assuming that this is the one where the LED is centred above the fibres. The fibres are analysed from 25–49 cm distance to the fibre read-out end for the exit angles  $0^\circ$  and  $30^\circ$ . The uncertainties for the intensity are calculated as combination of statistical and systematic uncertainties. The latter ones take into account the fact that the peak value of the perpendicular scan is searched for in steps. The error deriving from the fact that the excitation of the fibre is not uniformly efficient along the length is not taken into account, because it is not possible to define a reliable number for this. The uncertainties are explained in more detail in the next section.

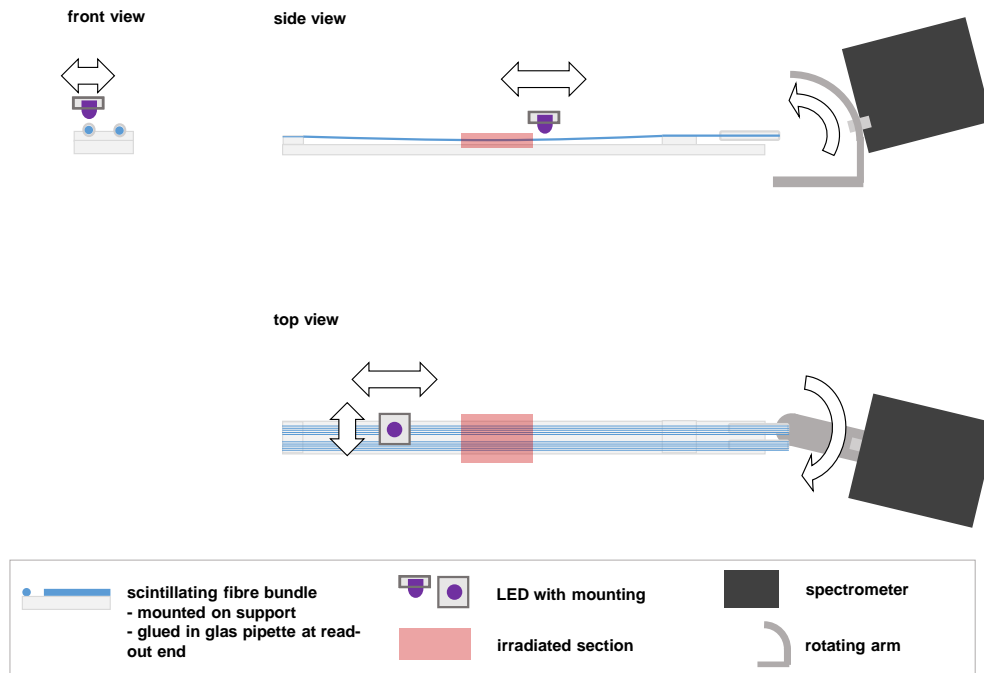


**Figure 6.25:** Sketch of the setup to measure the angular intensity of the fibres irradiated in Garching. The spectrometer is mounted to an arm which can be rotated in the horizontal plane. The angle in the vertical direction can be changed by mounting the spectrometer to a different position along the arm. A photograph of the spectrometer mounted to the arm is shown in the appendix in Fig. A.4. The exciting UV-LED moves across and along the fibre. It is mounted to an xy-table with two perpendicular linear slides. The slides are controlled from the same program which reads the data from the spectrometer.

The analysed part of the fibres is split in three sections with the irradiated part in the middle. Performing two single exponential fits to the un-irradiated parts reveals that they do not give the same attenuation, it is larger close to the photo-detector. Comparing the fit results to the expected attenuation for a non-irradiated fibre, shows that the attenuation is too large in the first part and too low in the second part (the intensity is even constant). Multiple effects might cause this, as discussed as following. It is known that reflections can occur at the end of a fibre or at cracks which increase the light yield close to the end and therefore lead to a smaller effective attenuation. Test measurements with a blackened end were performed but did not show obvious improvements. As studied with the simulation before, the average path length is longer close to the photo-detector, this is compensated by adding an appropriate factor to the attenuation for each of the three sections. This is only a minor correction and does not give equal fit results yet.

The fibre is glued to the support in front and behind the analysed section, hanging in the air with a certain radius in between. This might cause a difference in excitation due to the profile of the UV-LED. To compensate for this, the intensity along the fibre is modified with a 4th order polynomial function, chosen in a way that the attenuations resulting from the fits give the same value. The same function is used for all wavelengths and for both angles. To ensure that the method and the parameters used are appropriate more studies could be carried out (see below). The resulting intensity trends for different wavelengths are shown in Fig. 6.26 & 6.27 respectively. The exponential functions used are independent for the un-irradiated and the irradiated part and use the same attenuation parameter for the two un-irradiated sections. The method of intensity correction is not studied further because the attenuation in the irradiated part is about a factor 30 larger, so that the influence of the attenuation in the un-irradiated fibre sections is of minor influence.

The resulting attenuations for  $0^\circ$  and  $30^\circ$  are shown in Fig. 6.28. As expected the relative uncertainties for the attenuation in the un-irradiated part is quite large, as a result of the short fibre. However they are small enough to see the larger attenuation for photons exiting the fibre under an angle of  $30^\circ$ . The attenuation in the irradiated section is way larger and decreases exponentially to longer wavelength. An effect of the angle on the attenuation can not clearly be identified. The ratio of number of reflections at the boundaries between the two angular measurements is a factor of 1–1.8 orders of magnitude, assuming an average angle of  $3^\circ$  and  $0.5^\circ$  for photons detected by the spectrometer for the  $0^\circ$  measurement respectively. It can be concluded that the quality of the surface and therefore the reflection probability is not harmed by the irradiation. The results on the additional attenuation are combined with others in Section 6.4.4, the effect on the light yield is discussed in Section 6.4.5.

## 6.4.2 In-situ irradiation

When irradiating fibres at beam lines, it is simple to reach high doses on short time scales. However the possible influence of the dose rate on the damage requires special tests

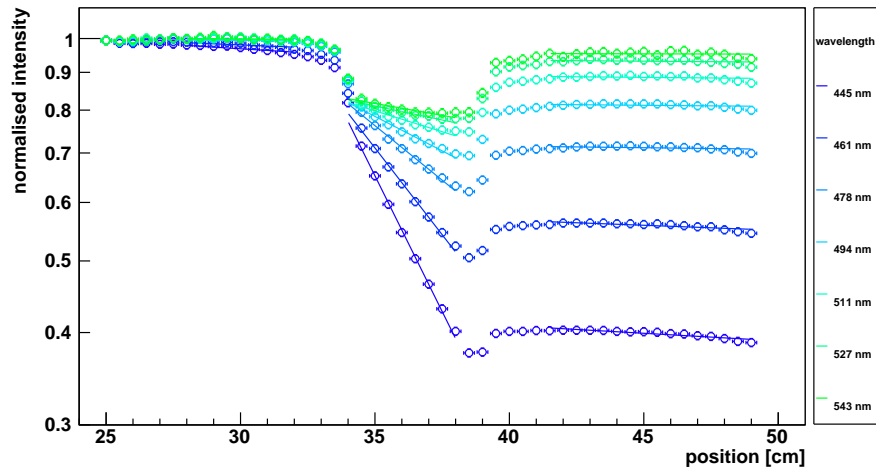


**Figure 6.26:** The intensity trend for  $0^\circ$  for the fibres irradiated in Garching. The fibres were irradiated in the middle only. The fit functions are explained in the text.

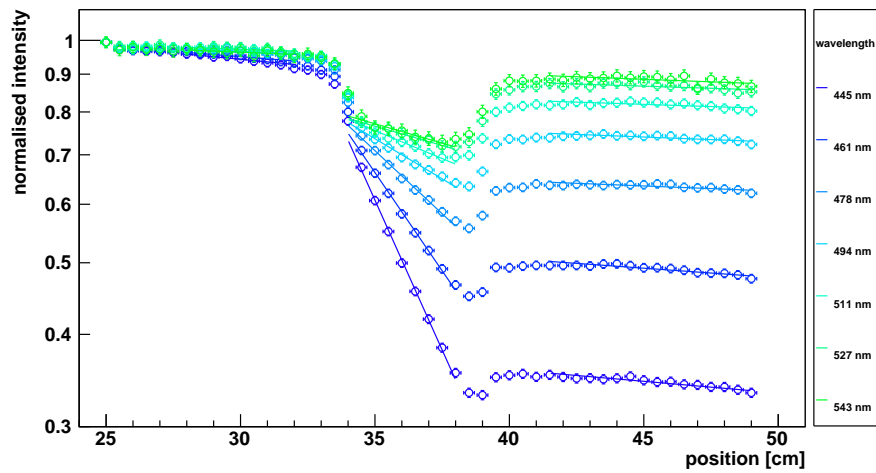


**Figure 6.27:** The intensity trend for  $30^\circ$  for the fibres irradiated in Garching. The fibres were irradiated in the middle only. The fit functions are explained in the text.



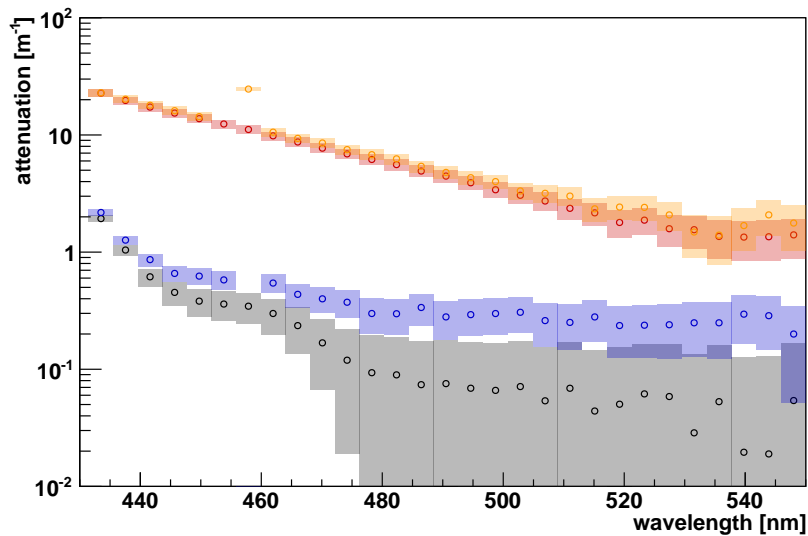


**Figure 6.28:** The attenuation of the fibres irradiated in Garching. The black and the blue points show the attenuation for the un-irradiated sections of the fibre for  $0^\circ$  and  $30^\circ$  respectively. The red and orange points show the respective attenuation for the irradiated section. The uncertainty of the fit results is shown as coloured areas.

with low dose rates. With these it is not possible to reach high doses (lack of time), the combination of both methods is needed to obtain reliable results.

Two low dose rate irradiations were performed in the course of this thesis. A few fibres glued to a support were installed parallel to the beam-line in the LHC tunnel upstream of the LHCb detector. During 2012 they received a homogeneous dose of about 3 kGy. These fibres were analysed by the CERN SciFi group, the results are included in the next section.

Parallel to that fibres glued to a support (called modules from now on) were positioned in the LHCb cavern. The three modules were installed on the shielding wall to the LHC tunnel, close to the VELO. An additional module was kept in the office as reference. The positions are listed in Fig. 6.29, a photograph is shown in Fig. A.6. The distance in  $z$  (along the beam-pipe) from the interaction point is about the same as for the TT.

A measurement of all the modules before the installation was planned but could not be realised due to wrong equipment on site<sup>8</sup>. The modules were installed in the first technical stop (TS1) 2012 and stayed in the cavern till the end of the year. The attenuation length was measured in TS2, TS3 and TS4 (christmas shutdown) with the help of a strontium source and an SiPM-module. The final dose which was applied to the modules is shown in Fig. 6.30, whereas it is 27 % and 65 % for TS2 and TS3 respectively. The dose is

<sup>8</sup>It was planned to excite the fibres with a strontium source, but the activity was too low to be used with the SiPM-module available. A measurement was performed with an UV-LED but the uncertainties were too high to be used.

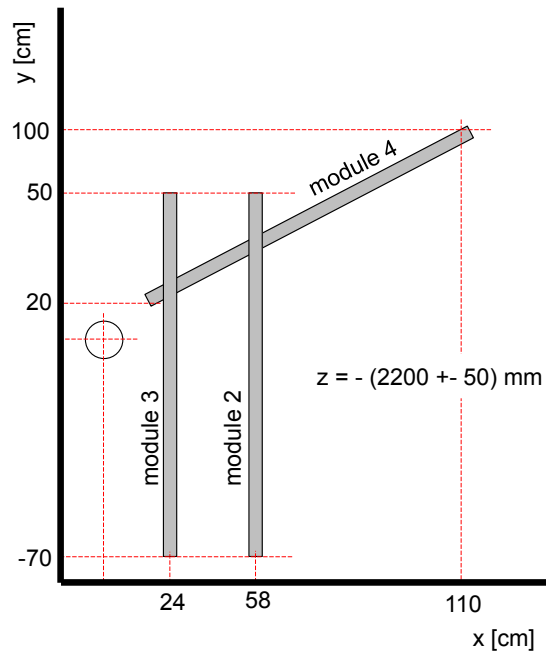


**Figure 6.29:** The position of the fibre modules installed in situ, at the shielding wall to the tunnel, close to the VELO. The positions are given with respect to the interaction point. A photograph of the installation is shown in Fig. A.6.

obtained from simulations of the LHCb group, the stated uncertainty is a factor of two of the dose [108]. The dose profile decreases quickly with the distance to the beam-pipe, creating a non-uniform dose distribution along the modules. This is a challenge for the analyse of the radiation damage.

The modules are measured with a strontium source ( $^{90}\text{Sr}$ , details about the source are listed in the appendix A.1) and an SiPM-module in the Technical Stops. The Hamamatsu MPPC C11208-01 houses a single channel SiPM with electronics and is read-out by a PC via USB. To place the source above the fibres, a positioning tool is used. This bar has to be aligned to the fibres once by eye, after that the source can be placed at the designated positions by pushing it to the bar. A sketch of the setup is shown in Fig. 6.31, a photograph of the source on the positioning bar in Fig. 6.32 and a photograph of the whole setup in Fig. A.7. The benefit of the single alignment per attenuation measurement is the reduced time needed (and therefore the working safety), the disadvantage is that the attenuation can be systematically lowered or increased by a rotation of the bar with respect to the fibres.

Two fibre packages with ten fibres each are glued to each module. One is completely covered with glue, the other one only at selective positions. Both packages where read out from either side so that four measurements are performed for every module. The resulting intensities for all modules in TS2-4 are shown in Fig. 6.33. The measured attenuation is not expected to be constant along the length of the fibres. The change of the wavelength spectrum and the angular distribution result in a systematic trend. More important the

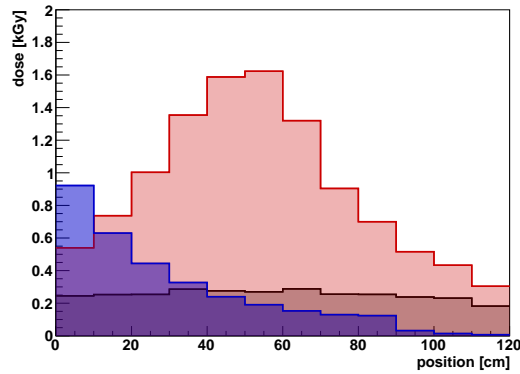


**Figure 6.30:** The final dose for the fibres irradiated in situ, module 2 is shown in black, module 3 in red and module 4 in blue. Data obtained from [108].

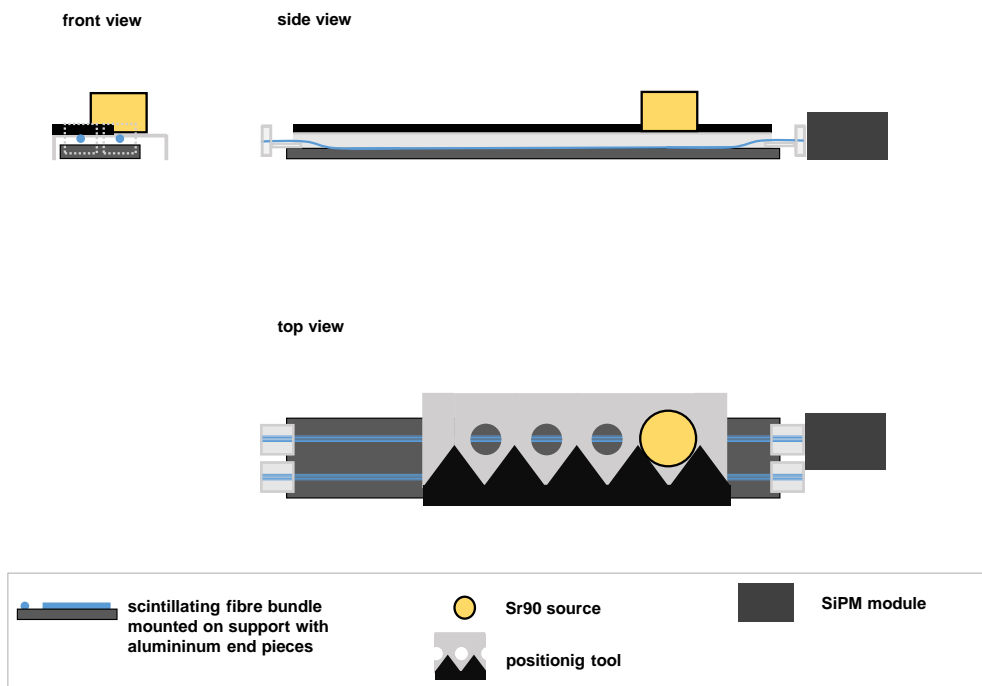


**Figure 6.31:** Sketch of the setup to measure the attenuation of the fibres irradiated in situ. A strontium source excites the fibres, it is placed on top of the the module with the help of a positioning bar. The fibres are read out by a SiPMs-module.

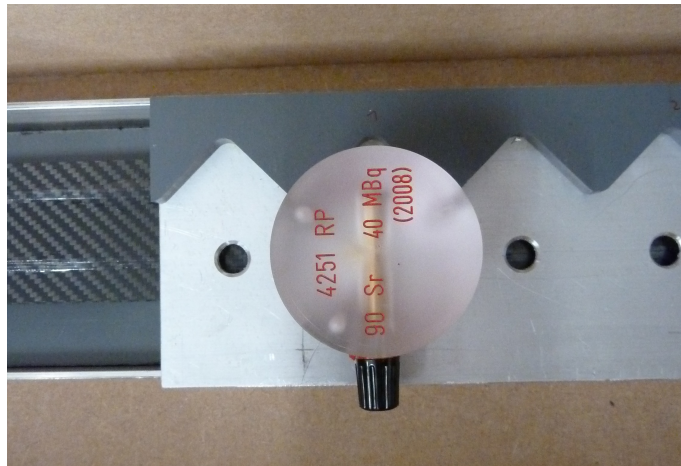


**Figure 6.32:**  $^{90}\text{Sr}$  source on the positioning bar. The fibres are aligned under the bar by positioning them underneath the holes.

dose and with it the expected radiation damage strongly dependent on the position along the module. Nevertheless the data for the measurements during the Technical Stops is described with a single exponential function. The systematic uncertainties do not allow for an improved analysis. The resulting attenuations are shown in Fig. 6.34. Although the four measurements of each module show a large spread (it is neither assumed nor observed that the glue influences the damage for the given precision), a clear increase of the attenuation for module 3 and module 4 can be seen.

In the course of the development of the single fibre GEANT4 simulation in the Dortmund group, the data obtained for module 3 with the SiPM measurements was used to test the parameters. This is described in detail in the corresponding thesis [54]. The setup was rebuilt in the simulation (fibre length, dose profile and photo-detector) and the analysis (single exponential fit) was performed in the same way as for the measurement data. The measurement results were compared to the result of two different radiation damage models. Both models assume a linear increase of the additional attenuation with dose. The model predicting a larger damage matched well the results of the in situ fibres within the uncertainties, whereas the studies performed at higher doses and dose rates by the LHCb SciFi group were better described by the second model.

With the help of the gained knowledge about scintillating fibres from measurements and simulations and an advanced setup it is now possible to improve the results. The measurement setup is equivalent to the one used for the proton-irradiated fibres, except for the fact that the holder for the fibre end is adapted for the aluminium end pieces, see Fig. 6.35. A photograph of a fibre bundle cross section in the aluminium end piece is shown in the appendix, see Fig. A.5. The attenuation of all four modules is measured from both fibre ends, each for the photon exit angles from  $-60^\circ$  to  $+60^\circ$  in  $20^\circ$  steps in the horizontal plane. Only the fibres completely covered with glue are used for the new analysis.

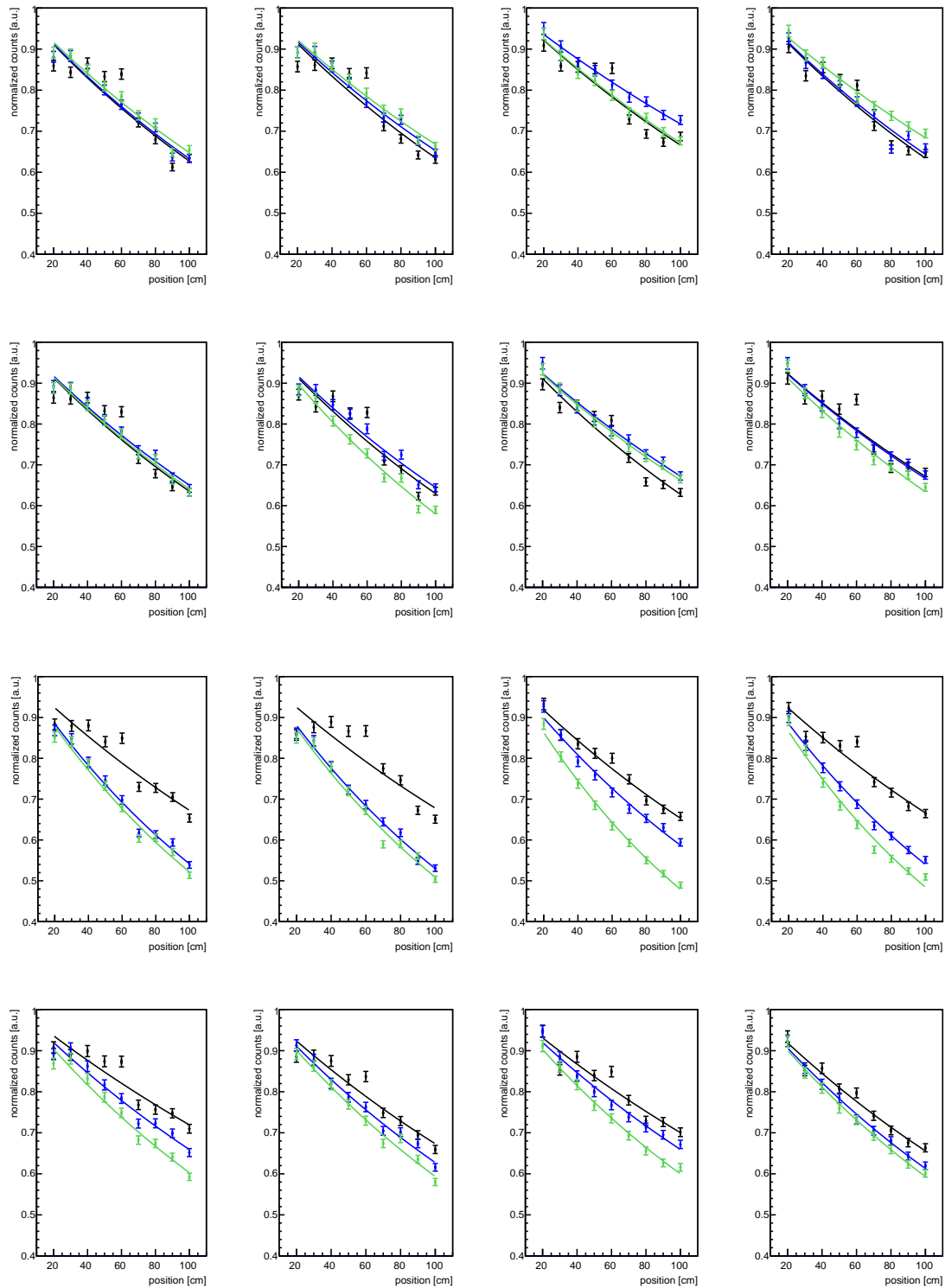


**Figure 6.33:** The intensity trends of in situ irradiated fibres measured with an SiPM. The four rows correspond to the four different modules 1-4. The columns show the different fibre bundles and measurement directions. The colour of the data and the of the trends represent the results for the measurements in Technical Step 2 (black), 3 (blue) and 4 (green).

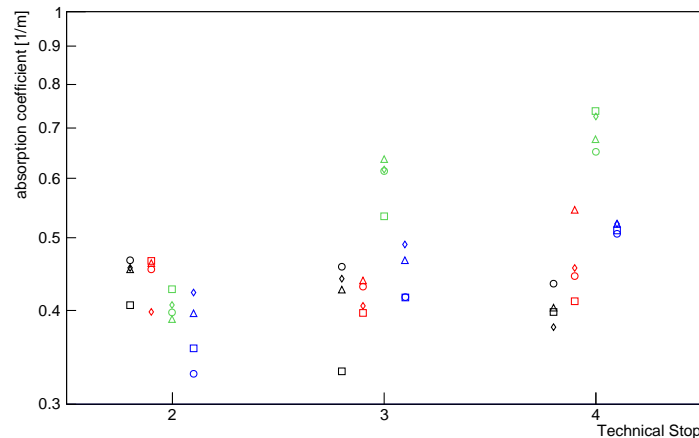


**Figure 6.34:** The attenuation for module 1-4 (left to right or black, red, green, blue) measured at the designated Technical Stop (TS) with the help of an SiPM. The four measurements for each module at each TS correspond to the two fibre bundles and the two directions. The corresponding dose since TS1 (installation) is 27 % (TS2), 65 % (TS3) and 100 % (TS4) of the final dose shown in Fig. 6.30.

Exemplary the intensity trend for module 3 under an angle of  $0^\circ$  is shown in Fig. 6.36(top). The intensity does not drop evenly, it even rises in between some measurement points. This can not be explained by the non-uniform dose but is a result of different excitation strengths. One influence is the fact that the UV-LED is not always perfectly centred on top of the fibres, it is moved in steps of 1 mm perpendicular to the fibre axis. The maximum drop of intensity caused by this is 2.5 %, the average systematic uncertainty is assumed to be 1.25 %. The statistic uncertainties are only relevant for low intensities which occur at low and large wavelengths and under large angles. In this case the non-even drop is mainly caused by a different level of excitation caused by the glue on top of the fibres. This can be corrected by the measurement of the intensity trend in the other direction (called backward direction).

To correct the intensities with the help of the backwards measurement, it is assumed that the attenuation is the same in both directions<sup>9</sup>. The intensities can only be corrected relative to each other (which is fine when determining the attenuation), arbitrary the first data point of the forward measurement is chosen to be of correct intensity. Successively the other intensities are corrected, calculated as a function of the previous offset and the intensity drops measured in both directions. The variation of the excitation strength is the same for all wavelengths and angles, it is just a function of the position along the fibres. The correction factor is therefore averaged over the central wavelength range with high intensities. Also the correction is just calculated for the  $0^\circ$  measurement and applied to the

<sup>9</sup>The effect of the longer path length for short distances to the photo detector is not taken into account, the effect is small compared to the corrections applied.

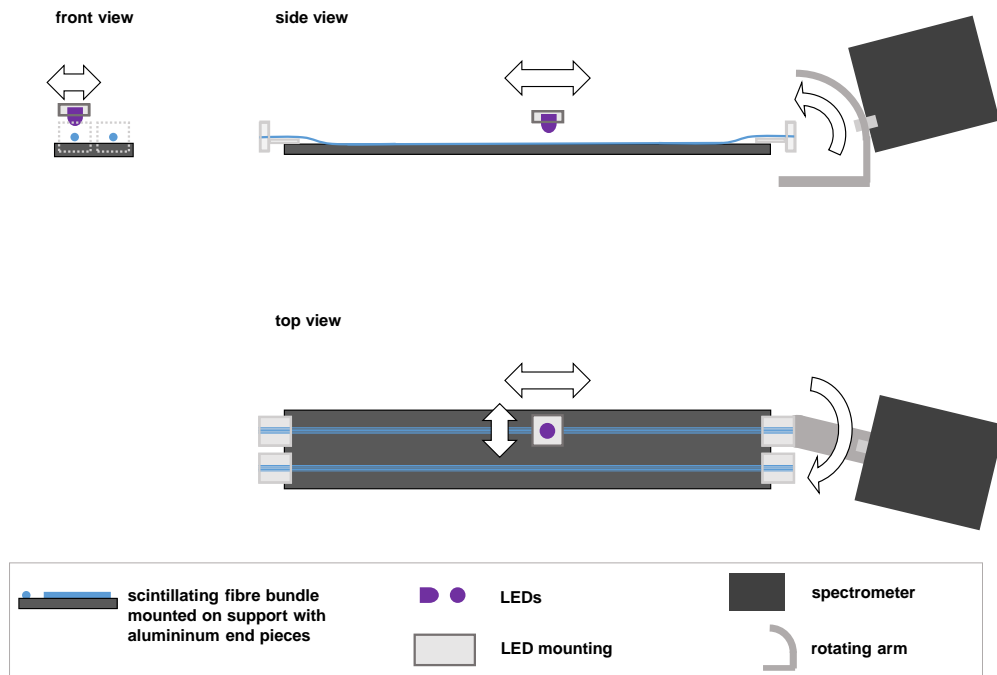


**Figure 6.35:** Sketch of the setup to measure the angular intensity of the fibres irradiated in situ. The spectrometer is mounted to an arm which can be rotated in the horizontal plane. The angle in the vertical direction can be changed by mounting the spectrometer to a different position along the arm. The exciting UV-LED moves across and along the fibre. It is mounted to an xy-table with two perpendicular linear slides. The slides are controlled from the same program which reads the data from the spectrometer.

other angles. The intensity trend for module 3 - 0° in forward and backward direction and the corrected trend are shown in Fig. 6.36, for all modules and angles see Fig. A.8-A.11.

The uncertainties of single data points of the resulting trends are low enough that a description with a simple single exponential curve would not be satisfactory for the irradiated modules. Instead the knowledge about the dose profile is used to define a more sophisticated function. At least for the relevant dose range, it can be assumed that the additionally induced attenuation increases linear with dose. The new function is built from sections of exponential functions with the respective attenuation, the intensity of each section is chosen in a way that the trend is continuous. The intensity  $I$  as a function of the position  $x$  is given by:

$$I(x) = \sum_{n=0}^N I_n e^{-(a_0 + D_n a_{rD})x}$$

with

$$I_n = \begin{cases} I_0 & \text{for } n = 0 \\ I_{n-1} e^{-(a_0 + D_{n-1} a_{rD})\Delta x} & \text{for } x_n < x < x_{n+1} \\ 0 & \text{else} \end{cases}$$

where  $n$  is the respective fibre section from  $x_n$  to  $x_{n+1}$  with the width  $\Delta x$ , the corresponding dose  $D_n$  and the intensity at the start of the section  $I_n = I(x_n)$ . The attenuation before irradiation  $a_0$  is obtained from the analysis of the un-irradiated module 1. The parameters obtained from the fit are the overall constant  $I_0$  and the additional attenuation per dose  $a_{rD}$ .

The resulting functions are exemplarily shown for the 0° measurement of module 1 and module 3 in Fig. 6.37. The measurement data with the functions for all modules and angles are shown in Fig. A.12. The chosen fit functions describe the data well, the trend is well reproduced. However one large uncertainty can not be compensated, the systematic misalignment of the spectrometer to the fibre end. This uncertainty is driven by the treatment of the fibre ends, not the adjustment of the spectrometer holder and is different from module to module.

The parameter extracted from the fit is the additional attenuation per dose. The absolute attenuation can not be determined like this for a module because it changes along the fibres. The resulting values are corrected for the average path length for the respective angle and shown in Fig. 6.38. The uncertainties for angles larger than 0° are not shown here (but in the appendix in Fig. A.13), the calculated values would just represent the statistical uncertainties and the systematic uncertainties caused by the alignment of the LED. The real uncertainties are driven by the angular offset, they are represented the best by the offset of the respective results under the same angle (which should be equal). The uncertainties are large for larger angles (and in general for module 2 & 4) caused by the fact that the relative expected difference in the attenuations due to the irradiation is small. The values for module 3 are the most reliable ones because the applied dose is the largest. It falls exponentially with increasing wavelength as expected. The additional attenuation per dose is about a factor three larger compared to the proton irradiation. No conclusion on the damage at larger angles can be made within the achieved accuracy. The values obtained for



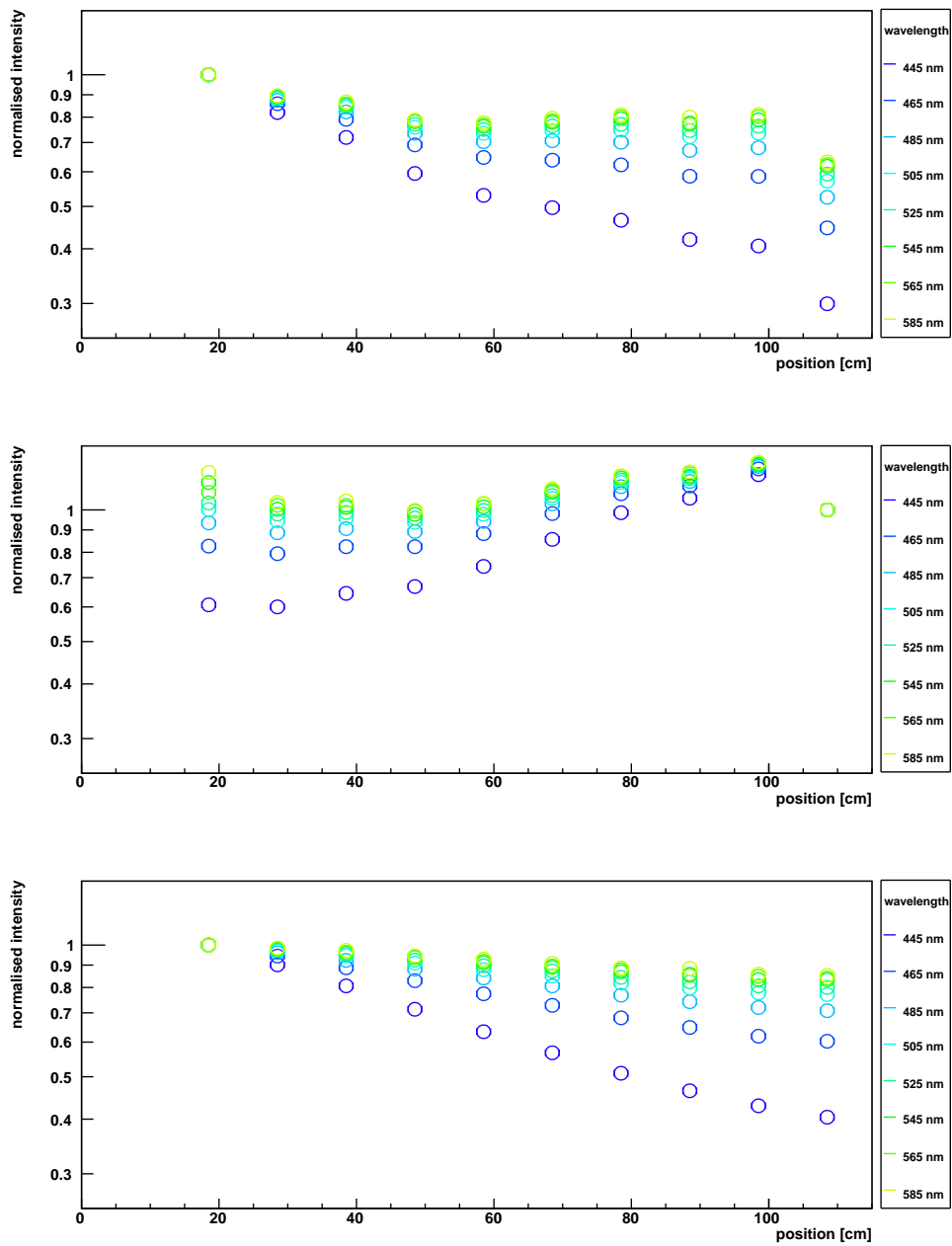


**Figure 6.36:** The correction of the intensities for module 3, angle  $0^\circ$ . The uppermost plot shows the measurement in forward direction, the middle one in backward direction. The lowest plot shows the corrected intensities for the forward direction with the help of the measurement in backward direction. The correction trends for all modules and angles are shown in the appendix, Fig. A.8-A.11.

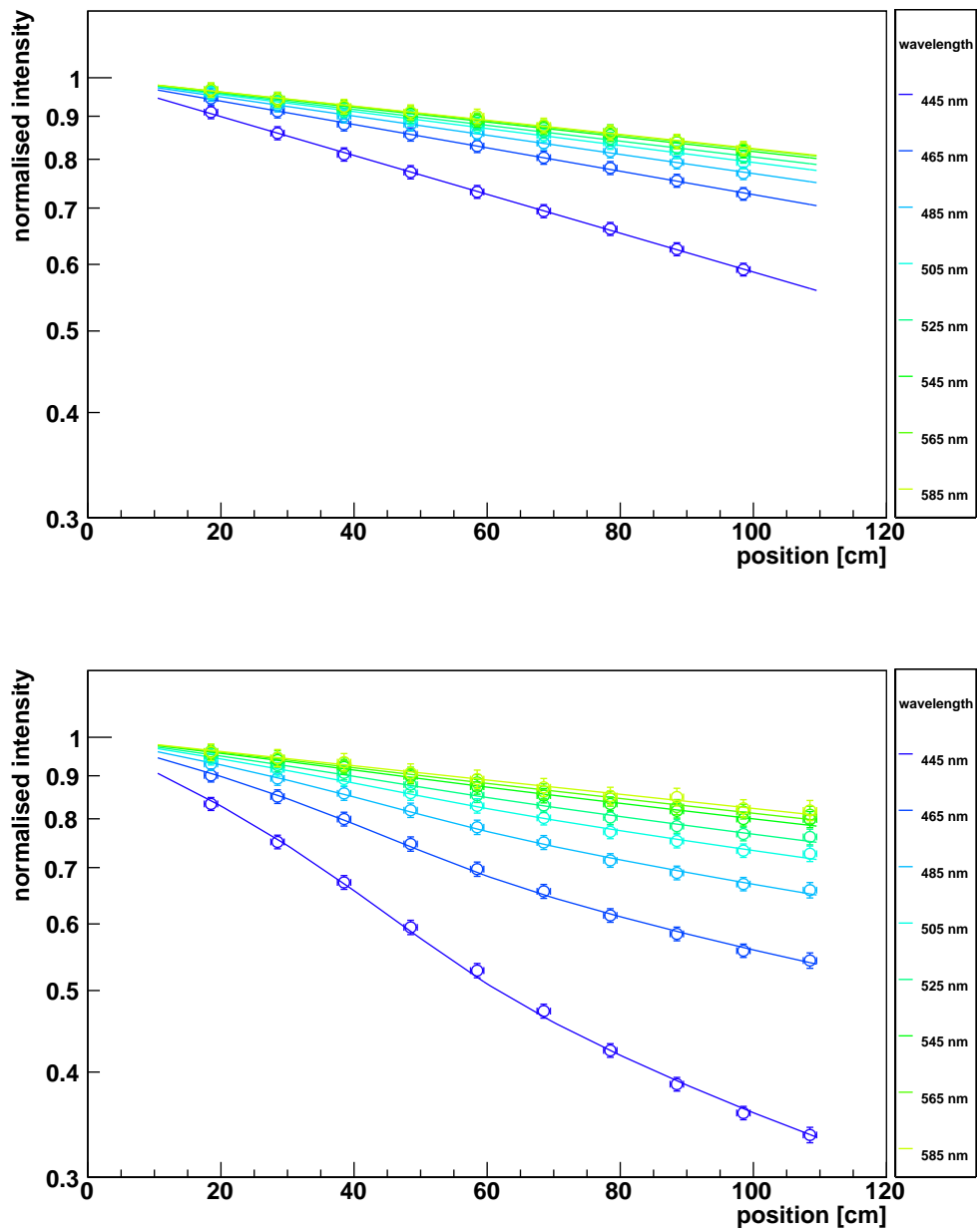


**Figure 6.37:** The intensity trend of module 1 and 3 with corresponding fits. The intensities are normalised to the fit value at 0 cm. The fit functions are explained in the text. The intensity trends including fits for all modules and angles are shown in the appendix.

the  $0^\circ$  measurements for all modules are included in the combined analysis in chapter 6.4.4. To visualize the attenuation after irradiation for the three modules, the additional attenuation per dose is multiplied with the average dose to obtain an average additional attenuation. This is added to the initial attenuation (represented by the attenuation of module 0). The resulting effective attenuations are shown in Fig. 6.39.

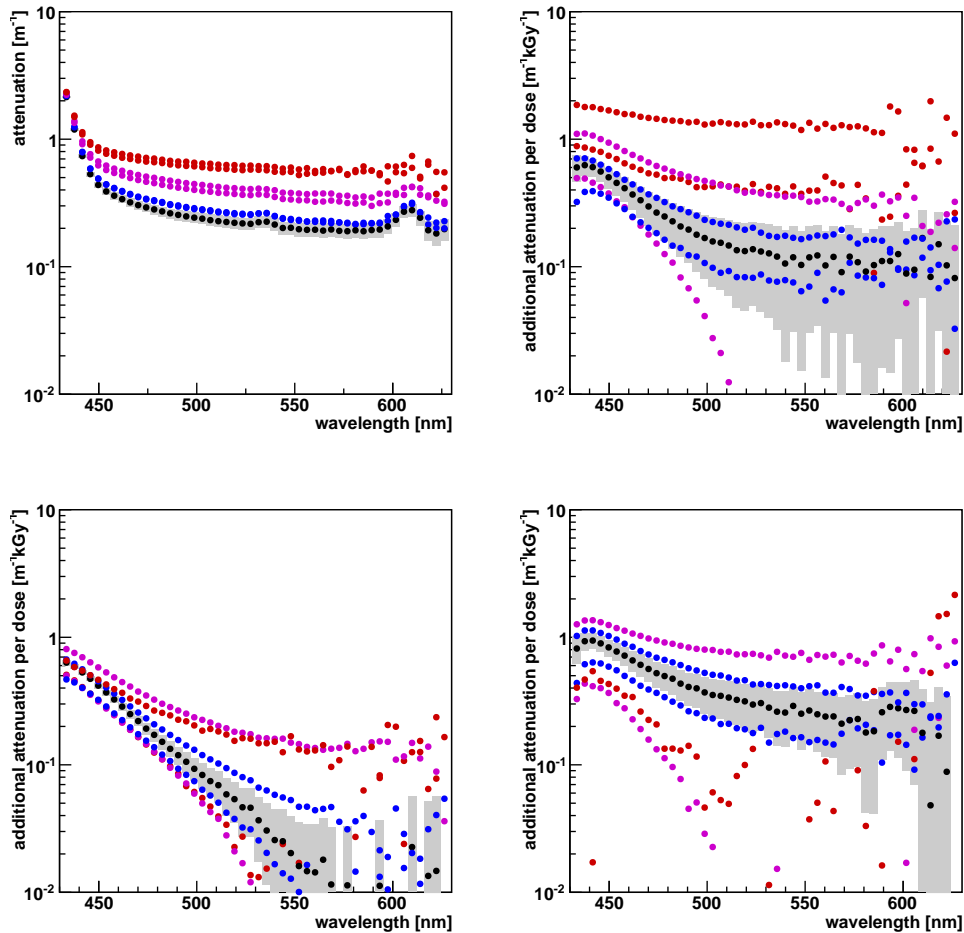


**Figure 6.38:** The attenuation for different photon exit angles for module 1 (top-left) and the additional attenuation per dose for module 2-4 (top-right, bottom-left, bottom-right). The trends for the different exit angles are colour coded in black, blue, purple and red with increasing absolute angle ( $0^\circ$ ,  $\pm 20^\circ$ ,  $\pm 40^\circ$ ,  $\pm 60^\circ$ ). The uncertainties for the  $0^\circ$  measurement are shown as grey area, whereas they are not shown for the other angles.

### 6.4.3 Other measurements

Several irradiation campaigns were carried out by the LHCb SciFi group. At first mainly high dose irradiations were performed at beam lines. After that the focus shifted to

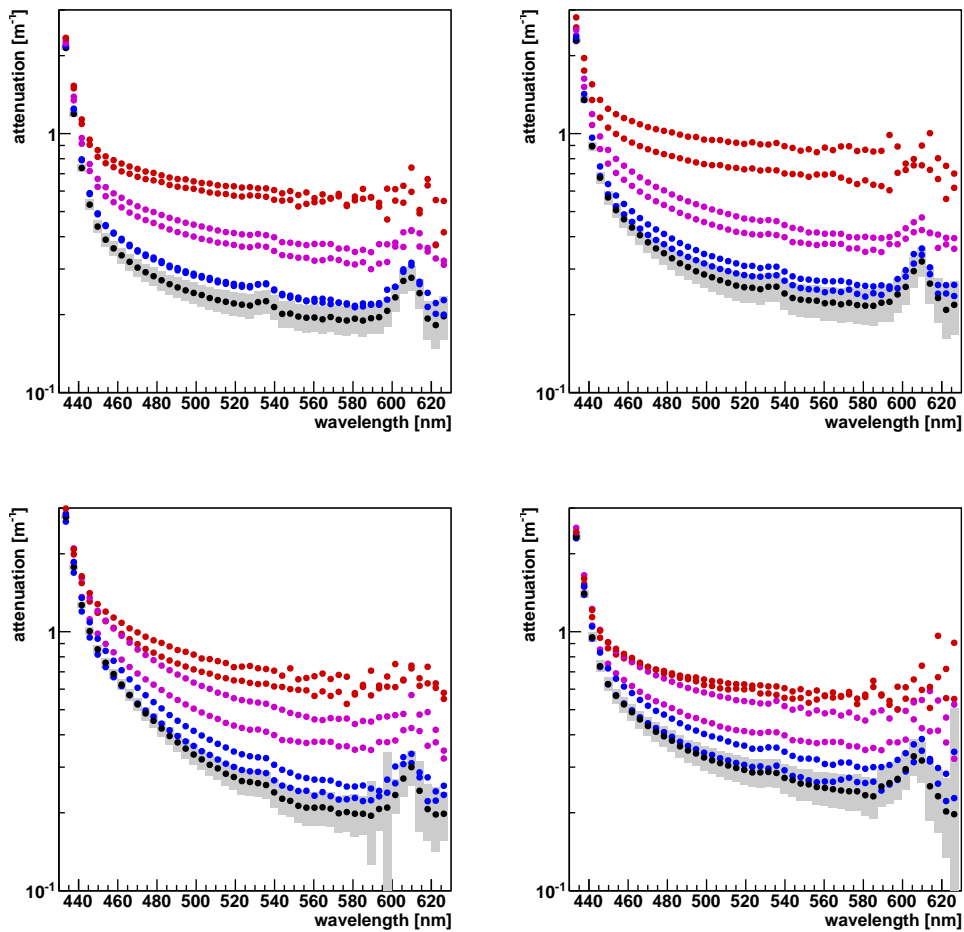


**Figure 6.39:** The attenuation for different photon exit angles for module 1-4 (top-left, top-right, bottom-left, bottom-right). The attenuation shown for module 2-4 is obtained by multiplying the attenuation per dose with the average dose for the respective module and adding this to the attenuation of module 1. The trends for the different exit angles are colour coded in black, blue, purple and red with increasing absolute angle ( $0^\circ$ ,  $\pm 20^\circ$ ,  $\pm 40^\circ$ ,  $\pm 60^\circ$ ). The uncertainties derived from the fits for the  $0^\circ$  measurement are shown as grey area, whereas they are not shown for the other angles.

investigate the damage at low doses, which in addition enable an irradiation at low dose rates. The majority of the measurements was initially performed with non-wavelength dependent photo-detectors (e.g. SiPM) which are typically easier to handle. Measuring the attenuation based on the sum of all wavelengths and angles leads to results which depend on the setup. Like this it is not possible to directly compare the results, or a certain systematic uncertainty has to be tolerated.

One approach to account for the different setups (irradiation and measurement) is to simulate these in detail with the single fibre simulation. This was performed in a thesis in the Dortmund SciFi group [54]. Like this different radiation damage models can be compared to the measurement results. The results of this study are shortly addressed in the following section.

To evaluate the wavelength dependent radiation damage with the help of the own measurements it is required to measure the irradiated fibres with a spectrometer. For this purpose many measurements were redone in the LHCb SciFi group. They are shortly explained in the following, the results are analysed in the succeeding section.

**Ru106** This irradiation campaign was performed in the Dortmund group. Nine fibres with a length of about 7 m were wound around a cylinder. Four  $^{106}\text{Ru}$  eye applicators<sup>10</sup> (beta emission) with a total activity of about 50 MBq were rotated around the cylinder to irradiate the fibre simultaneous and homogeneous. The achieved dose is 70 Gy with a dose rate of  $1.3 \times 10^{-4} \text{ kGy h}^{-1}$ . The results presented here were obtained measuring the attenuation of the fibres after the irradiation. The challenges of this irradiation campaign are small mechanical damages to the fibres caused by kinks developed at edges of the cylinder (which were corrected in the analysis) and the low damage due to the low dose. The results are not published so far, the data used here was provided privately [109], the setup is explained in [110]. Only the results of the fibre which was mechanically damaged the least is used here.

**AAA** A 3 m long fibre was irradiated and analysed by the CERN group. The fibre was rolled up in a case, surrounded by a radioactive liquid (Fludeoxyglucose, usually used in positron emission tomography) which was provided by the company AAA<sup>11</sup>. The reached dose (mainly induced by positrons) is 0.34 kGy with a dose rate of  $2 \times 10^{-2} \text{ kGy h}^{-1}$ . The fibre was mechanically damaged at one position of the loop, which caused some kinks, the designated light loss was corrected in the analysis. The results are not published yet, they were provided privately [111], the setup is explained in [110].

**PS** A bundle of eight scintillating fibres was irradiated at the CERN PS (24 GeV protons) by the CERN SciFi group. The fibres of about 3 m length were glued to a 1 m long polycarbonate plate, with four straight sections and three short turns. Two of the sections saw just a negligible background level, one was irradiated to 3 kGy with a dose rate of  $1.7 \text{ kGy h}^{-1}$  and the fourth section to 22 kGy with a dose rate

<sup>10</sup>The eye applicators were used to treat eye cancer before

<sup>11</sup>Advance Accelerator Applications, 20 Rue Diesel, 01630 Saint Genis Pouilly, France

of  $0.4 \text{ kGy h}^{-1}$ . The dose rates are actually the average over the irradiation period, the peak rate is much higher. The wavelength dependent attenuation was provided privately [111], the setup is explained in [7].

**KIT** Several bundles of fibres glued to PVC boards were irradiated at the KIT (Karlsruhe Institute of Technology, Campus North) with 22.9 MeV protons by the Heidelberg SciFi group. The results shown here were obtained with a 2 m long fibre bundle glued in a race track shape. Four of the straight sections were irradiated to doses of about 9–43 kGy with dose rates of  $1.1 \times 10^3$ – $2.8 \times 10^3 \text{ kGy h}^{-1}$ . The wavelength dependent attenuation was provided privately [112], the setup is explained in [7].

All data was provided as absolute or additional attenuation as a function of the wavelength with corresponding uncertainties. The uncertainties of all the measurements are all driven by systematics. In many cases this implies that the person performing the measurement or the analysis has to guess the precision / reliability of the data at some point of the analysis. For some measurements this estimation was performed more conservative than in others. For this reason own uncertainties are used for the additional attenuation to ensure that the fit functions treat all the irradiation campaigns equally. Otherwise the measurements with optimistically small uncertainties would dominate the result.

### 6.4.4 Combination of irradiation results

The results of the irradiation campaigns described in the two previous sections are used for a combined analysis of the radiation damage of the attenuation in the fibre. The goal is a functional description of the change of the attenuation which can be used in dedicated simulation studies to predict the light yield over the course of the run time of the detector.

The crucial parameter is the additionally induced attenuation as a function of the wavelength and the dose. Figure 6.40 shows the additional attenuation as a function of the dose, the wavelength is coded in appropriate colours. In this plot and all the following of the same type the attenuation of the CERN PS irradiation at a dose of 3.0 kGy is shown with a dose of 3.3 kGy to be distinguished from the result of the LHC tunnel irradiation. The attenuation at small wavelengths follows a rather smooth trend, while the wavelength dependence is very different for the measurements and no correlation to any parameter is observed.

To better visualize the wavelength dependence, Fig. 6.41 has the wavelength shown on the x-axis while the dose is colour-coded. The wavelength dependent additional attenuation is well described by an exponential function with a constant offset ( $a_r = a_0 \exp(-a_w x) + a_{\text{offset}}$ ). From other studies outside the LHCb SciFi project it is expected that the main damage decreases with the wavelength, caused by permanent absorption centres at low wavelengths, see chapter 6.1.3. However also absorption centres at higher wavelengths were seen by different groups which typically anneal. An additional constant attenuation can also occur when the fibre was mechanically damaged during irradiation or handling, or when the attenuation was worse before irradiation compared to the measure-

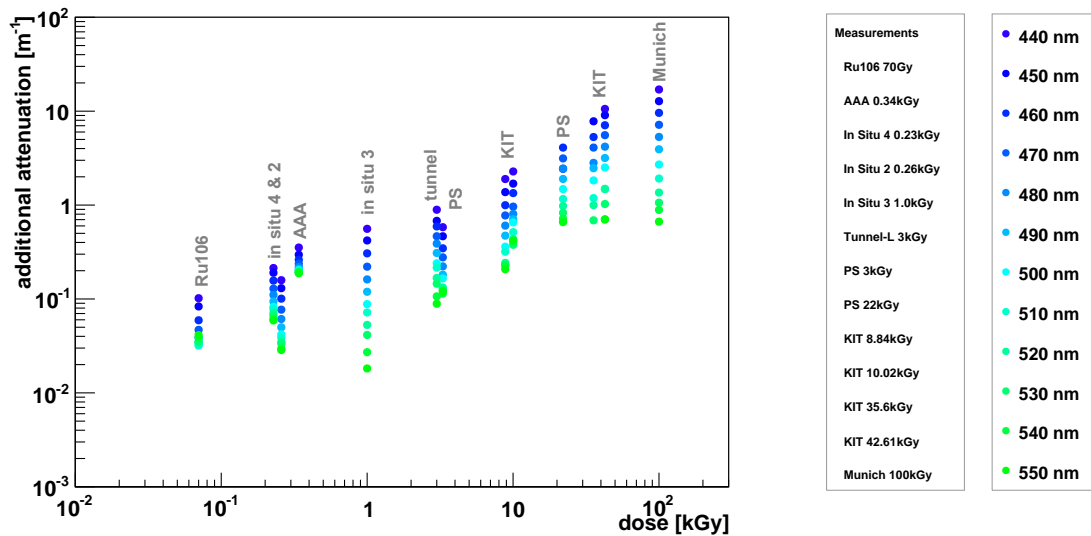


**Figure 6.40:** Additional attenuation for different wavelengths as a function of the dose. The attenuation of the CERN PS irradiation at a dose of 3.0 kGy is shown with a dose of 3.3 kGy to be distinguished from the result of the LHC tunnel irradiation.

ment which it is compared to. For the following analysis it is assumed that the constant offset in attenuation is not caused by the irradiation and is therefore subtracted, only the exponentially decreasing component is considered.

The additional attenuation with subtracted offset is shown in Fig. 6.42. The wavelength dependence is more similar after the correction, although it is not the same. The attenuation increase with dose is not consistent in different literature studies. From basic principle it should increase linear with the dose and saturation effects are not expected to occur within the dose range relevant for the LHCb Upgrade environment (The ratio of damaged molecules is small).

To investigate the behaviour of the results of the LHCb SciFi studies, the additional attenuation per dose is shown in Fig. 6.43. The left plot shows the attenuation per dose as function of the dose. With the given uncertainties it is not possible to judge whether it drops smoothly but it can also not be excluded. One reason for a decreased slope with increasing dose could be a larger chance of recombination of absorption centres, a higher annealing rate.

An alternative reason is the influence of the dose rate. It is expected that the damage is lower at high dose rates than at low dose rates (see chapter 6.1.3). The effect is not expected to be continuously but to separate the data in a high rate and low rate section with a small intermediate region. Figure 6.43-right shows the attenuation per dose as a function of the dose rate. The attenuation seems to be linear with dose for dose rates above  $0.1 \text{ kGy h}^{-1}$ . The attenuation per dose is higher at smaller dose rates, within the uncertainties (which are larger at small doses due to the smaller additional attenuation), it might also be linear

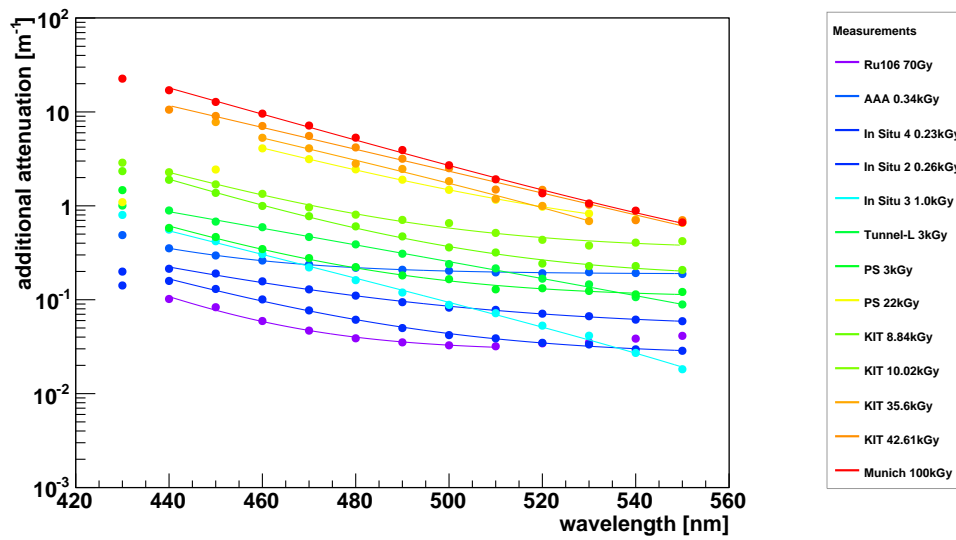


**Figure 6.41:** Additional attenuations as a function of the wavelength. The dose is colour-coded. The lines are fit-functions to describe the data (sum of an exponential decrease and a constant). Only data points with sufficient light yield are used for the fits.

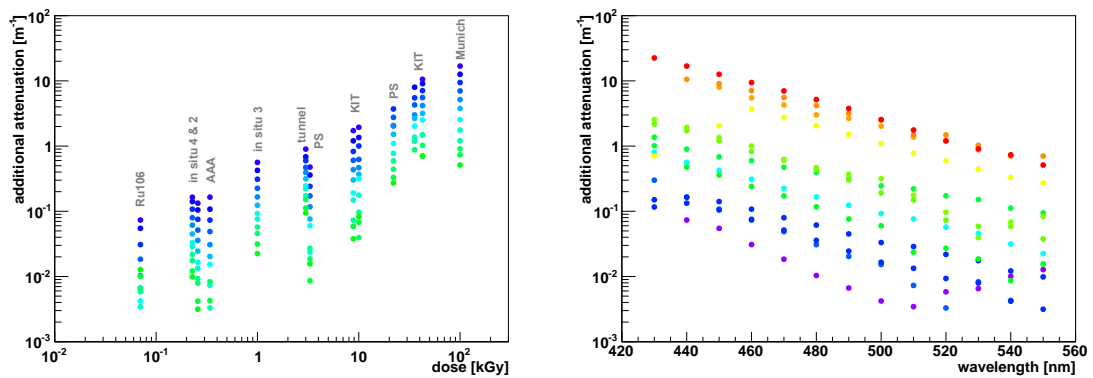


**Figure 6.42:** The additional attenuation corrected for the corresponding constant offsets for different wavelengths (left) and for different doses (right). The legends are shown in Fig. 6.40 & 6.41 respectively.



with the dose. The fact that the additional attenuation of the fibre irradiated in the LHC tunnel (with a low dose rate) is larger than the one of the PS irradiation (with a high dose rate), hints to a dose rate dependence. But this one data point is not enough to prove it, the comparison of the attenuation of these two campaigns with an SiPM showed the inverted result.

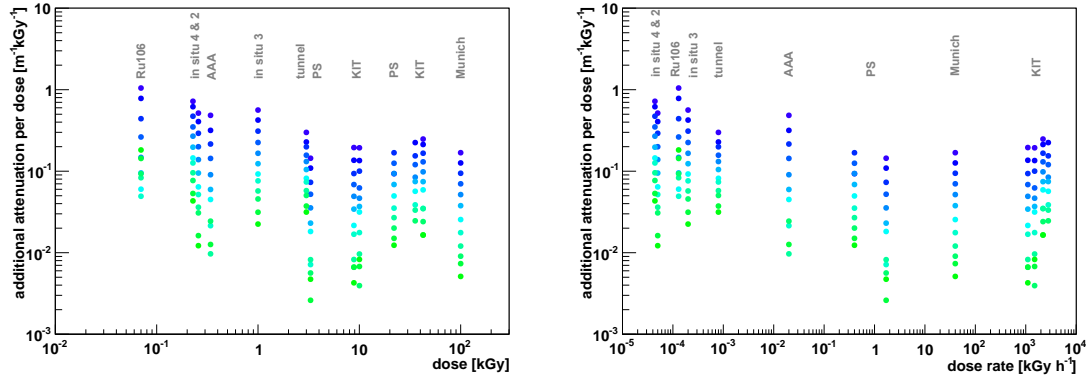


**Figure 6.43:** The attenuation per dose as a function of the dose (left) and as a function of the dose rate (right) for different wavelengths. The legend is shown in Fig. 6.40

With the given data it can not be concluded whether the increase of the attenuation is smaller than linear or the larger dose rate for the high dose irradiations is the cause for the smaller relative damage. To define different models, the trend of the attenuation at 450 nm (peaking wavelength of the fibre spectrum) is considered. To improve the precision the value obtained from the wavelength dependent fit of the attenuation (see above) is used, the obtained values are shown in Fig. 6.44. Two linear functions and a power-law are used to describe the data. The linear fit to the whole data set underestimates the data at low doses. A power-law function is used to describe all data points the best. The pure fit result would result in a description which underestimates the majority of the data points due to a few undershoots, that is why it is adjusted to a larger value in order to describe best the majority of the data. The obtained result for the radiation induced attenuation  $a_r$  as the function of the dose  $D$  is<sup>12</sup>

$$a_{r,pow,450nm} = 0.4D^{0.8}.$$

Assuming that the reduced relative damage for large doses is caused by the higher dose rate, means that these data underestimate the damage expected for the real detector operation. To regard this a linear fit is performed to the low dose rate data only (which are the ones  $\leq 3$  kGy, not including the respective PS irradiation). The result of the fit gives<sup>12</sup>

$$a_{r,lin,450nm} = (3.82 \pm 0.39) \times 10^{-1} D.$$

<sup>12</sup>With the attenuation  $a$  given in m<sup>-1</sup>, the dose  $D$  in kGy and the wavelength  $\lambda$  in nm.

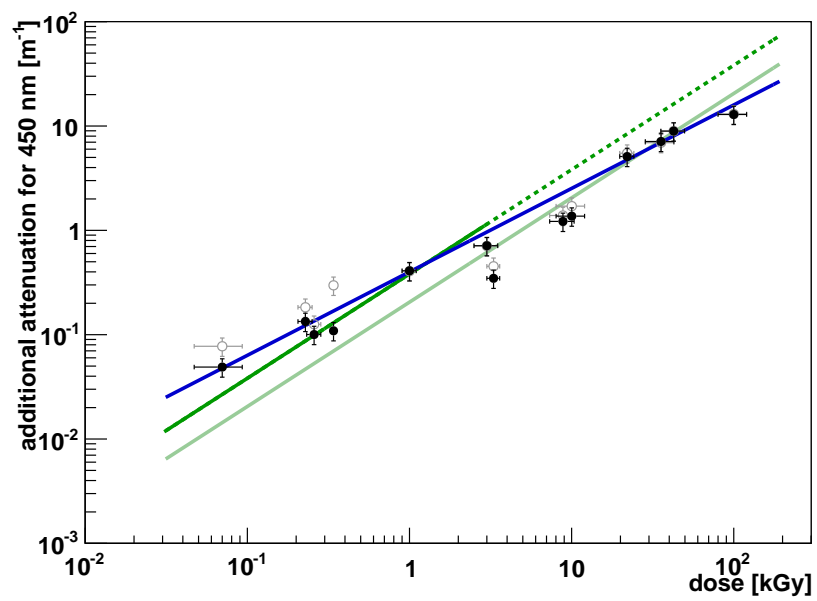


**Figure 6.44:** The additional attenuation for a wavelength of 450 nm. The corrected data is shown in black, while the original data is shown in grey. A linear function (light green) and a power-law function (blue) are adapted to the whole data set. The dark green linear function is fitted to the low dose data only.

To determine the wavelength dependence of the radiation damage the combination of all data is approximated with a single exponential decrease. The resulting radiation induced attenuation as a function of the wavelength  $\lambda$  for the two models is<sup>12</sup>

$$a_{r,\text{pow}} = 0.4D^{0.8}e^{-3.01 \times 10^{-2}(\lambda-450)},$$

$$a_{r,\text{lin}} = 0.38De^{-3.01 \times 10^{-2}(\lambda-450)}.$$

To compare the models to data they are shown in Fig. 6.45 & 6.46. They are shown together with the corrected data (left plots) and the original data (right plots). Under the given circumstances, the data at low doses is well described by both models. By construction the linear model shows a larger damage at high doses. In case the offset in the additional attenuation at large wavelengths is an irradiation effect (original data), both models underestimate the damage in the parameter space of large wavelengths and low doses ( $<0.5$  kGy). The corresponding illustration of the wavelength dependent attenuation of the linear model adapted to all data points and of the two linear models described in [54] are shown in the appendix in Fig. A.14. The latter ones have got an constant offset in the wavelength dependence, thus a larger damage at high wavelengths. Just from the models it is not possible to quantify the effect of the additional attenuation. Due to the inhomogeneous particle density, and the resulting dose profile, a detailed simulation was performed to conclude on the radiation damage.

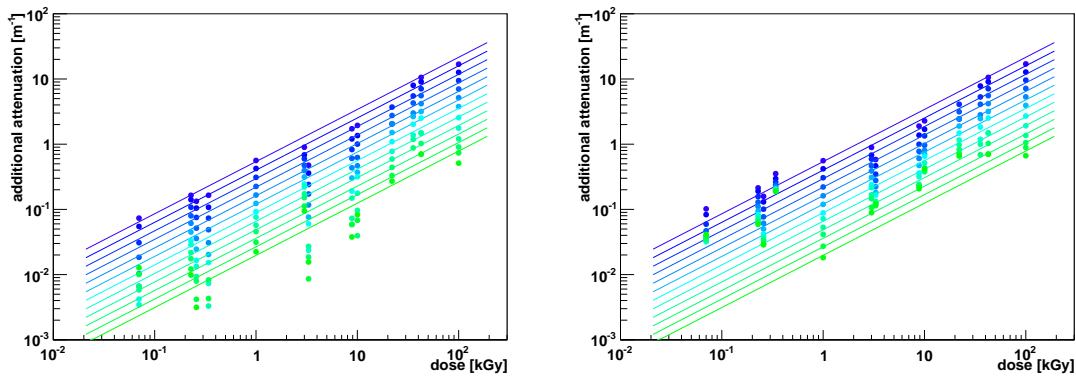


**Figure 6.45:** The attenuation data (left: corrected, right: original data) compared the the power-law model for different wavelengths. The legend is shown in Fig. 6.40

### 6.4.5 Simulation of the light loss due to radiation

The average number of photons detected by the SiPM, the light yield, is a crucial parameter for the performance of the SciFi Tracker. The lower the light yield at a given position, the greater the chance that the number of photons in an event stays below the clustering thresholds, resulting in a reduced single hit efficiency (as described in chapter 4.3.4). The light yield is not equal across the detector plane, it is reduced to the middle ( $y=0$ ), due to

## 6 Scintillating fibres research

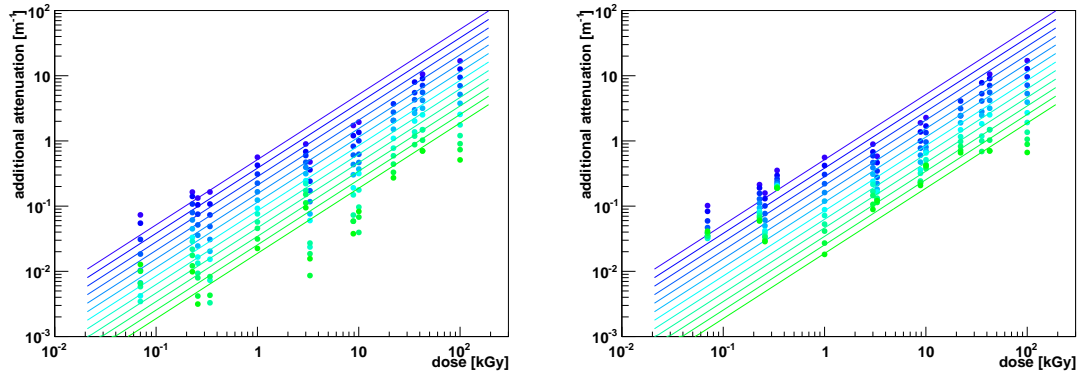


**Figure 6.46:** The attenuation data (left: corrected, right: original data) compared the linear model adjusted to the low dose data for different wavelengths. The legend is shown in Fig. 6.40

the attenuation in the fibres. To evaluate the impact of the radiation damage, the reduction of the light yield is simulated.

This is performed by the dedicated attenuation map simulation developed by the Dortmund SciFi group [113]. It is based on the single fibre GEANT4 simulation and simulates the relative light yield for a detector layer. To account for the irradiation damage, it utilises a dose map and the radiation damage models defined in the previous section. The simulation is briefly described in the following.

To simulate the relative light yield, not every single fibre is considered. The granularity is given by the dose map. Effective March 2016, the recommended dose map is based on a bin size of  $100 \times 100 \text{ mm}^2$  [114, 115] (the impact of the bin size is discussed later). Since the detector is built symmetric, only one quarter of a layer is simulated. The fibres are positioned parallel to the y-axis, along the middle of the dose map bins. The excitation points along the fibre are positioned at the bin junctions, thus the mean dose in between two excitation points is given correctly by the dose map. To be more precise the excitation points are shifted by  $+0.5 \text{ mm}$ , an excitation right at the fibre end would not give the correct results. A GEANT4 simulation is performed at every excitation point, for which the dose map provides the dose profile along each fibre. The single fibre simulation returns the photons with corresponding wavelengths which reach the fibre end. These are added up, respecting the wavelength dependent photon detection efficiency of the SiPMs. That way the attenuation map simulation provides two dimensional histograms, giving the relative amount of photons reaching the fibre end, compared to the number initially produced by the first dopant in the fibres. This map is provided separately for the photons travelling direct to the SiPMs and the ones which were reflected by the mirror. The data used in the following was provided by [116].

The used dose map is shown in Fig. 6.47. It gives the dose for an integrated luminosity of  $50 \text{ fb}^{-1}$  for the first detector layer of T1. The dose profile is widespread in the horizontal direction due to the dipole field of the magnet, thus the bin with the largest dose is the

one on the side of the beam-pipe. The maximum dose is 14.4 kGy, which is about a factor two lower than the peak value stated before (in chapter 4.3.1). The latter value was obtained with a dose simulation of circular arranged bins, which can not be used here. The bin size along the fibres does not have large impact, since the radiation damage is linear along the extension of a bin. However it implies that the worst excitation point simulated is at position  $(x,y) = (150\text{ mm}, 0.5\text{ mm})$ , which is equivalent to a beam-pipe hole width of 300 mm. To simulate beam-pipe holes with divergent sizes, a dose map with higher granularity is required. A new map with a bin size of  $25 \times 25\text{ mm}^2$  (in  $x,y$ ) is currently produced by the corresponding LHCb group [115]. It will be implemented when available.

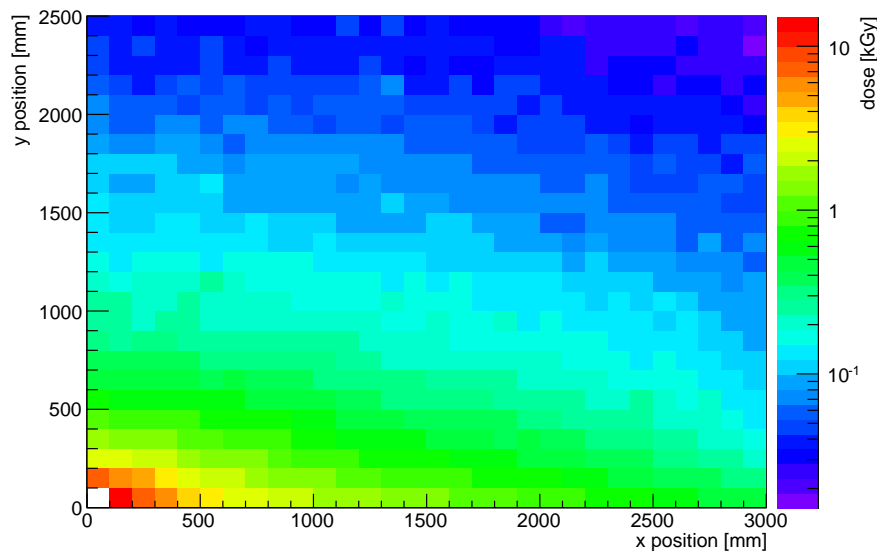


**Figure 6.47:** The dose map used for the attenuation map simulation. The simulated dose is given for an integrated luminosity of  $50\text{ fb}^{-1}$  for one quarter of T1. The same figure with written-out numbers is shown in the appendix, see Fig. A.15. The data was provided by [114].

The provided maps give the relative light yield, separated for direct and reflected photons. These are added respecting the mirror reflectivity of 80 %. The result is scaled with the result that the maps give the absolute light yield. The factor is chosen such that the light yield next to the mirror matches the value determined in the test beam (16 p.e. [8]). This number is not expected to be correct for the final detector (as discussed in the following), it is used to illustrate the effect of the radiation damage. The resulting light yield maps for the unirradiated detector and the irradiated detector for the power-law model and the linear model are shown in Fig. 6.48. The light yield separated for the direct and reflected light are shown in Fig. A.16 in the appendix.

There are several reasons why the absolute light yield is different for the real detector, which are explained in the following. The effective reflectivity of the mirrors in the

## 6 Scintillating fibres research

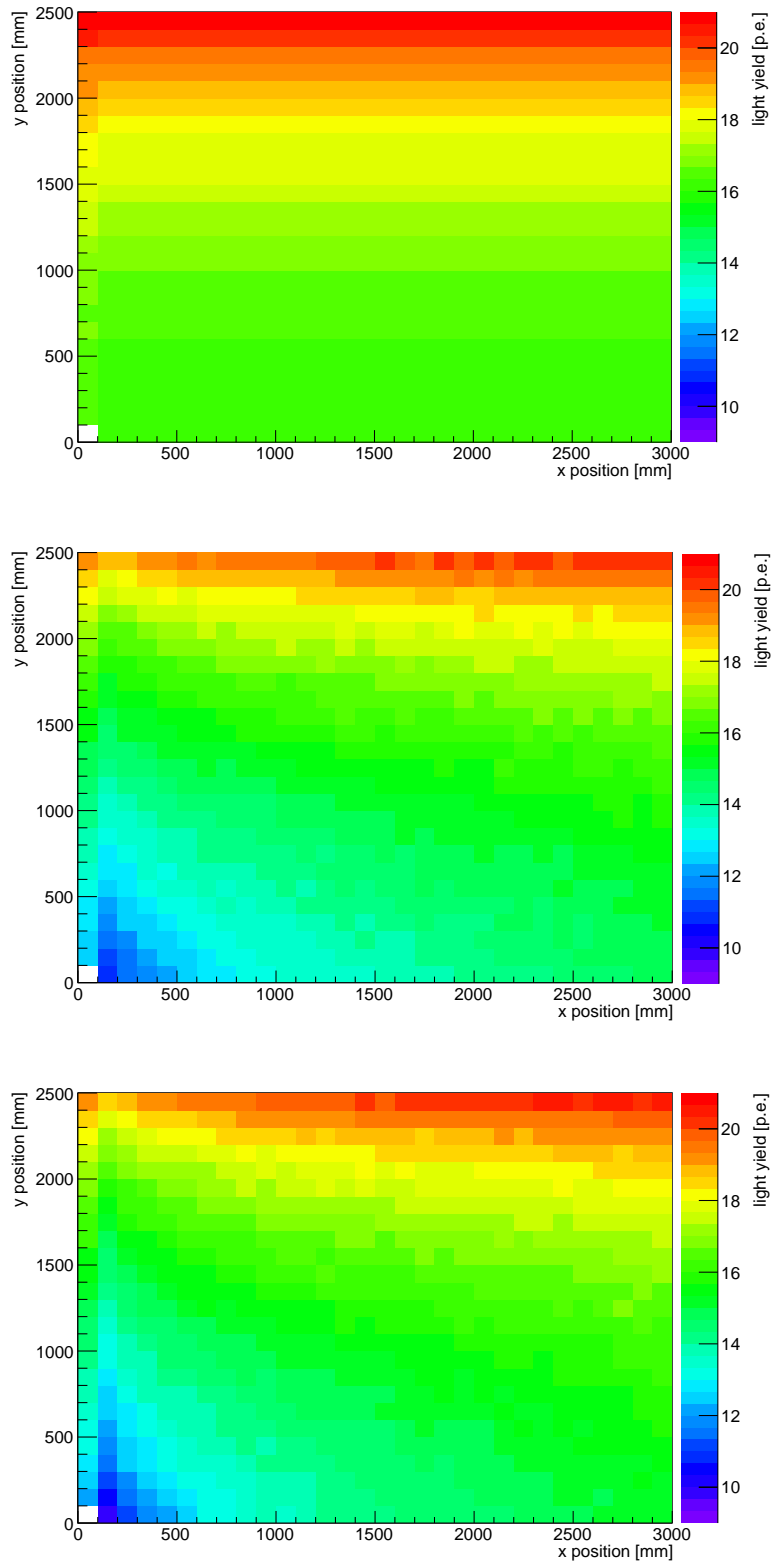


**Figure 6.48:** Simulated light yields for no irradiation (top), power-law model (middle) and linear model (bottom). The same figure with written-out numbers is shown in the appendix, see Fig. A.17.

test beam was lower than expected, probably due to the attachment [61]. An improved mounting would directly increase the light yield. The time response of the electronics is not included in the simulation at this stage, taking this into account would reduce the yield close to the SiPMs. The light yield measured at the test beam is not the true average number of photons detected, but the mean number in a cluster. These two numbers are different because of the clustering thresholds applied. The effect is larger for a small number of photons, than for a large light yield. Due to these effects, it is not meaningful to convert the simulated light yield to a single hit efficiency, more sophisticated studies are need for this.

To compare the effect of the two radiation damage models among themselves and to previous studies, the ratios of the light yields are computed. The two maps showing the ratio of the light yield after to before irradiation are shown in Fig. 6.49. To compare the models among themselves the ratio of the light yield of these two is also shown. As expected the damage is the largest close to the beam-pipe, the outer half of the tracker shows a reduction in light yield of below 10 %. The relative light yield for the worst case bin close to the beam-pipe is 67 % and 62 % for the power-law model and the linear model respectively. The slightly better result compared to the previously quoted number of 60 % [8] is most probably caused by the y-position of 150 mm of the fibre under study. The two models studied in [54] resulted in 63 % and 42 % respectively, caused by the larger damage at high wavelengths. To judge the overall influence of the radiation damage, an estimate for the mean reduction of the light yield is performed. To account for the increased density of tracks in the central region, the values in the plane are weighted with the dose at the corresponding position. The average relative light yield is 83 % for both models. The larger damage at high doses for the linear model is balanced by the slightly lower damage at low doses, see Fig. 6.49 (bottom).

## 6.5 Summary & outlook

One of the crucial parameters for the performance of the SciFi Tracker is the light yield, the number of photons detected by the silicon photomultipliers. For a given noise rate of the SiPMs it determines the signal to noise ratio. The initial number of photons produced in the fibre, the attenuation along the fibre and the photon detection efficiency of the SiPMs are the parameters defining the light yield. Especially the attenuation is not simply determinable from lab measurements or test beam campaigns. It is a combination of absorption and scattering in the material and losses at the reflection at the boundaries between core and cladding and in between the claddings. The effective attenuation seen in the detector is a function of the wavelength spectrum, the angular distribution and the used read-out electronics, and is therefore not the same for different measurement setups.

Thus, it is essential to perform detailed simulations. The variety of parameters needed for a detailed fibre simulation require the constant comparison to new measurements. These can be used as input to tune the parameters, and therefore to improve the simulation.

## 6 Scintillating fibres research

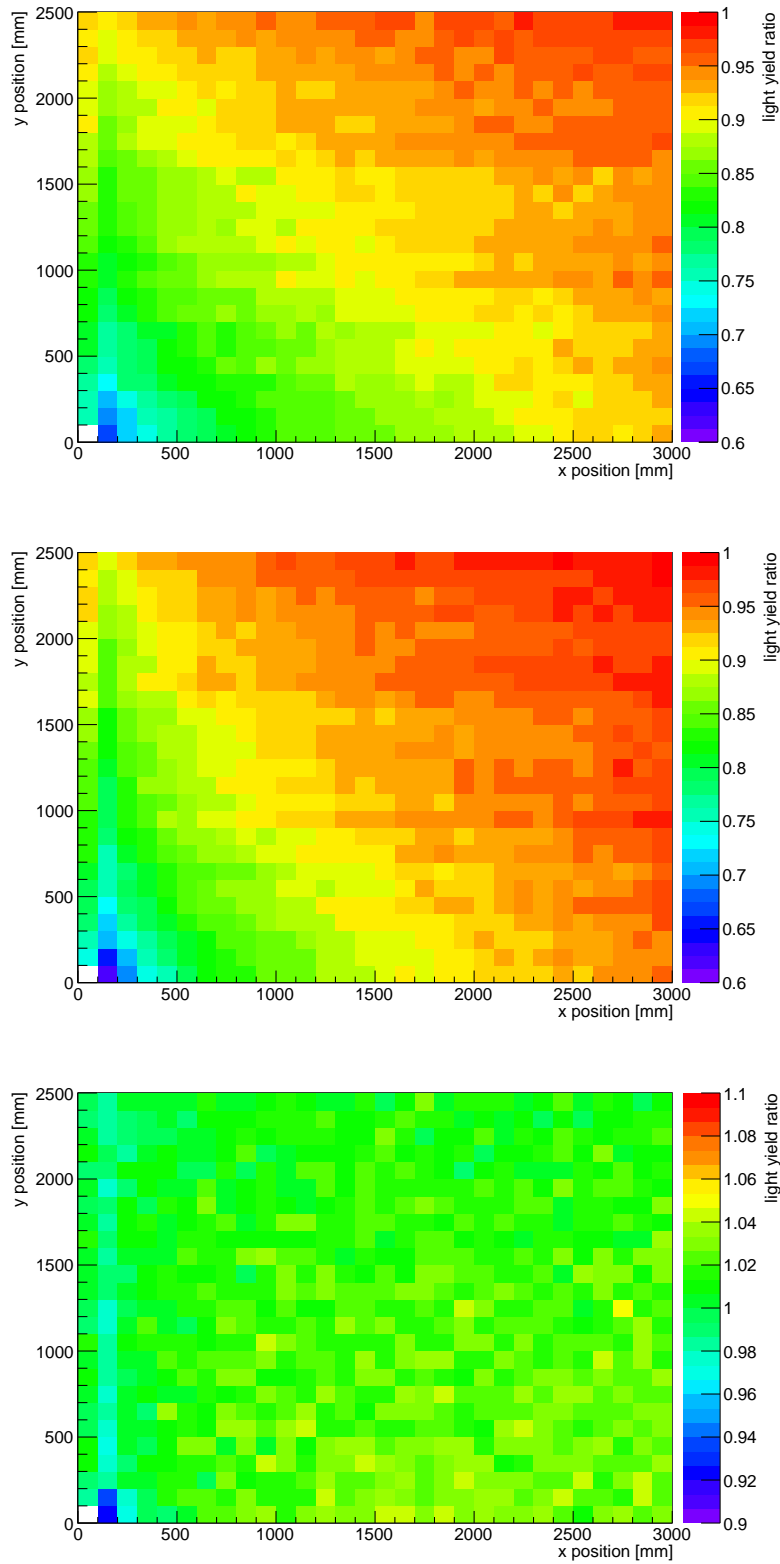


**Figure 6.49:** Simulated ratios for the light yields of power-law model / no irradiation (top), linear model / no irradiation (middle) and linear model / power-law model (bottom). The same figure with written-out numbers is shown in the appendix, see Fig. A.18.



The available GEANT4 simulation developed in the Dortmund SciFi group describes the transmission of the photons through the fibre on the level of single photons. Measurements of the intensity and the attenuation as a function of the photon exit angle were used to tune the parameter of the loss probability at the boundaries. The tuned simulation was used to simulate the influence of measurements under different angles, for example on the average path length of the photons. This knowledge was used in the measurements of the radiation damage campaigns.

The central region of the detector is the most important, most tracks pass the detector close to the beam-pipe. This also implies that the highest dose level and with it the largest radiation damage occurs there. The highest expected dose after the planned runtime of the upgraded detector is about 30 kGy in the most central region [7]. As it drops quickly with increasing distance to the beam-pipe, the major part of the tracker is exposed to a dose of below 1 kGy.

To determine the radiation damage, tests with dedicated fibres were performed. To evaluate the damage at high doses, a bundle of fibres was irradiated with protons at the tandem accelerator at Forschungszentrum Garching to 100 kGy. The angular analysis showed the expected significant increase in the attenuation. A possible radiation damage of the boundary between core and cladding would increase the attenuation for photons travelling under large angles. However this was not observed, thus measurements under small angles can be used to predict the damage for all photons.

The experience of other experiments and dedicated measurements of non-LHCb groups showed that the radiation damage might be larger at small dose rates. The typical dose rate of the irradiation campaigns at beam lines is several orders of magnitude higher than the expected rate for the SciFi Tracker during data taking. Therefore three bundles of scintillating fibres were irradiated in situ in the LHCb cavern. The dose profile along the fibres is not homogeneous, but follows the particle density distribution of the experiment. To determine the radiation induced attenuation, the data points were described using a function whose attenuation follows the dose profile. The additional attenuation per dose is about a factor three larger compared to the proton irradiation.

To define a wavelength dependent radiation damage model, the measurement results of the LHCb SciFi group were collected. From basic principles, it is expected that the damage increases linear with dose. However, the data shows a lower damage per dose at higher doses. Saturation of the initial damage is not expected in the dose range, but an increased annealing yield could explain the lower relative damage at high doses. To describe this scenario, a power-law model was adapted to the data. An alternative explanation for the lower relative damage at high doses could be the systematically higher dose rate at these irradiation campaigns. To account for this, a linear dependence was adapted to the low dose rate data only. In both models the wavelength dependence is described by an exponential decrease of the damage with increasing wavelength.

Both radiation damage models were used to estimate the relative light loss due to irradiation. To achieve this, the models were used as input for the simulation developed by the

## 6 Scintillating fibres research

Dortmund SciFi group. Using the single fibre implementation in GEANT4, it simulates the light loss along the fibres for the respective dose profile in a station of the SciFi Tracker. The resulting relative light yield for the worst case bin close to the beam-pipe is 67 % and 62 % for the power-law model and the linear model respectively. The average light yield for all particles is 83 % for both models. These values will be updated when a dose map with higher granularity is available.

The results lie within the expectations from the previous models, which were used to prove the feasibility of the LHCb SciFi Tracker. However, the new analysis allows for more detailed tests of the tracking performance by the LHCb SciFi group. The attenuation maps will be used to study different detector geometries. Especially the upcoming maps with higher granularity will enable studies of the radiation damage in the central region.

For the design of the beam-pipe hole, the naive approach is to choose a shape which is as small as possible. This is realised by a step shape design, where the step width (in x-direction) is defined by the SiPM array width. As shown in Fig. 6.49, the damage in the most central region also effects the light yield for hits in a larger distance. This is caused by the significant reduction of the mirrored light. A beam-pipe hole shape with larger dimensions will therefore increase the efficiency in the active part of the detector on top and below the cut out. This effect might increase the overall efficiency, although the hits close to the beam-pipe are lost.

The wavelength dependent model enables more detailed simulations. For example a change of the wavelengths dependence of the photon detection efficiency of the SiPMs would be described correctly. A major improvement is expected from the usage of new scintillating fibres with NOL additives. Independent of an enlarged light yield, the shift of the emission spectrum to longer wavelengths would reduce the effective radiation damage. The production of NOL fibres is still under development. In case possible, they will be used in the innermost modules, which will be produced the last. Before dedicated irradiation campaigns are performed, the expected effect can be studied with the single fibre simulation.

# 7 Conclusion

The upgrade of the LHCb detector in the LHC long shutdown 2 in 2019/20 involves the replacement of several sub detectors. The tracking stations, currently separated in a silicon-strip Inner Tracker and a drift-tube Outer Tracker, will be replaced by a single technology detector, the Scintillating Fibre Tracker. It is based on thin scintillating fibres arranged in 2.5 m long multiple layer fibre mats, read out by silicon photomultipliers.

Two of the major challenges are the harsh radiation environment for the scintillating fibres and the construction of the modules. It is the first time that scintillating fibres are used in conditions as present in the LHCb upgrade scenario, and fibres with a diameter of only 250  $\mu\text{m}$  were never used to build a detector covering a total area of about 360  $\text{m}^2$ . The studies presented in this thesis constitute a large share of the R&D performed on these two topics.

A machine to process scintillating fibres to multi-layer fibre mats was designed and built. It is based on a rotating wheel of about 1 m diameter on which the fibre is wound. A thread guides the fibre to ensure a reliable precise positioning. The optimised design of pins from glue produced during the winding ensures the precise alignment of the fibre mats in the modules. This prototype machine enabled to test different production techniques and fibre mat designs. The produced fibre mats proved the feasibility of the production principle, for example for the construction of the full size module for the Engineering Design Review. In addition multiple mats were built for the test beam campaigns to test the performance of the SciFi Tracker.

For the serial production of about 1300 fibre mats at four winding centres an optimised machine was designed in collaboration with a company. It ensures the compliance of the required reliability, operability and working safety. As one of the winding centres, the Dortmund SciFi group will produce about 20% of the fibre mats. The Production Readiness Review for the Dortmund group will take place in Q2 2016.

One of the crucial parameters of the SciFi Tracker is the hit efficiency. To achieve a high efficiency a low noise rate of the SiPMs and a high light yield of the scintillating fibres are essential. The amount of light reaching the SiPMs is reduced by the radiation damage of the fibres, which increases the attenuation along the fibre. The attenuation in the fibres has a strong wavelength dependence and is larger for photons travelling under a large angle through the fibre. These effects have to be accounted for in the analysis of the attenuation.

Irradiation tests were performed with a proton beam to a dose of 100 kGy and in situ in the LHCb cavern to a dose of about 1 kGy. The high dose irradiation at the tandem accelerator showed the expected significant increase of the attenuation (about a factor 30). The in situ

## *7 Conclusion*

irradiation enabled the study of the damage at low dose rates. The determined radiation induced absorption per dose is about a factor three larger compared to the proton irradiation. The obtained data was combined with the results of other irradiations of the LHCb SciFi group and a wavelength and dose dependent attenuation model was defined. Two models were defined, which were compared with the help of the available fibre simulation of the Dortmund SciFi group.

The relative light yield drops to 67 % and 62 % at the worst case point of the detector respectively. This value lies within the expectation from previous models, which were used to prove the feasibility of the SciFi Tracker. With the help of the new models more detailed studies on the tracking performance by the LHCb SciFi group will be performed. The more detailed implementation of the radiation damage enables the study of different detector geometries and the implementation of new technologies. Especially the possible usage of new fibres with NOL additives is expected to reduce the effective radiation damage significantly.

# A Appendix

## A.1 Proton irradiation

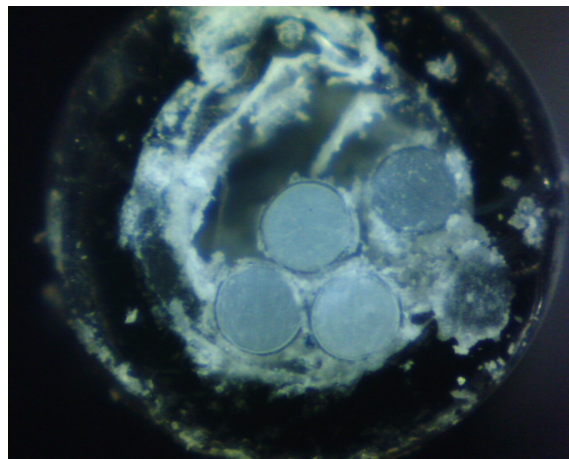


**Figure A.1:** The cross section of the fibre bundle irradiated with protons. The fibres are glued in a glass pipette.

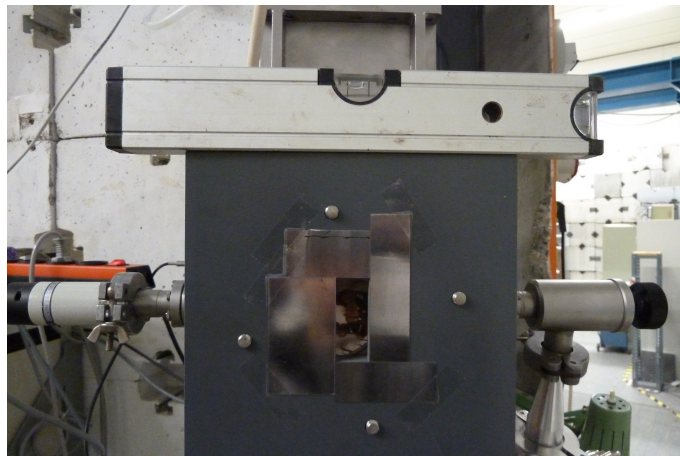


**Figure A.2:** Photograph of the absorber plate at the beam line exit window at the tandem accelerator at Forschungszentrum Garching. The size of the hole is  $1 \times 5$  cm.

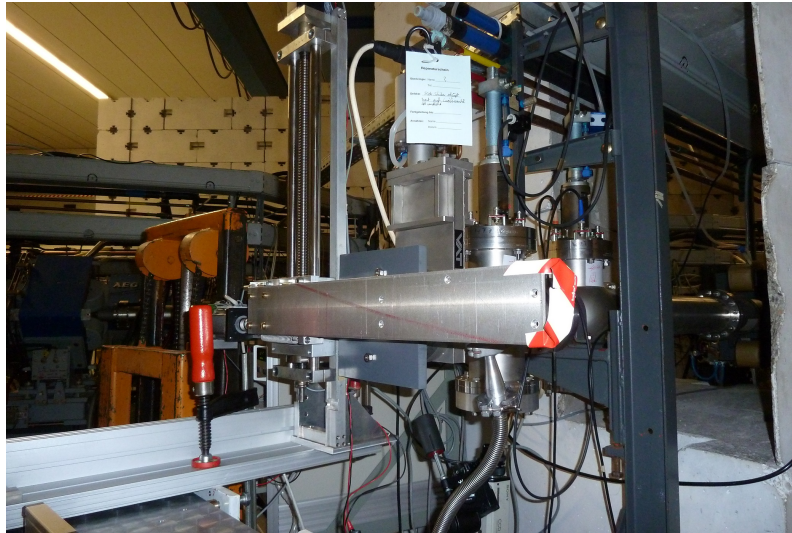


**Figure A.3:** Photograph of the linear slide to move the fibre modules at Forschungszentrum Garching. No fibre module is installed at the slide on the photograph. The linear slide moves the fibres along its length to achieve an uniform dose profile.

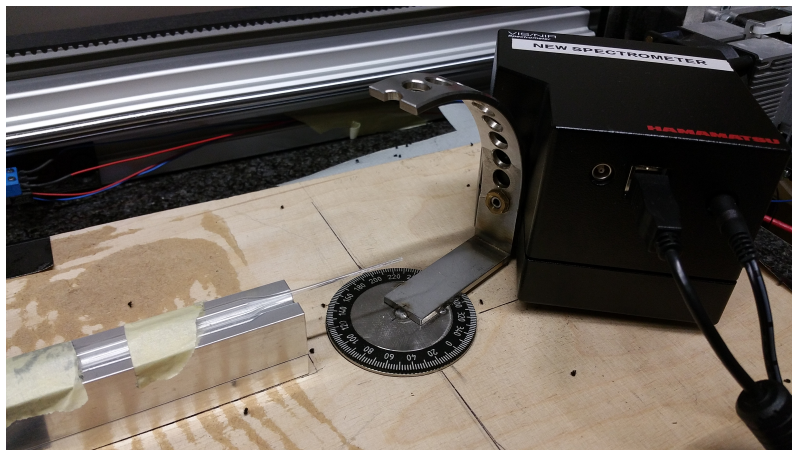


**Figure A.4:** Photograph of the setup to measure the angular intensity with a spectrometer (for the proton irradiated fibres). It is positioned at  $0^\circ$  in the vertical directions and  $+20^\circ$  in the horizontal direction. The fibres are glued in the glass pipette.

## A.2 In situ irradiation

**Table A.1:** The strontium source used for the measurements of the in situ modules in the technical stops had an activity of about 35 MBq. The data for the decay are listed below [117]. The source was kindly provided by the LHCb Outer Tracker group.

	$^{90}\text{Sr}$	$^{90}\text{Y}$
half life	28.9 y	64 h
decay	$\beta^-$ : 100 %	$\beta^-$ : $\approx$ 100 %
energy	0.546 MeV	2.28 MeV
decay product	$^{90}\text{Y}$	$^{90}\text{Zr}$ (stable)

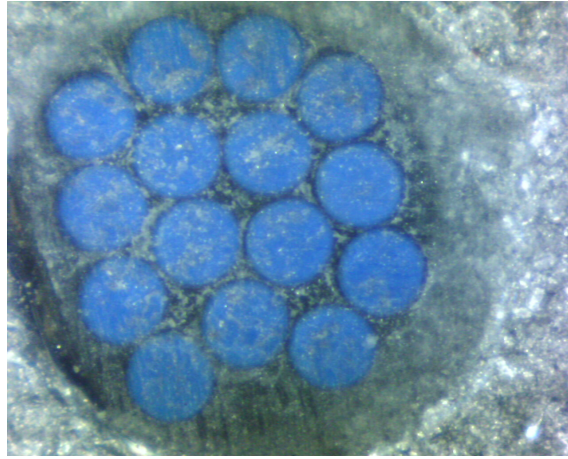


**Figure A.5:** The cross section of a fibre bundle irradiated in situ (module 1).



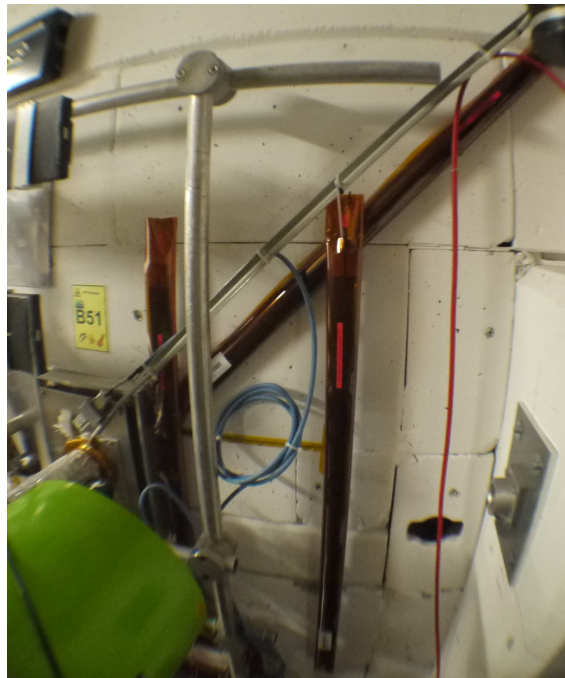


**Figure A.6:** The fibre modules installed in situ in the LHCb cavern at the shielding wall to the tunnel in the VELO-area. The module on the left closest to the beam-pipe is module 2, the one parallel module 3 and the diagonal module is module 4.



**Figure A.7:** Photograph of an in situ fibre module read out during a Technical Stop. The fibres are excited with a Strontium source and read out with an SiPM-usb-module.



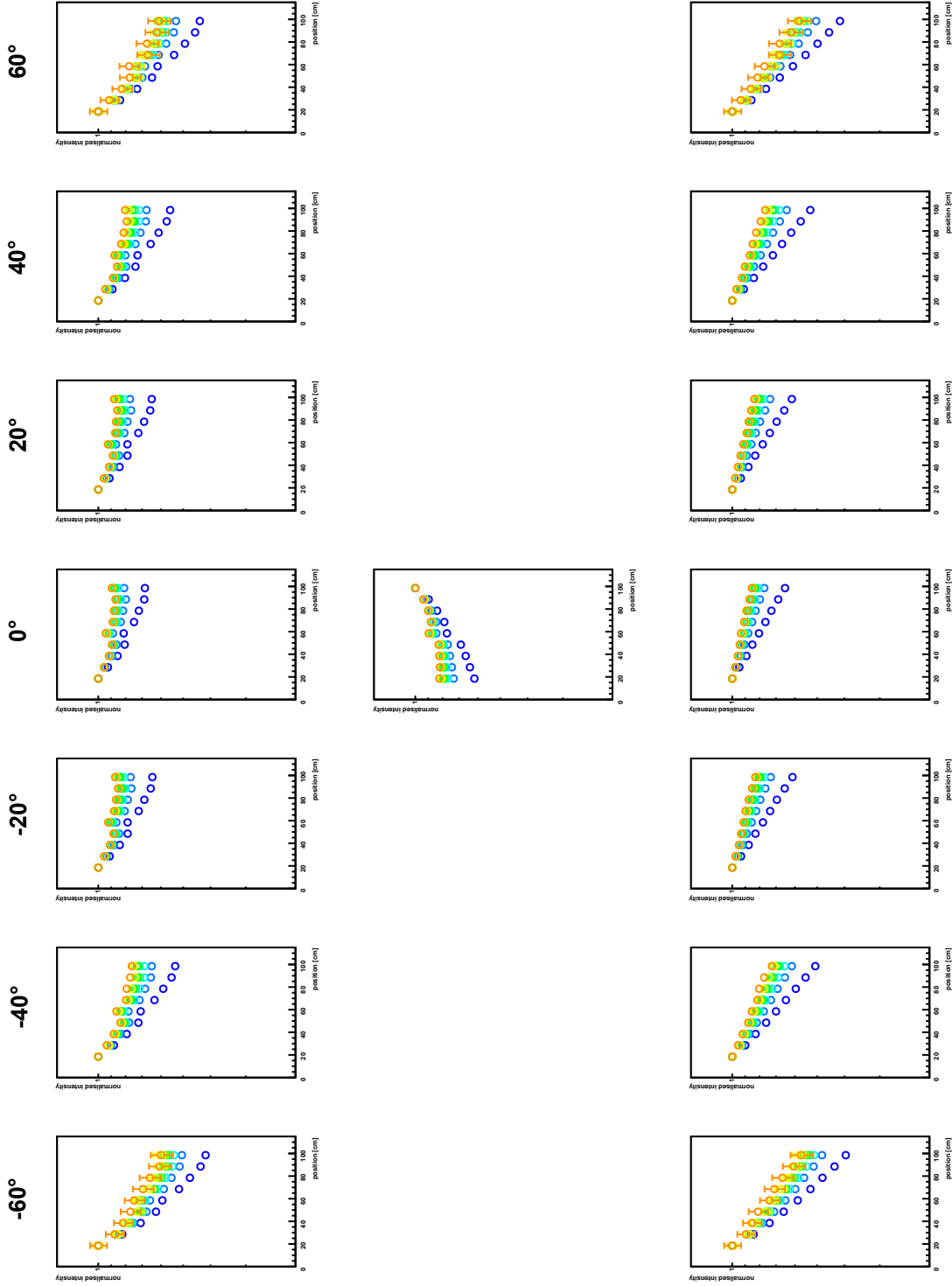


**Figure A.8:** Intensity trend for module 1 (unirradiated) of the in situ irradiation. The top row shows the forward measurements for the photon exit angles from  $-60^\circ$  to  $+60^\circ$  in  $20^\circ$  steps. The middle plot shows the backwards measurements for  $0^\circ$  and the bottom row shows the corrected forward measurements. The colors represent the wavelengths from 445 nm (blue) to 589 nm (orange).

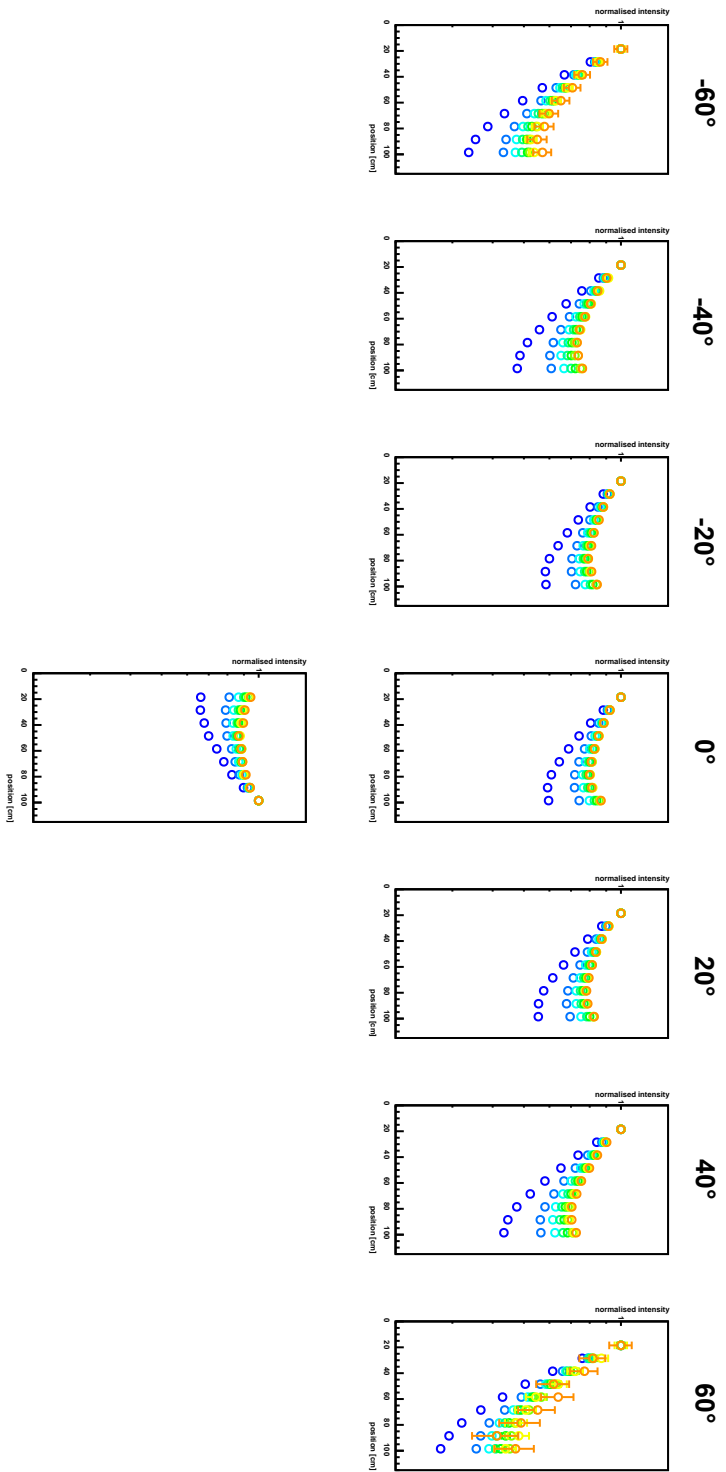


**Figure A.9:** Intensity trend for module 2 of the in situ irradiation. The top row shows the forward measurements for the photon exit angles from  $-60^\circ$  to  $+60^\circ$  in  $20^\circ$  steps. The middle plot shows the backwards measurements for  $0^\circ$  and the bottom row shows the corrected forward measurements. The colors represent the wavelengths from 445 nm (blue) to 589 nm (orange).

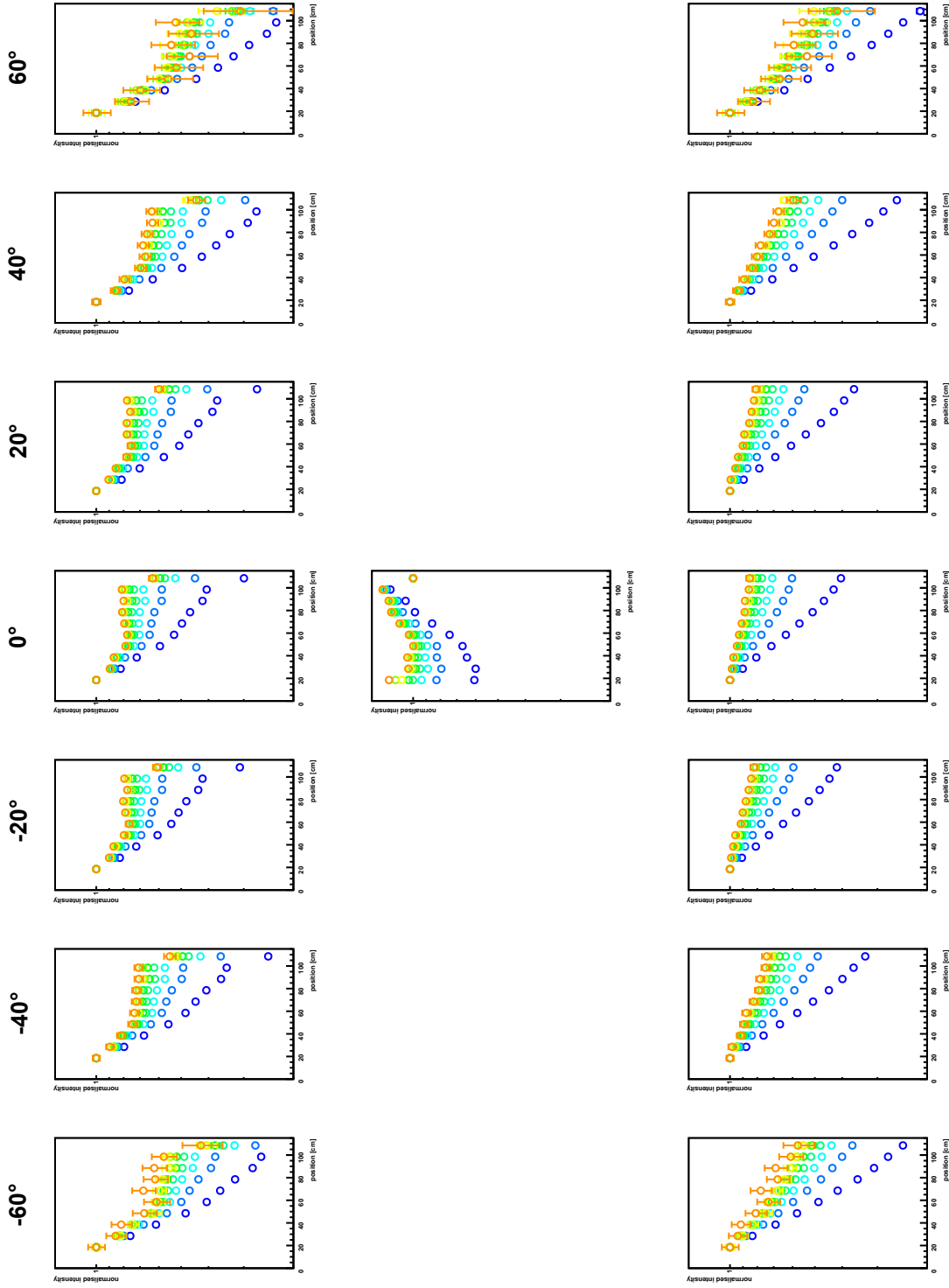


**Figure A.10:** Intensity trend for module 3 of the in situ irradiation. The top row shows the forward measurements for the photon exit angles from  $-60^\circ$  to  $+60^\circ$  in  $20^\circ$  steps. The middle plot shows the backwards measurements for  $0^\circ$  and the bottom row shows the corrected forward measurements. The colors represent the wavelengths from 445 nm (blue) to 589 nm (orange).

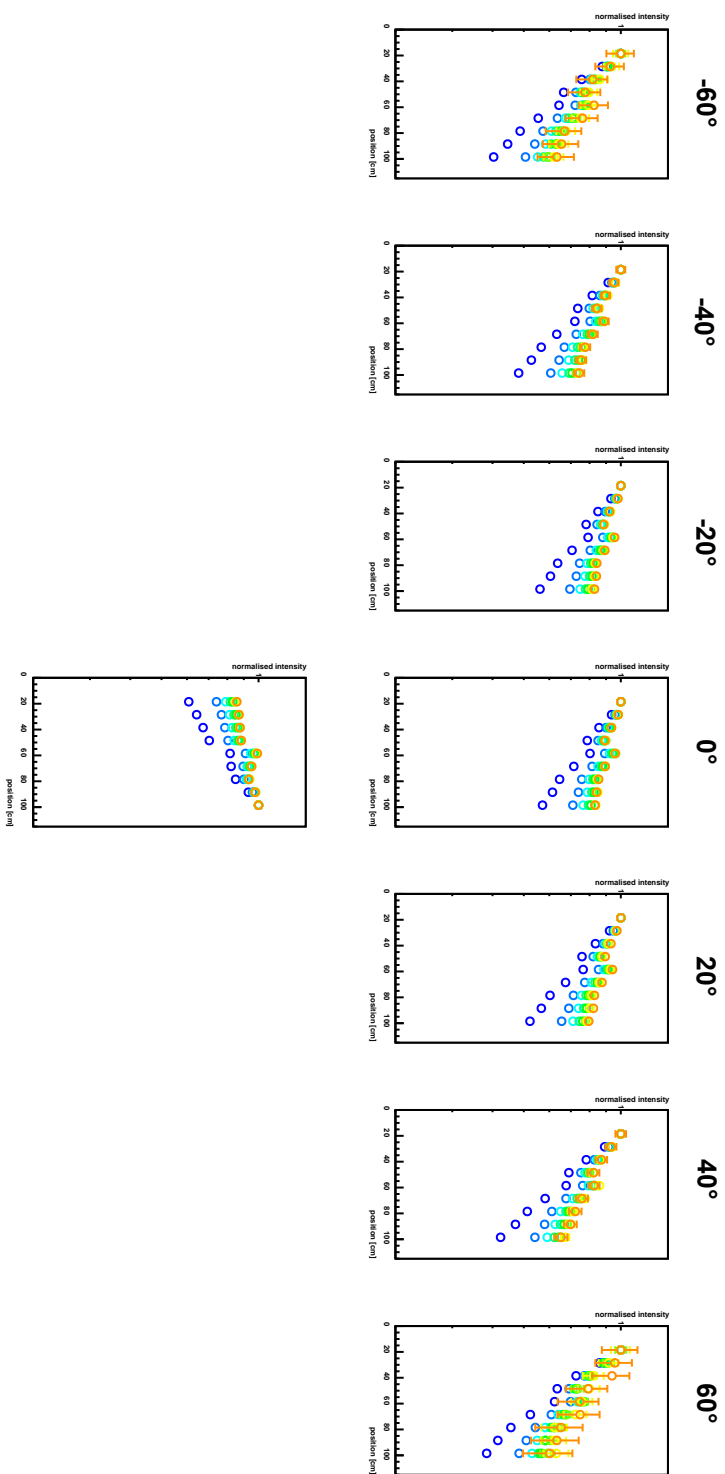


**Figure A.11:** Intensity trend for module 4 of the in situ irradiation. The top row shows the forward measurements for the photon exit angles from  $-60^\circ$  to  $+60^\circ$  in  $20^\circ$  steps. The middle plot shows the backwards measurements for  $0^\circ$  and the bottom row shows the corrected forward measurements. The colors represent the wavelengths from 445 nm (blue) to 589 nm (orange).

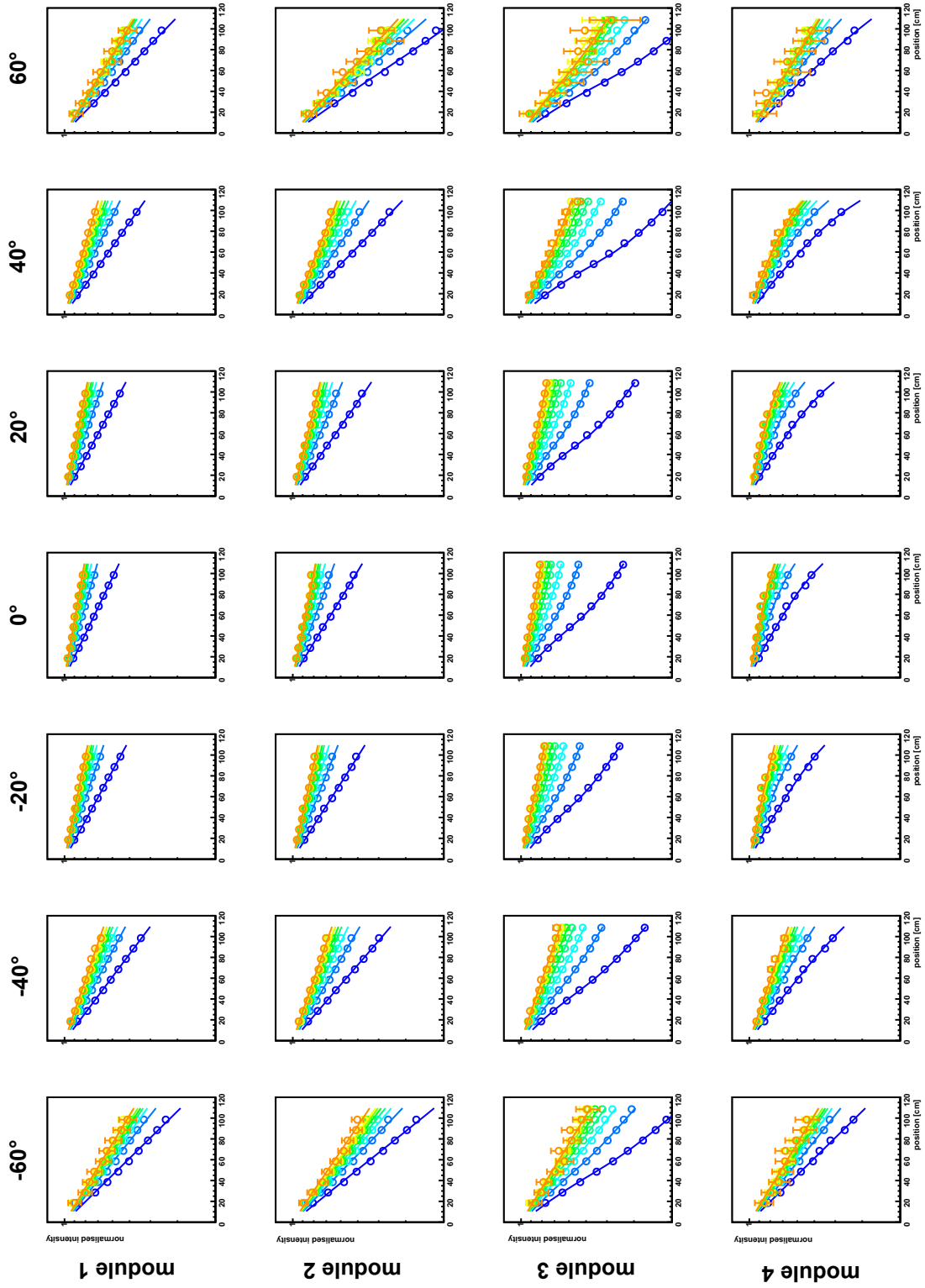


**Figure A.12:** The intensity trends and fits for the in situ irradiated modules 1 to 4 (top to bottom row). The columns show the data for  $-60^\circ$  to  $+60^\circ$  in  $20^\circ$  steps. The colors represent the wavelengths from 445 nm (blue) to 589 nm (orange).

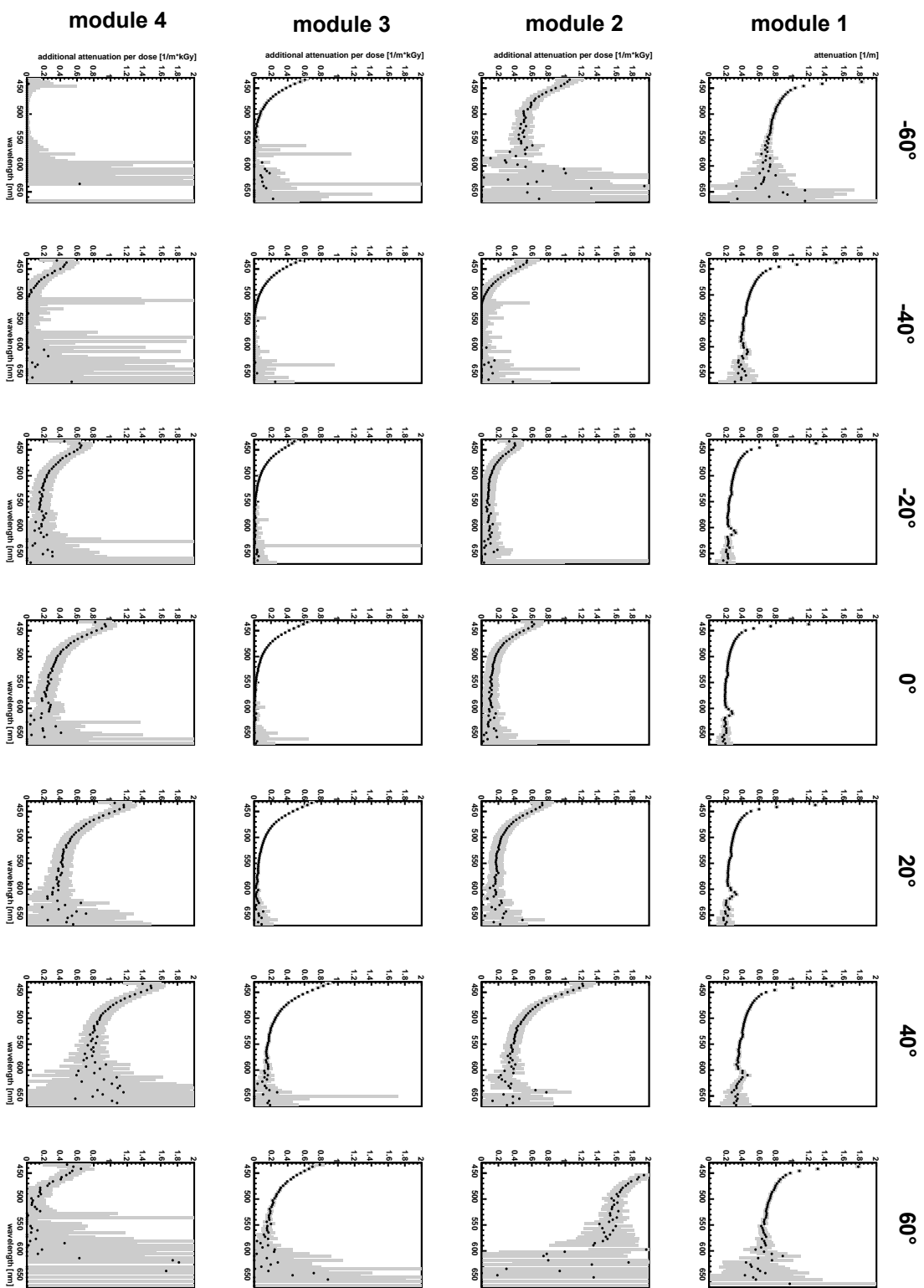


**Figure A.13:** The attenuation for the in situ irradiated modules 1 to 4 (top to bottom row). The columns show the data for  $-60^\circ$  to  $+60^\circ$  in  $20^\circ$  steps. The uncertainties are shown in grey.

## A.3 Combination of irradiation measurements

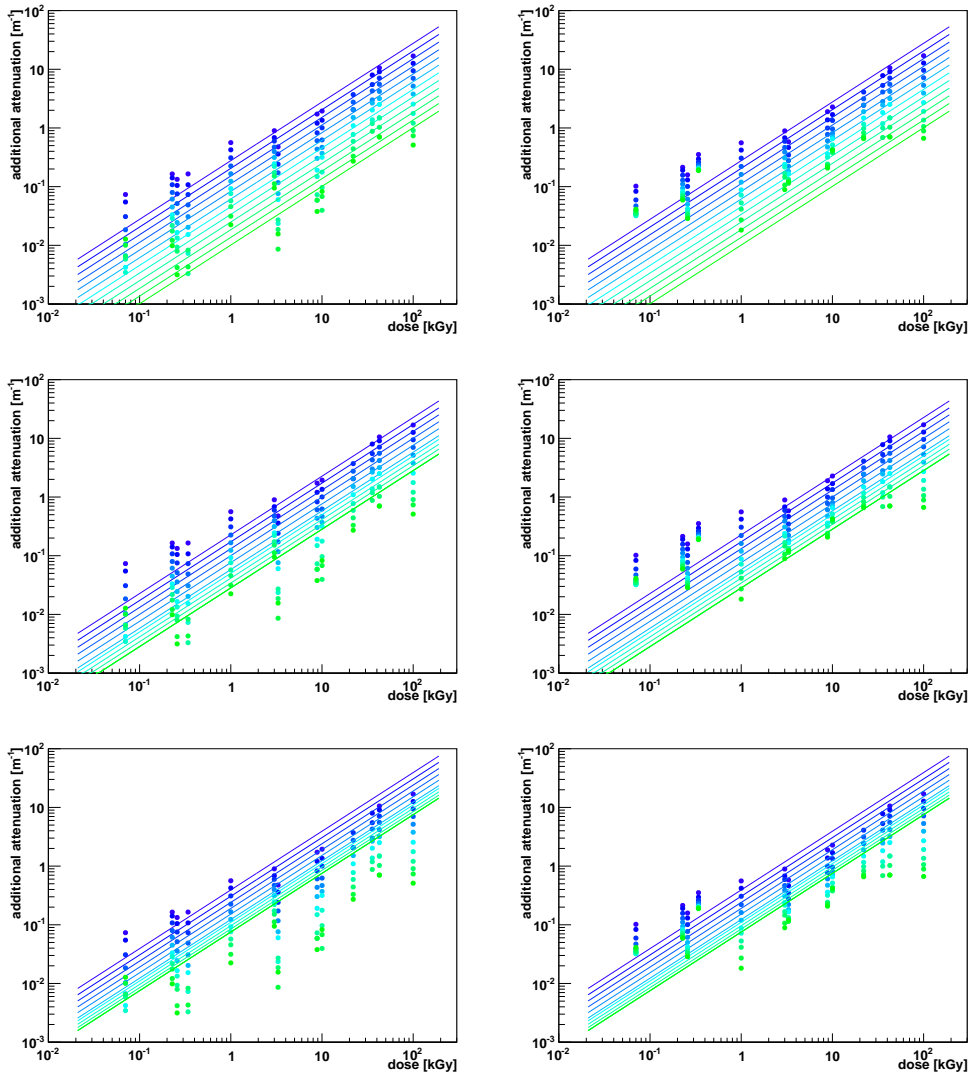


**Figure A.14:** The attenuation data (left: corrected, right: original data) compared different linear models, for different wavelengths. Top: linear model adapted to all data. Middle and bottom: Model A and B, defined in [54]. The legends are shown in Fig. 6.40 on page 115.

### A.4 Light yield maps

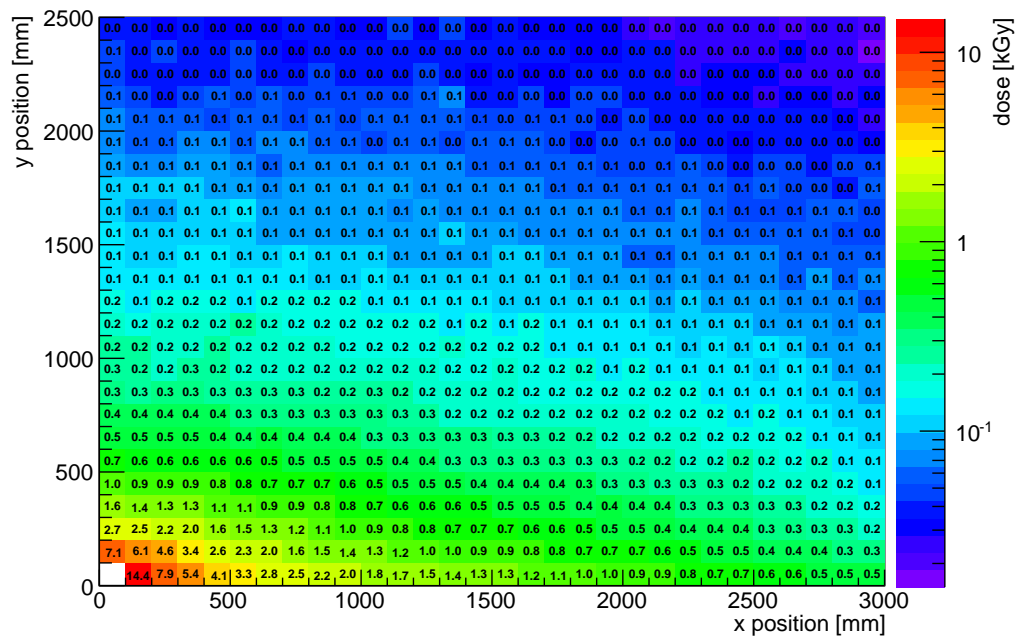


**Figure A.15:** The dose map used for the attenuation map simulation. The dose is given for an integrated luminosity of  $50 \text{ fb}^{-1}$  at the position of T1. The data was provided by [114].



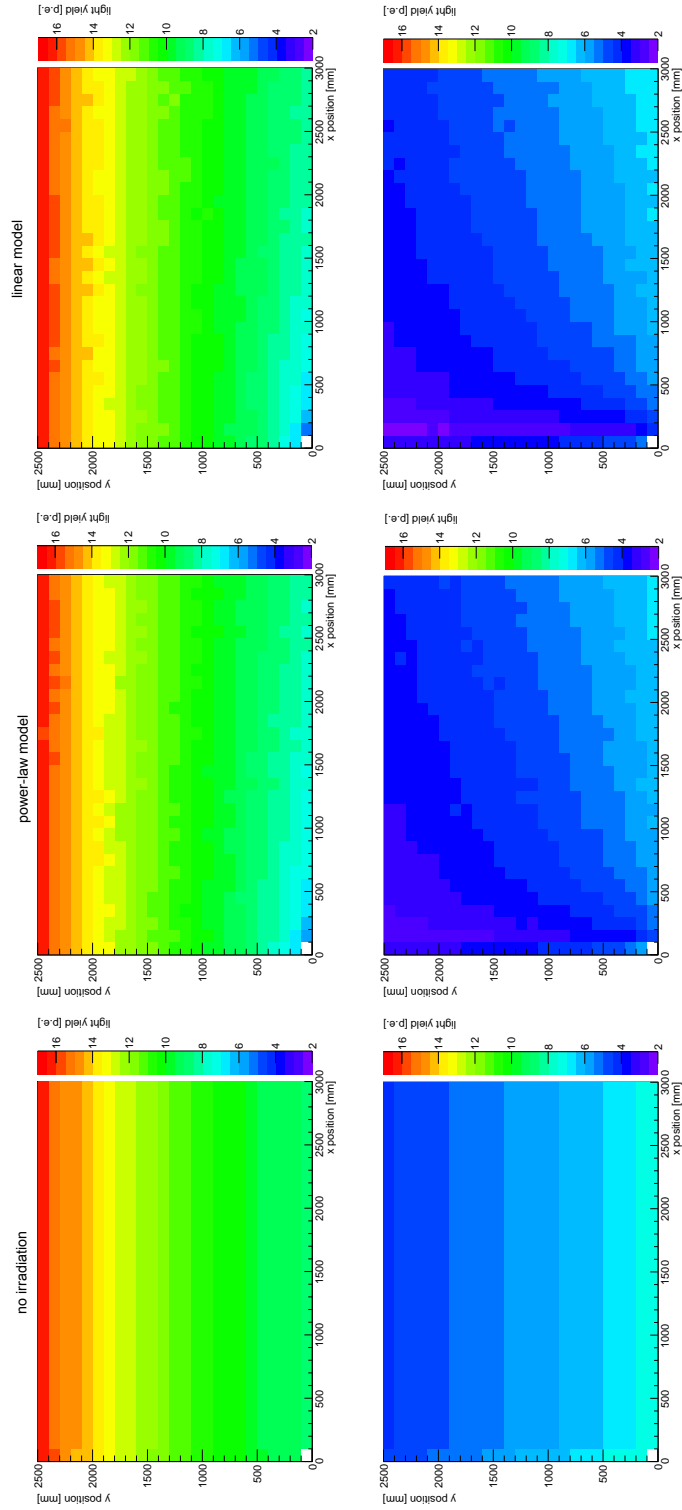


**Figure A.16:** Simulated light yields for direct light (top row) and reflected light (bottom row), for no irradiation, the power-law model and the linear model.

# A Appendix

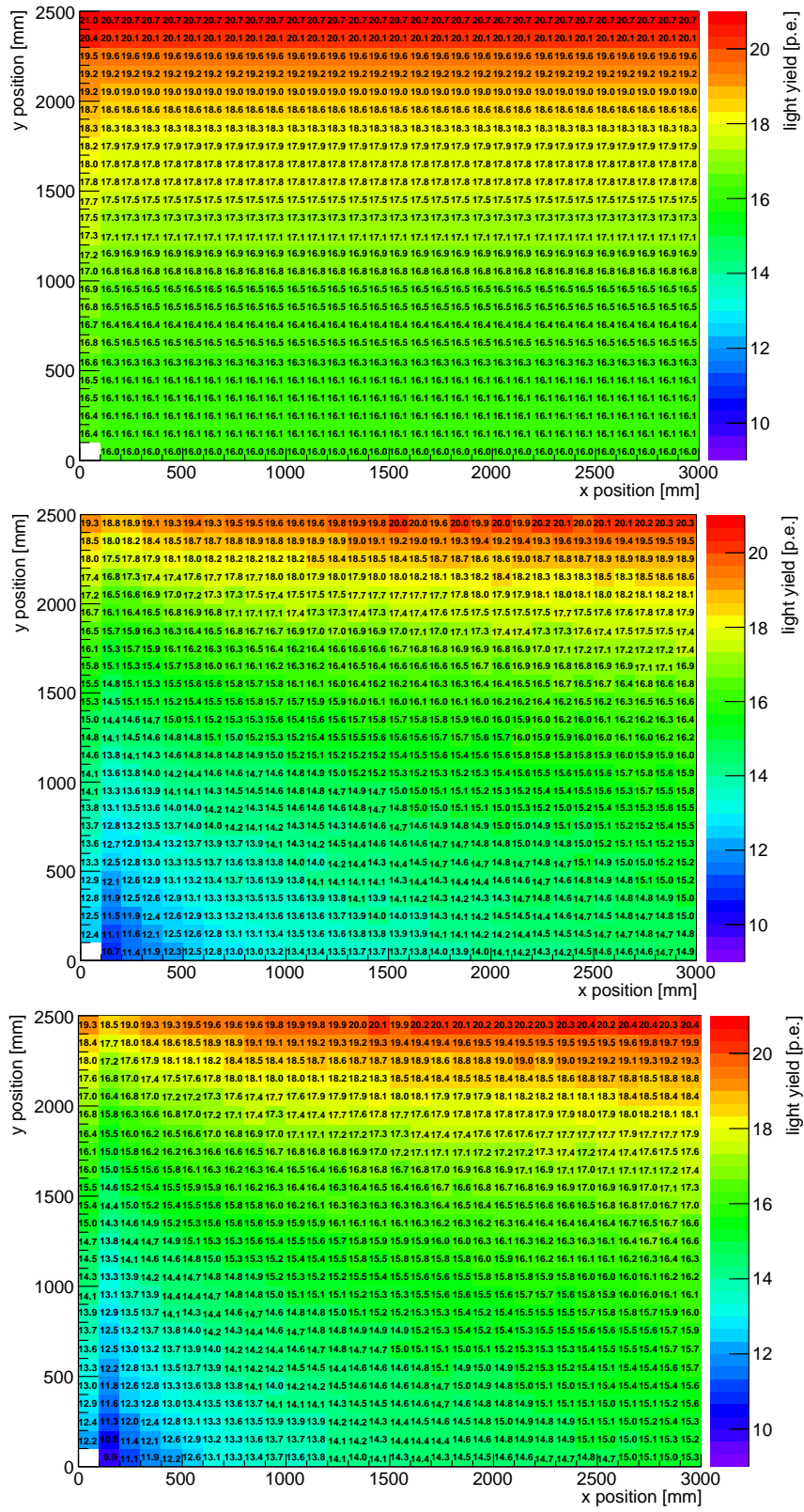


**Figure A.17:** Simulated light yields for no irradiation (top), power-law model (middle) and linear model (bottom).

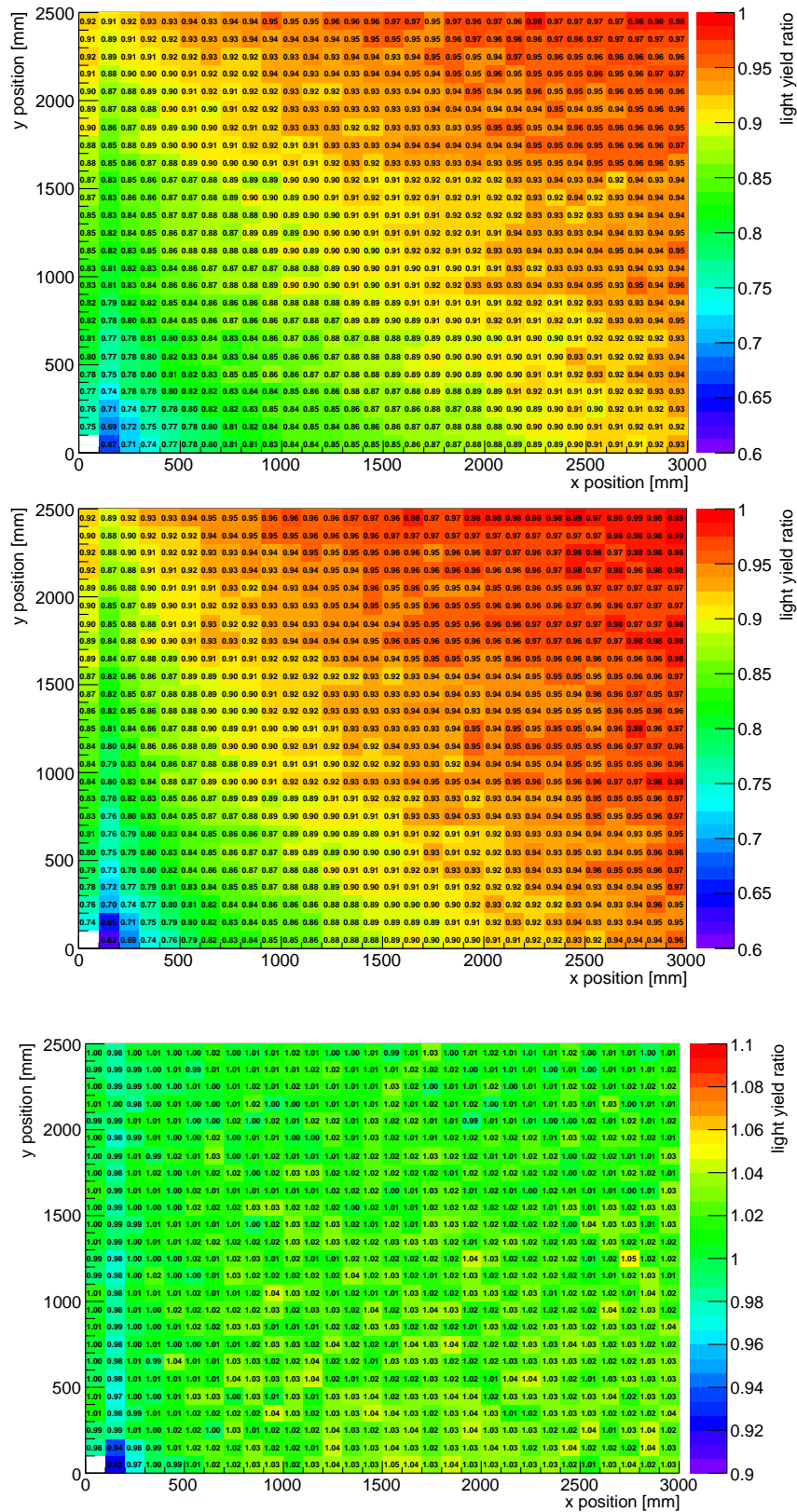


Figure A.18: Simulated ratios for the light yields of power-law model / no irradiation (top), linear model / no irradiation (middle) and linear model / power-law model (bottom).



# Bibliography

- [1] LHCb collaboration, *The LHCb Detector at the LHC*, Journal of Instrumentation **3** (2008), no. 08 S08005.
- [2] S. L. Glashow, *Partial-symmetries of weak interactions*, Nuclear Physics **22** (1961), no. 4 579 .
- [3] A. Salam and J. C. Ward, *Electromagnetic and weak interactions*, Physics Letters **13** (1964), no. 2 168 .
- [4] S. Weinberg, *A Model of Leptons*, Phys. Rev. Lett. **19** (1967) 1264.
- [5] LHCb collaboration, *LHCb Detector Performance*, Int. J. Mod. Phys. A **30** (2014) 1530022. 82 p.
- [6] LHCb collaboration, *Letter of Intent for the LHCb Upgrade*, Tech. Rep. LHCC-I-018, CERN, Geneva, Mar, 2011.
- [7] LHCb collaboration, *LHCb Tracker Upgrade Technical Design Report*, Tech. Rep. CERN-LHCC-2014-001. LHCb-TDR-015, CERN, Geneva, Feb, 2014.
- [8] S. Bachmann et al. (incl. R. Ekelhof), *LHCb Scintillating Fibre Tracker Engineering Design Review Report: Fibres, Mats and Modules*, Tech. Rep. LHCb-PUB-2015-008, CERN, Geneva, Mar, 2015.
- [9] A. Bay et al. (incl. R. Ekelhof), *Viability Assessment of a Scintillating Fibre Tracker for the LHCb Upgrade*, Tech. Rep. LHCb-PUB-2014-015, CERN, Geneva, Feb, 2014.
- [10] R. Ekelhof, *Fibers, fiber mats and panels, at LHCb Upgrade SciFi Tracker: Technology Validation Review*, CERN, 27 Nov 2013.
- [11] C. Lefevre, *LHC: the guide (English version)*, CERN-Brochure-2009-003-Eng, Feb, 2009.
- [12] R. B. Palmer and J. C. Gallardo, *High-energy colliders*, in *Critical problems in physics. Proceedings, Conference celebrating the 250th Anniversary of Princeton University, Princeton, USA, October 31-November 2, 1996*, pp. 247–269, 1997. arXiv:physics/9702016.
- [13] ATLAS collaboration, *The ATLAS Experiment at the CERN Large Hadron Collider*, Journal of Instrumentation **3** (2008), no. 08 S08003.

## Bibliography

- [14] CMS collaboration, *The CMS experiment at the CERN LHC*, Journal of Instrumentation **3** (2008), no. 08 S08004.
- [15] ATLAS collaboration, *Observation of a new particle in the search for the Standard Model Higgs boson with the ATLAS detector at the LHC*, Phys. Lett. **B716** (2012) 1.
- [16] CMS collaboration, *Observation of a new boson at a mass of 125 GeV with the CMS experiment at the LHC*, Phys. Lett. **B716** (2012) 30.
- [17] ATLAS and CMS collaborations, *Combined Measurement of the Higgs Boson Mass in  $pp$  Collisions at  $\sqrt{s} = 7$  and 8 TeV with the ATLAS and CMS Experiments*, Phys. Rev. Lett. **114** (2015) 191803.
- [18] ALICE collaboration, *The ALICE experiment at the CERN LHC*, JINST **3** (2008) S08002.
- [19] L. Evans and P. Bryant, *LHC Machine*, Journal of Instrumentation **3** (2008), no. 08 S08001.
- [20] LHCb HLT project, J. Albrecht, V. V. Gligorov, G. Raven, and S. Tolk, *Performance of the LHCb High Level Trigger in 2012*, J. Phys. Conf. Ser. **513** (2014) 012001.
- [21] *CMS detector design homepage*, 04 Sep 2015. <http://cms.web.cern.ch/news/cms-detector-design>.
- [22] LHCb Speaker's Bureau,  *$b\bar{b}$  production angle plots*, April, 2015. [http://lhcb.web.cern.ch/lhcb/speakersbureau/html/bb\\_ProductionAngles.html](http://lhcb.web.cern.ch/lhcb/speakersbureau/html/bb_ProductionAngles.html).
- [23] A. Schopper, *PH Newsletter - The LHCb Upgrade*, 16 May 2014.
- [24] T. Ruf, *Web Page of a Panoramix User*, Sep, 2015. [http://lhcb-reconstruction.web.cern.ch/lhcb-reconstruction/panoramix/running\\_panoramix.htm](http://lhcb-reconstruction.web.cern.ch/lhcb-reconstruction/panoramix/running_panoramix.htm).
- [25] LHCb Speaker's Bureau, *LHCb Trigger Schemes*, Sep, 2015. <https://lhcb.web.cern.ch/lhcb/speakersbureau/html/TriggerScheme.html>.
- [26] LHCb collaboration, *Observation of  $J/\psi p$  resonances consistent with pentaquark states in  $\Lambda_b^0 \rightarrow J/\psi K^- p$  decays*, Phys. Rev. Lett. **115** (2015) 072001.
- [27] LHCb collaboration, *A measurement of the CKM angle  $\gamma$  from a combination of  $B^\pm \rightarrow Dh^\pm$  analyses*, Phys. Rev. Lett. **B726** (2013) 151.
- [28] C. Cauet, *Precision measurement of the CKM parameter  $\sin(2\beta)$  with the LHCb experiment*, Aug, 2015. PhD thesis, Technische Universität Dortmund.
- [29] LHCb collaboration, *First Evidence for the Decay  $B_s^0 \rightarrow \mu^+ \mu^-$* , Phys. Rev. Lett. **110** (2013), no. 2 021801.
- [30] CMS and LHCb collaborations, *Observation of the rare  $B_s^0 \rightarrow \mu^+ \mu^-$  decay from the combined analysis of CMS and LHCb data*, Nature **522** (2015) 68.

- [31] Belle-II collaboration, *Belle II Technical Design Report*, arXiv:1011.0352, KEK-REPORT-2010-1, 2010.
- [32] M. Barrett, *The Belle II Experiment*, May, 2015. Proceedings of talk presented at: Flavor Physics & CP Violation, Nagoya, Japan.
- [33] U. Uwer, *Future facilities*, 2014. Flavour Physics Conference, ICISE, Quy Nhon.
- [34] LHCb collaboration, *LHCb Trigger and Online Upgrade Technical Design Report*, Tech. Rep. CERN-LHCC-2014-016. LHCb-TDR-016, CERN, Geneva, May, 2014.
- [35] LHCb collaboration, *LHCb VELO Upgrade Technical Design Report*, Tech. Rep. CERN-LHCC-2013-021. LHCb-TDR-013, CERN, Geneva, Nov, 2013.
- [36] LHCb collaboration, *LHCb PID Upgrade Technical Design Report*, Tech. Rep. CERN-LHCC-2013-022. LHCb-TDR-014, CERN, Geneva, Nov, 2013.
- [37] LHCb Outer Tracker group, *Performance of the LHCb Outer Tracker*, J. Instrum. **9** (2013) P01002. 30 p.
- [38] LHCb collaboration, *LHCb inner tracker: Technical Design Report*. CERN-LHCC-2002-029; LHCb-TDR-8, CERN, Geneva, 2002.
- [39] CMS collaboration, *The CMS tracker: addendum to the Technical Design Report*, CERN, Geneva, 2000.
- [40] CMS collaboration, *CMS Technical Design Report for the Pixel Detector Upgrade*, Tech. Rep. CERN-LHCC-2012-016. CMS-TDR-11, CERN, Geneva, Sep, 2012.
- [41] LHCb collaboration, LHCb collaboration, *Expression of Interest for an LHCb Upgrade*, Tech. Rep. LHCC-G-139. CERN-LHCC-2008-007, CERN, Geneva, Apr, 2008.
- [42] F. Muheim, *R&D plans for all subsystems, LHCb Upgrade working group meeting*, CERN, 05 Aug 2008.
- [43] T. Nakada, *Thin Fiber Tracking, Upgrade meeting, LHCb Week*, CERN, 26 Feb 2009.
- [44] F. Blanc, *Fiber Tracking, LHCb Upgrade Meeting*, CERN, 12 May 2010.
- [45] R. Ekelhof and M. Deckenhoff, *Fiber Tracker Studies for OT, Sub-Detector Sessions, LHCb week*, CERN, 27 Feb 2010.
- [46] *LHCb Upgrade Mini-Workshop on tracker*, CERN, 15 Sep 2011.
- [47] LHCb collaboration, *Framework TDR for the LHCb Upgrade: Technical Design Report*, Tech. Rep. CERN-LHCC-2012-007. LHCb-TDR-12, CERN, Geneva, Apr, 2012.
- [48] *LHCb Upgrade SciFi Tracker: Technology Validation Review*, CERN, 27 Nov 2013.

## Bibliography

- [49] B. Leverington, *The LHCb upgrade and the Scintillating Fibre Tracker*, in *European Physical Society HEP*, 2015.
- [50] Kuraray Co. , Ltd. , *Kuraray - plastic scintillating fibers homepage*, Feb, 2016. <http://kuraraypsf.jp/psf/index.html>.
- [51] D. Renker, *Geiger-mode avalanche photodiodes, history, properties and problems*, Nuclear Instruments and Methods in Physics Research Section A: Accelerators, Spectrometers, Detectors and Associated Equipment **567** (2006), no. 1 48 .
- [52] Hamamatsu Photonics, *MPPC -Multi-Pixel Photon Counter -Technical Information*, 2009. [http://sales.hamamatsu.com/assets/applications/SSD/mppc\\_kapd9003e01\\_1.pdf](http://sales.hamamatsu.com/assets/applications/SSD/mppc_kapd9003e01_1.pdf).
- [53] A. Kuonen, *SiPM PDE, private communication*, Apr, 2015.
- [54] M. Deckenhoff, *Scintillating Fibre and Silicon Photomultiplier Studies for the LHCb Upgrade*, 2015. PhD thesis, Technische Universität Dortmund.
- [55] H. Channal, *Electronics Status, SciFi General Meeting*, CERN, 07 Mar 2016.
- [56] C. Joram and T. Schneider, *Mirroring of fibre ends for the LHCb SciFi project*, Tech. Rep. LHCb-PUB-2014-020, CERN, Geneva, Feb, 2014.
- [57] A. Schultz von Dratzig, *Finite Element Analysis of the SciFi-Nomex-Sandwich Panels*, Tech. Rep. LHCb-PUB-2015-007, CERN, Geneva, Mar, 2015.
- [58] A. Pellegrino, *Readout box status, SciFi General Meeting*, CERN, 26 Mar 2015.
- [59] C. Joram, *SciFi Tracker Planning twiki page*, Mar, 2016. <https://twiki.cern.ch/twiki/bin/view/LHCb/SciFiTrackerPlanning>.
- [60] R. Greim, *LHCb SciFi Testbeam 2015, LHCb SciFi test beam meeting*, CERN, 09 Sep 2015.
- [61] A. B. Rodrigues Cavalcante et al. (incl. R. Ekelhof), *LHCb Scintillating Fibre Tracker: Test Beam Report 2015*, Tech. Rep. LHCb-PUB-2015-025, CERN, Geneva, Nov, 2015.
- [62] S. Bachmann et al. (incl. R. Ekelhof). *Tracker infrastructure workshop*, Imperial College, London, 21 Feb 2013.
- [63] M. Hoeck, *Design and Construction of a Scintillating Fibre Tracker for measuring Hard Exclusive Reactions at HERMES*, 2006. 10.3204/DESY-THESIS-2006-027.
- [64] T. Savidge, *Commercial techniques, meeting dedicated to fiber module production*, RWTH Aachen, 24 Sep 2012.
- [65] A. B. Rodrigues Cavalcante et al. (incl. R. Ekelhof), *Scanners for the quality control of scintillating plastic fibres*, Tech. Rep. LHCb-PUB-2015-009, CERN, Geneva, Apr, 2015.



- [66] M. Deckenhoff, *Entwicklung einer Qualitätsanalyse für szintillierende Fasern - Untersuchungen zur Datennahme des SiPM-Moduls, Messverfahren und Datenanalyse zur Bestimmung von Faserparametern, automatisierte Regelung der Faserspaltung*, 2009. Diploma thesis, Technische Universität Dortmund.
- [67] F. Kruse, *Entwicklung einer Qualitätsanalyse für szintillierende Fasern - Geant4-Simulationen, Entwicklung der Datennahme, Messungen an szintillierenden Fasern*, 2009. Diploma thesis, Technische Universität Dortmund.
- [68] B. Beischer *et al.*, *A high-resolution scintillating fiber tracker with silicon photomultiplier array readout*, Nuclear Instruments and Methods in Physics Research Section A: Accelerators, Spectrometers, Detectors and Associated Equipment **622** (2010), no. 3 542 .
- [69] G. Roper Yearwood, *The Development of a High-Resolution Scintillating Fiber Tracker with Silicon Photomultiplier Readout*, 2013. PhD thesis.
- [70] P. Annis *et al.*, *The {CHORUS} scintillating fiber tracker and opto-electronic readout system*, Nuclear Instruments and Methods in Physics Research Section A: Accelerators, Spectrometers, Detectors and Associated Equipment **412** (1998), no. 1 19 .
- [71] T. Nakano *et al.*, *Research and development of scintillating fiber tracker for  $\nu$ /<sub>sub mu</sub> /-  $\nu$ /<sub>sub tau</sub> / oscillation experiment*, in *Nuclear Science Symposium and Medical Imaging Conference, Conference Record of the 1991 IEEE*, pp. 264–268 vol.1, Nov, 1991.
- [72] R. Ekelhof, *SciFi Module R&D, LHCb SciFi Upgrade Tracker Meeting*, CERN, 14 Jun 2012.
- [73] C. Joram, *Coverlay fibre mat cross section photograph, private communication*, Nov, 2015.
- [74] M. Domke, *Drawing of alignment pin, private communication*, 2015.
- [75] E. Korovaytseva, P. Hebler, and R. Ekelhof, *Simulation of Fibre Mat Winding for the LHCb SciFi Tracker*, Tech. Rep. LHCb-INT-2014-023, CERN, Geneva, Apr, 2014.
- [76] J. Müller, *Entwicklung einer Qualitätskontrolle von Matten aus szintillierenden Fasern für den LHCb SciFi Tracker*, 2014. Master's thesis, Technische Universität Dortmund.
- [77] R. Ekelhof, *Winding Machine Requirements - Fibre Mat Production Machine for the SciFi Tracker of LHCb*, Tech. Rep. LHCb-INT-2014-031, CERN, Geneva, Jul, 2014.
- [78] J. Müller and P. Zander, *Online Monitoring of Fibre Mat Winding*, Tech. Rep. LHCb-INT-2015-014, CERN, Geneva, May, 2015.

## Bibliography

- [79] S. Brandt, *Qualitätsanalyse von Tracker-Modulen aus szintillierenden Fasern für das Upgrade des LHCb-Detektors am CERN*, 2012. Bachelor's thesis, Technische Universität Dortmund.
- [80] F. D. Brooks, *Development of organic scintillators*, 1979. doi: 10.1016/0029-554X(79)90729-8.
- [81] H. Leutz, *Scintillating fibres*, Nuclear Instruments and Methods in Physics Research Section A: Accelerators, Spectrometers, Detectors and Associated Equipment **364** (1995), no. 3 422 .
- [82] T. Förster, *Zwischenmolekulare energiewanderung und fluoreszenz*, Ann. Phys. **437** (1948) 55.
- [83] I. A. Berlman, *Handbook of Fluorescence Spectra of Aromatic Molecules*, Academic Press, New York and London, 2. ed., 1971.
- [84] C. D'Ambrosio *et al.*, *Organic scintillators with large Stokes shifts dissolved in polystyrene*, Nucl. Instrum. Meth. **A307** (1991) 430 .
- [85] C. Ponomarenko *et al.*, *Nanostructured organosilicon luminophores and their application in highly efficient plastic scintillators*, Nature Scientific Reports **4** (2014) .
- [86] C. Joram, G. Haefeli, and B. Leverington, *Scintillating fibre tracking at high luminosity colliders*, Journal of Instrumentation **10** (2015), no. 08 C08005.
- [87] T. O. White, *Scintillating fibres*, Nuclear Instruments and Methods in Physics Research Section A: Accelerators, Spectrometers, Detectors and Associated Equipment **273** (1988), no. 2 820 .
- [88] P. Rebourgeard *et al.*, *Fabrication and measurements of plastic scintillating fibers*, Nuclear Instruments and Methods in Physics Research Section A: Accelerators, Spectrometers, Detectors and Associated Equipment **427** (1999), no. 3 543 .
- [89] J. S. Wallace, M. B. Sinclair, K. T. Gillen, and R. L. Clough, *Color center annealing in  $\gamma$ -irradiated polystyrene, under vacuum and air atmospheres*, Radiation Physics and Chemistry **41** (1993), no. 1-2 85 .
- [90] J. Bähr, R. Nahnauer, S. Nerreter, and R. Shanidze, *A Fiber Detector Radiation Hardness Test*, 1999. <http://arxiv.org/abs/physics/9907019v1>.
- [91] A. D. Bross and A. Pla-Dalmau, *Radiation Damage of Plastic Scintillators*, 1991. <http://lss.fnal.gov/archive/1991/pub/Pub-91-308.pdf>.
- [92] W. Busjan, K. Wick, and T. Zoufal, *Shortlived absorption centers in plastic scintillators and their influence on the fluorescence light yield*, Nuclear Instruments and Methods in Physics Research Section B: Beam Interactions with Materials and Atoms **152** (1999), no. 1 89 .
- [93] H. Kudoh *et al.*, *Pulsed e-beam irradiation of polymers - A comparison of dose rate effects and let effects*, Radiation Physics and Chemistry **48** (1996), no. 5 555 .

- [94] K. Wick and T. Zoufal, *Unexpected behaviour of polystyrene-based scintillating fibers during irradiation at low doses and low dose rates*, Nuclear Instruments and Methods in Physics Research Section B: Beam Interactions with Materials and Atoms **185** (2001), no. 1-4 341 .
- [95] T. Zoufal, *Beeinträchtigung der optischen Eigenschaften und Veränderung der Fluoreszenz von Kunststoffszintillatoren durch Röntgenstrahlung*, PhD thesis, Universität Hamburg, 2002, doi: 10.3204/DESY-THESIS-2002-013.
- [96] J. Blaha *et al.*, *Scintillating fibers for particle physics experiments - on-line-induced absorption measurements in gamma radiation field*, Radiation Measurements **38** (2004), no. 4-6 805 .
- [97] C. Joram, *LHCb SciFi Fibre Inventory twiki page*, 2015. <https://twiki.cern.ch/twiki/bin/view/LHCb/FiberInventory>.
- [98] A.-K. Raytarowski, *Untersuchungen zum Durchmesser Verlauf szintillierender Fasern mithilfe einer automatisierten Faserkontrolle im Rahmen des LHCb Upgrades*, 2014. Bachelor's thesis, Technische Universität Dortmund.
- [99] GEANT4, S. Agostinelli *et al.*, *GEANT4: A Simulation toolkit*, Nucl. Instrum. Meth. **A506** (2003) 250.
- [100] Hamamatsu, *Mini-spectrometer C10083CA homepage*, March, 2016. <http://www.hamamatsu.com/us/en/C10083CA.html>.
- [101] T. Soestwöhner, *Messung der Winkelabhängigkeit des Photonenaustritts am Ende von szintillierenden Fasern für den LHCb-SciFi-Tracker*, 2014. Bachelor's thesis, Technische Universität Dortmund.
- [102] J. Broll, *Simulation der Winkelverteilung der austretenden Photonen am Ende von szintillierenden Fasern für den SciFi-Tracker des LHCb-Experiments*, 2014. Bachelor's thesis, Technische Universität Dortmund.
- [103] J. Albrecht *et al.* (incl. R. Ekelhof), *Angular dependency of the photons emitted by scintillating fibres*, Tech. Rep. LHCb-INT-2016-002, CERN, Geneva, Jan, 2016.
- [104] T. Soestwöhner and J. Broll, *Fibre simulation data, private communication*, 2014.
- [105] S. Jäger, *Untersuchung der Winkelabhängigkeit der Abschwächlänge bei szintillierenden Fasern*, 2015. Bachelor's thesis, Technische Universität Dortmund.
- [106] J. Surmann, *Simulationsstudien zur Winkelabhängigkeit von Abschwächlängen szintillierender Fasern für das Tracker-Upgrade am LHCb-Experiment*, 2015. Bachelor's thesis, Technische Universität Dortmund.
- [107] J. Surmann and R. Ekelhof, *Simulating the Properties of Scintillating Fibres - The influence of angles and track lengths of photons on the absorption*, Tech. Rep. LHCb-INT-2016-009, CERN, Geneva, Feb, 2016.
- [108] M. Karacson, *Dose simulation data at the LHCb shielding wall, private communication*, 2013.

## Bibliography

- [109] L. Gavardi, *Fibre attenuation measurement data, private communication*, 2015.
- [110] C. Joram, *Fibre Procurement and QA, SciFi General Meeting*, CERN, 01 Dec 2014.
- [111] C. Joram, *Fibre attenuation measurement data, private communication*, 2015.
- [112] B. Leverington, *Fibre attenuation measurement data, private communication*, 2015.
- [113] M. Demmer, R. J. Ekelhof, and J. T. Wishahi, *Simulation of Light Yield Attenuation Maps for the LHCb SciFi Tracker Upgrade*, Tech. Rep. LHCb-INT-2016-015, CERN, Geneva, Mar, 2016.
- [114] N. Lopez March, *Dose simulation data for the SciFi Tracker, private communication*, 2013.
- [115] M. Karacson, *Dose simulation, private communication*, 2016.
- [116] M. Demmer, *Simulated attenuation map data, private communication*, 2016.
- [117] National Nuclear Data Center, *NNDC homepage*, 2016. <http://www.nndc.bnl.gov/about/nndc.html>.

# List of Figures

2.1	The CERN accelerator complex . . . . .	7
2.2	Cross-section of an LHC dipole magnet . . . . .	8
2.3	Luminosity trend during a fill . . . . .	9
2.4	The CMS detector . . . . .	10
2.5	$b\bar{b}$ production . . . . .	11
2.6	The LHCb detector, 3D . . . . .	11
3.1	The LHCb detector, side view . . . . .	13
3.2	LHCb IT-OT schematic . . . . .	15
3.3	LHCb RICH 1 rings . . . . .	16
3.4	LHCb Trigger Scheme 2012 . . . . .	17
3.5	Instantaneous luminosity and pile-up at LHCb . . . . .	18
3.6	Integrated luminosity at LHCb . . . . .	18
3.7	Trigger yield as a function of the instantaneous luminosity . . . . .	20
3.8	LHCb Trigger Scheme Upgrade . . . . .	21
3.9	LHCb Trigger Scheme online-offline comparison . . . . .	21
3.10	The upgraded LHCb detector . . . . .	22
3.11	VELO schematic layout . . . . .	22
3.12	UT stave structure . . . . .	23
3.13	RICH1 optics . . . . .	24
4.1	LHCb track types . . . . .	26
4.2	LHCb tracking momentum distribution and momentum resolution . . . . .	27
4.3	LHCb reconstructed tracks . . . . .	28
4.4	Tracking Station options . . . . .	31
4.5	SciFi station . . . . .	32
4.6	SciFi cluster principle . . . . .	33
4.7	Dose simulation at T1 . . . . .	34
4.8	Fired pixels of an SiPM as function of entering photons . . . . .	36
4.9	Photon detection efficiency of an SiPM . . . . .	36
4.10	Noise cluster rate as a function of the cross-talk and the seed threshold . . . . .	37
4.11	Photograph of an 128-channel SiPM . . . . .	38
4.12	Scheme of the read-out electronics . . . . .	38
4.13	Scheme of the read-out ASIC PACIFIC . . . . .	39
4.14	Time dependent output of the integrator . . . . .	39
4.15	Sketch of the fibre winding wheel . . . . .	41

*List of Figures*

4.16	Pin insert in the winding wheel . . . . .	41
4.17	Boundary between two fibre mats in a module . . . . .	42
4.18	Schematic of the panels . . . . .	43
4.19	Simulation of the deformation of a module through its own weight . . . . .	44
4.20	Cross section of a read-out box . . . . .	45
4.21	Bridge and table of the T-Stations . . . . .	46
4.22	Test beam light yield distribution . . . . .	49
4.23	Test beam single-hit efficiency . . . . .	50
4.24	Test beam single-hit efficiency vs light yield . . . . .	51
5.1	Schematic of module end cuts alternatives . . . . .	54
5.2	Fibre winding machine based on a rotating frame . . . . .	56
5.3	Fibre winding for CHORUS . . . . .	56
5.4	Hand winding at CERN . . . . .	57
5.5	Cross section of a hand wound 2.5 m fibre mat . . . . .	57
5.6	Fibre mat winding on a Coverlay patterned Kapton foil . . . . .	59
5.7	Coverlay fibre mat cross section . . . . .	59
5.8	Fibre guiding clamp on the wheel . . . . .	60
5.9	Different shaped pin holes in the small wheel . . . . .	62
5.10	Drawings of the final alignment pin-hole shape . . . . .	62
5.11	Fibre mat cross section simulation . . . . .	63
5.12	Fibre mat bump cut out . . . . .	64
5.13	Prototype winding machine . . . . .	65
5.14	Prototype winding machine positioning spool . . . . .	66
5.15	Serial winding machine . . . . .	67
5.16	Positioning spool serial winding machine . . . . .	68
5.17	Serial winding machine control PC . . . . .	68
5.18	Online monitoring screenshot . . . . .	70
5.19	Coverlay winding . . . . .	70
5.20	Online monitoring camera at the serial winding machine . . . . .	71
5.21	Fibre mat cross section with pattern . . . . .	72
5.22	Fibre mat cross section with slit . . . . .	72
6.1	Absorption and emission spectrum of scintillating fibre compounds . . . . .	76
6.2	Scintillating fibre spectrum . . . . .	77
6.3	Scintillating scheme of NOL fibres . . . . .	78
6.4	Fibre scheme . . . . .	79
6.5	Attenuation coefficients in scintillating fibres . . . . .	79
6.6	The extension of a scintillating fibre under different forces . . . . .	82
6.7	The contraction of a fibre mat right after the vertical cut . . . . .	82
6.8	Fibre bump . . . . .	83
6.9	Fibre diameter trend . . . . .	84
6.10	Fibre diameter distribution 2d . . . . .	84
6.11	Fibre diameter histogram . . . . .	85

6.12	Setup to measure a single fibre with a spectrometer . . . . .	87
6.13	Attenuation fit of 12 meter long fibre . . . . .	88
6.14	Spectral attenuation of a scintillating fibre . . . . .	88
6.15	Setup to measure the angular intensity of a single fibre with a spectrometer	90
6.16	Angular intensity for photons leaving the fibre end . . . . .	91
6.17	Angular intensity for photons leaving the fibre end without reflections at the surface . . . . .	91
6.18	Angular intensity for photons leaving the fibre end, including reflection losses . . . . .	92
6.19	Angular attenuation measurements . . . . .	93
6.20	Contributions to the angular attenuation . . . . .	93
6.21	Relative photon path lengths in core and cladding . . . . .	94
6.22	Relative photon path lengths to excitation distance . . . . .	94
6.23	Attenuation for different exit angles and sections of the fibre . . . . .	95
6.24	Attenuation for different angles split up for attenuation factors . . . . .	96
6.25	Setup to measure the angular intensity of the fibres irradiated in Garching	98
6.26	Intensity trend fibres irradiated in Garching, 0° . . . . .	100
6.27	Intensity trend fibres irradiated in Garching, 30° . . . . .	100
6.28	Attenuation of the fibres irradiated in Garching . . . . .	101
6.29	Position of the fibre modules installed in situ . . . . .	102
6.30	Integrated dose for the fibres irradiated in situ . . . . .	103
6.31	Setup to measure the attenuation of the fibres irradiated in situ . . . . .	103
6.32	Radioactive source positioned on the alignment tool of the fibres irradiated in situ . . . . .	104
6.33	Intensity trends of in situ irradiated fibres measured with an SiPM . . . . .	105
6.34	Attenuation of in situ irradiated fibres measured with an SiPM. . . . .	106
6.35	Setup to measure the angular intensity of the fibres irradiated in situ . . . . .	107
6.36	in situ intensity correction . . . . .	109
6.37	Intensity trend of module 1 and 3 . . . . .	110
6.38	Attenuation per dose of in situ irradiated modules . . . . .	111
6.39	Attenuation of in situ irradiated modules . . . . .	112
6.40	Additional attenuation as a function of the dose . . . . .	115
6.41	Additional attenuation as a function of the wavelength . . . . .	116
6.42	Corrected attenuation . . . . .	116
6.43	Attenuation per dose as a function of the dose and the dose rate . . . . .	117
6.44	Attenuation at 450 nm . . . . .	118
6.45	Attenuation data compared to the power-law model . . . . .	119
6.46	Attenuation data compared to the linear model . . . . .	120
6.47	Dose map used for the attenuation map simulation . . . . .	121
6.48	Simulated light yields . . . . .	122
6.49	Simulated ratios of the light yields . . . . .	124
A.1	Cross section of the fibre bundle irradiated with protons . . . . .	vii

*List of Figures*

A.2	Photograph of absorber at the beam line exit window at the Tandem accelerator at Forschungszentrum Garching. . . . .	vii
A.3	Photograph of the linear slide to move the fibre modules at Forschungszentrum Garching. . . . .	viii
A.4	Photograph of the angular measurement setup for the proton irradiated fibres	viii
A.5	Cross section of a fibre bundle irradiated in situ . . . . .	ix
A.6	Photograph of the fibre modules installed in situ . . . . .	x
A.7	Photograph of an in situ fibre module read out during a Technical Stop . .	x
A.8	Intensity trends for in situ module 1 . . . . .	xi
A.9	Intensity trends for in situ module 2 . . . . .	xii
A.10	Intensity trends for in situ module 3 . . . . .	xiii
A.11	Intensity trends for in situ module 4 . . . . .	xiv
A.12	Intensity trends with fits for in situ irradiated modules . . . . .	xv
A.13	Attenuation of the in situ modules . . . . .	xvi
A.14	Attenuation data compared to different linear models . . . . .	xvii
A.15	Dose map used for the attenuation map simulation . . . . .	xviii
A.16	Simulated light yields for direct and reflected light . . . . .	xix
A.17	Simulated light yields . . . . .	xx
A.18	Simulated ratios of the light yields . . . . .	xxi



# Acknowledgments

The work presented in this thesis could not have been possible without the collaboration of many colleagues. Above all, I want to express my gratitude to Mirco Deckenhoff, Janine Müller, and Julian Wishahi from the Dortmund group. We spent many years together, travelling across Europe irradiating things, interpreting results, winding fibre mats and discussing simulations.

Since they joined the LHCb SciFi group, I had a very fruitful collaboration with Blake Leverington and Christian Joram. Without the discussions about fibre irradiations and module design, the results presented in this document would not have been the same. In addition I want to thank them and Laura Gavardi for providing the results of their own irradiation campaigns, which I used to develop the attenuation dependent models.

I would like to thank Moritz Demmer, Julian Surmann and Carina Fedojevic of the Dortmund SciFi group for their work and help with simulations and measurements for this thesis. In addition I don't want to forget the other (former) members of the Dortmund SciFi group Tobias, Stefan, Florian, Philip, Holger and Nina and the Bachelor students Svenja, Sebastian, Raphael, Carina, David, Jessica, Anna-Katharina, Jan, Thomas, Max, Ole, Sebastian, Julian, Martin, Patrick, and two Simons.

The work presented in this document could not have been achieved without the technical support and work by many people. I want to thank Matthias Domke, Kai Warda and Georg Kosian, the mechanical workshop and the electronic workshop, Klaus Rudloff and his team of the design office, and the Präparationslabor.

My research on the fibre mat production and the study of the radiation damage profited strongly from the collaboration with other groups. I would like to thank the teams from RWTH Aachen (Gregorio, Roman, Carsten, Tobias, Simon, Michael, and Thomas), University of Heidelberg (Blake, Sebastian, Uli, Christian, Max, and Stephie), CERN (Christian, Ana-Barbara, and Thomas), EPFL from Lausanne (Fred, Guido, Tim, Axel, Mark, Barinjaka, and Plamen) and NIKHEF from Amsterdam (Antonio and Jacco). In addition, I would like to thank the management of the LHCb SciFi group, namely Fred Blanc, Ulrich Uwer and Christian Joram for their support.

In the context of the irradiation of fibres in the LHCb cavern, I would like to express my gratitude to Eric, Rolf, Gloria, Matthias, Yuri, Niels, Antonio, and Moritz<sup>†</sup>. For the proton irradiation I thank the team of the tandem accelerator at Forschungszentrum Garching and Christoph Ilgner.

## *Acknowledgements*

I would like to thank Bernhard, Christophe, Florian, Janine, Johannes, Julian, Max, Steffi and everyone I forgot who helped me to write down the words, sample reading chapters and answering questions about style and wording.

I am grateful for the support by the Bundesministerium für Bildung und Forschung, allowing me to perform my research and to travel to meet collaborators in person. I would like to thank Priv.-Doz. Dr. Reiner Klingenberg for reviewing my thesis and Prof. Dr. Gudrun Hiller and Dr. Bärbel Siegmann for accepting to participate in my board of examiners. Last but not least I want to express my deep gratitude to my advisor, Prof. Dr. Bernhard Spaan. He gave me the freedom to follow my own ideas and gave me support when necessary.

# Danksagung

Nach dem offiziellen Teil, möchte ich nun noch den Menschen danken, welche zwar nicht direkt zum Inhalt der Arbeit beigetragen haben, aber trotzdem einen Anteil am Gelingen hatten.

Hier muss die gesamte Arbeitsgruppe E5a genannt werden. Ich komme (fast) jeden Tag gerne ins Büro – das wäre ohne die Kollegen sicherlich nicht der Fall. Am wichtigsten sind hierbei natürlich die zahlreichen Zimmergenossen, aber auch viele andere haben zum guten Klima während und abseits der Arbeit beigetragen. Ob bei Gesprächen über Essen und Kamas, dem gemeinsamen Mittagessen mit 30 Personen oder dem einheitlichen Jammern auf dem Fahrrad auf der „schönsten Route“ zu le Big Boss.

Ohne die stets freundliche Hilfe der Sekretärinnen Eva Lorenz und Britta Stickel hätte ich den Papierkram sicherlich nicht so gut gemeistert, Danke!

Außerhalb der Arbeit haben mir meine Teamkameraden beim Sport Ablenkung verschafft. Sowohl beim Basketball als auch beim Flag Football konnte ich so ggf. angestauten Stress wieder abbauen. Und alle waren nachsichtig, dass ich es in letzter Zeit nicht häufig zum Training geschafft habe...

Meiner Familie möchte ich für die Unterstützung während des Studiums und der Promotion danken. Am meisten leiden unter meinem Stress in der Endphase musste wohl meine Kerstin, sie hat es aber tapfer durchgestanden und hat mir Halt gegeben. Kurz nach der Disputation haben wir ein noch bedeutenderes Ereignis gefeiert, unsere Hochzeit. Dies lässt diese Arbeit nun ganz klein erscheinen.

